UNIVERSITÀ DEGLI STUDI DI PARMA

Dottorato di ricerca in Fisica

XXIX Ciclo

Protein-based nanostructures as carriers for photo-physically active molecules in biosystems

Coordinatore:
Chiar.mo Prof. Cristiano Viappiani

Tutor:
Chiar.mo Prof. Cristiano Viappiani

Dottorando: Pietro Delcanale

Se ti è nato il gusto di scoprire, non potrai che sentire il bisogno di andare più in là

(Walter Bonatti)

Contents

1 Introduction

Stable self-assembled nanostructures can often be easily obtained in biologically relevant conditions by taking advantage of spontaneous interactions between their constituent components. The research presented in this work is based on the observation that simple self-assembled nanostructures can be built when a small molecule interacts with a carrier protein. This appears to be particularly interesting when the protein exposes binding sites suitable for accommodating small hydrophobic drugs, since the interaction is likely to occur spontaneously in aqueous environment, driven by simple hydrophobic effect. These protein-based nanostructures have been investigated for the delivery of small photo-physically active molecules, all sharing characteristics of hydrophobicity, but being different for structure, origin and photo-physical properties. Large part of the investigation has been carried out on naturally-occurring photo-active molecules, in particular Hypericin, a drug extracted from the plant *Hypericum perforatum*; but also some synthetic metal-organic compounds have been considered. Some major advantages are achieved from the combination of these photo-physically active drugs with the protein carrier, in particular the possibility to a obtain a bio-compatible nanostructure, relying on the fact that protein-based carriers are spontaneously present in biosystems. Since hydrophobic aggregation is generally a limiting factor for the photo-activity of these drugs, a relevant advantage is that the combination with a protein structure promotes the solubilization of the molecules, thus enhancing their photo-activity and increasing their bio-availability. We were thus able to obtain photo-functional nanostructures, potentially interesting for several applications, see Section 2 for details. The functionality of the system is ultimately related to the type of photo-physical or photo-chemical processes of the photo-active molecule. Many of the investigated drugs are photosensitizing molecules, which are exploited in specific photo-treatments to eliminate tumors or to kill pathogen microbes, by means of a reaction called *photosensitization*, which occurs with the simultaneous presence of a photosensitizer, visible light and molecular oxygen. However, simple emission of photo-luminescence can be considered an interesting photo-activity since it potentially allows to localize the distribution of the molecule in a biosystem by imaging techniques. This has been one of the main objects of investigation for our protein-based systems. The type of protein structure that constitutes the scaffold of the photo-functional nanostructure, will mainly dictate the biosystem where the nanostructure has the best perspectives of application. Indeed, the spontaneous presence of the protein within a system guarantees a high level of bio-compatibility for the photo-functional nanostructure based on that protein. We focused on wide-spread proteins belonging to different families, having different origin and folding, only sharing a generic carrier functionality and the possibility to interact with the photo-active molecules.

Following this approach, the results are presented according to the type of protein which constitutes the scaffold of the photo-functional nanostructure. Sections 4.1 and 4.2 collect the results obtained for the nanostructures based on globins, particularly apo-myoglobin, which has been the main object of investigation. We interestingly demonstrated a double functionality, both therapeutic (based on photosensitization) and diagnostic (based on imaging) for these structures, which can be actually considered *theranostic* formulations (see 1.5). In Section 4.3, the results obtained for the nanostructures exploiting the lipocalin β-lactoglobulin are collected. Finally, Section 4.4 presents a first set of results where the model protein Bovine Serum Albumin is successfully used to stabilize an extremely hydrophobic metal-organic compound in biologically relevant conditions. Before entering the main subject of the project, the first chapter of this thesis offers a brief description of the photo-physics of organic molecules in solution.

1.1 Photo-physics of organic molecules in solution

1.1.1 Quantum mechanical description of a molecule

The quantum mechanical wavefunction describing a molecule is generally expresses as:

$$\Psi = \psi e^{-\frac{iEt}{\hbar}}$$

where ψ is the spatial component; E is the energy and t the time variable.

The spatial wavefunction must fulfill the time-independent Schrödinger equation where $\hat{H}$ is the Hamiltonian operator for *non-relativistic* molecular potential energy:

$$\hat{H}\psi = E\psi$$

where $\psi(\vec{r},\vec{R})$ is a function of electronic $\vec{r}$ and nuclear $\vec{R}$ spatial coordinates.

For many-atoms molecules some main approximations have to be considered:

- *Born-Oppenheimer* approximation is based on the observation that the electron mass is considerably smaller than the nuclear mass, so that the motion of electrons do not appreciably perturb the nuclear motion, while electrons rearrange almost instantaneously when nuclear configuration changes. Thus electrons and nuclei can be treated independently and the electronic and nuclear contributions can be separated:

  $$\hat{H} = \hat{H}_{el} + \hat{H}_{nucl}$$

  $$\psi = \varphi_{el}(\vec{r},\vec{R})\, N(\vec{R})$$

  where φ_{el} and N are the electronic and nuclear wavefunctions respectively. φ_{el} depends parametrically on nuclear $\vec{R}$ coordinates, so that the Schrödinger equation can be solved for the electronic component in a given static nuclear arrangement (fixed $\vec{R}$ values).

- If explicit magnetic interactions are neglected, the spin component can be factorized from the electronic wavefunction:

  $$\psi = \varphi \, N \, \sigma$$

  where φ is the spatial electronic wavefunction, N is the nuclear wavefunction and σ is the wavefunction accounting for the spin of electrons [1 2].
- A common approach to obtain the electronic wavefunction of a molecule is the *Hartree-Fock* (or *self-consistent field*) method. This is based on a mean field approximation, where the effects of the other electrons on a given individual electron are approximated by a single averaged effect (mean field). The electrons are considered independent since their mutual interactions are approximated by the mean field, and thus the electronic part of the molecular Hamiltonian is a sum of single electron contributions:

  $$\hat{H}_{el} = \sum_i \hat{h}_i \, \hat{S}_i$$

  where $\hat{h}_i$ and $\hat{S}_i$ are respectively the electronic and spin operators for a single i-th electron. The solutions for φ_{el} are expressed as an anti-symmetrized product of single electron spatial and spin wavefunction:

  $$\varphi_{el} \approx \hat{A} \prod_i \varphi_i \sigma_i$$

  where $\hat{A}$ is the anti-symmetric operator, that is necessary in order to fulfill the *Pauli Principle*, while φ_i and σ_i are the spatial and spin wavefunction for the single i-th electron. The anti-symmetric operator corresponds to a *Slater determinant* accommodating all the one-electron wavefunctions [2 3].
- The nuclear Hamiltonian of the molecules takes into account for translations, vibrations and rotations of the molecule. Neglecting roto-vibrational coupling in the molecular motion, the nuclear Hamiltonian can be factorized:

  $$\hat{H}_{nucl} = \hat{h}_{trasl} + \hat{h}_{vibr} + \hat{h}_{rot}$$

  where the three terms correspond to translational, vibrational and rotational operators. Translational component is not considered since it corresponds to a continuum of energy, the vibrational component is usually approximated by harmonic potential or Morse potential, while rotational contributions are negligible for the purposes of this work.

The time-independent Schrödinger equation for the electronic component of the molecule can be solved under these approximations: electronic eigenstates, or molecular orbitals, and the correspondent eigenvalues, referred to as energy levels, are obtained. In usual conditions, the molecular orbitals corresponding to lower energy levels are occupied according to the Pauli principle. Optical transitions involve the occupied molecular orbitals with higher energy and the energetically closer unoccupied orbitals, particularly the higher occupied molecular orbital (HOMO) and the lower unoccupied molecular orbital (LUMO). Each molecular orbital has vibrational sub-states with corresponding vibrational energy levels, arising from the solution of the Schrödinger equation for the nuclear component at a given electronic configuration. Vibrational states are closer in energy than electronic states. In usual conditions only the lower vibrational sub-level of HOMO is significantly occupied. An optical transition can promote the electron to a higher vibrational state of the LUMO. Rotational sub-states are negligible for the description of photo-physical processes [3].

1.1.2 Singlet and Triplet

The spin state σ_i of an individual electron can be either α or β, schematically corresponding to spin-up and spin-down with respect to the quantization axis. Neglecting explicit magnetic interactions between electrons and in absence of external magnetic field, the spin do not introduce significant changes in the energy configuration of the molecule. However, the spin state of a molecule is crucial for the description of its photo-physics. According to the Pauli principle a single molecular orbital can accommodate at the most two electrons having opposite spin (doubly occupied orbital). Since photo-physical processes involve few orbitals, e.g. HOMO and LUMO, in most cases the spin-orbit state of organic molecules can be simplified as a system of two electrons distributed in two possible orbitals defined a and b, e.g. corresponding to HOMO and LUMO. The doubly occupied orbitals lower in energy that are not involved in optical transitions can be neglected. This system of two electron (labelled 1 and 2) can either assume a spin *singlet* (Σ) or a spin *triplet* state (Θ). Also the spatial electronic state of the system φ needs to be considered in order to fulfill the requirements of the Pauli principle.

- *singlet*:

$$\varphi_S \Sigma$$

where

$$\Sigma = \frac{1}{\sqrt{2}}\big(\alpha(1)\beta(2) - \alpha(2)\beta(1)\big)$$

Σ is anti-symmetric, so the spatial component φ_S must be symmetric in order to fulfill the Pauli principle. Typically, two configurations are possible, as depicted in Fig.1-1:

$$\text{closed shell: } \varphi_S = a(1)a(2)$$

$$\text{open shell } \varphi_S = \tfrac{1}{\sqrt{2}}[a(1)b(2) + a(2)b(1)]$$

The ground state of the majority of organic molecules correspond to a singlet close shell configuration, while the excited state is often a singlet open shell. Singlet spin function Σ correspond to zero spin angular momentum with zero projection on the quantization axis (Fig. 1-2).

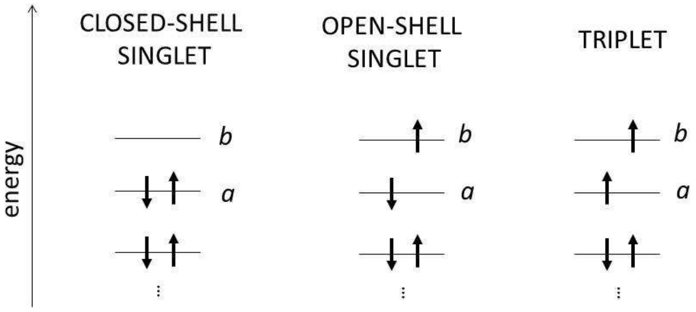

Fig. 1-1 *Schematic representation of electronic configuration for singlet and triplet state of a typical organic molecule. Orbitals labelled a and b are those involved in optical transitions and often correspond to HOMO and LUMO respectively. Orbitals of lower energy are doubly occupied and not involved in optical transitions.*

- *triplet*:

$$\varphi_T\Theta$$

where Θ is symmetric and corresponds to a triplet of states:

$$\Theta[+1] = \alpha(1)\alpha(2)$$

$$\Theta[0] = \frac{1}{\sqrt{2}}[\alpha(1)\beta(2) + \alpha(2)\beta(1)]$$

$$\Theta[-1] = \beta(1)\beta(2)$$

The spatial component φ_T must be anti-symmetric in order to fulfill the Pauli principle and corresponds to:

$$\varphi_S = \frac{1}{\sqrt{2}}[a(1)b(2) - a(2)b(1)]$$

The magnitude of the spin angular momentum vector is $\sqrt{2}\hbar$ and the projection on quantization axis are $\hbar$, 0 and $-\hbar$ corresponding to the three functions of quantum number $+1$, 0 and -1 respectively (Fig. 1-2) [3] [2].

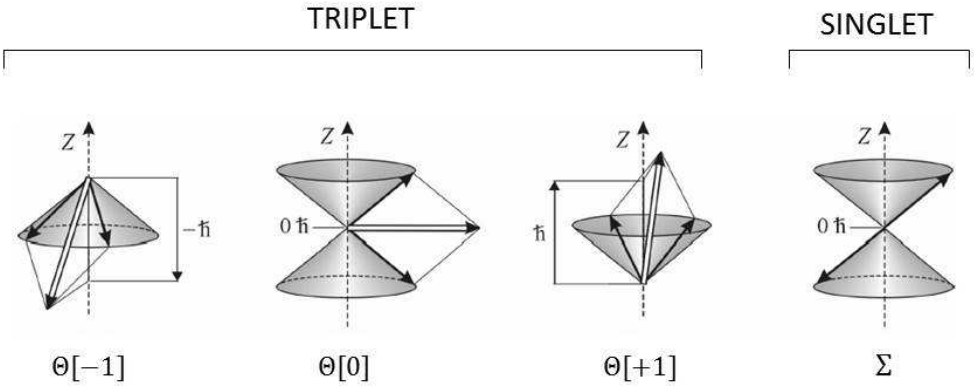

Fig. 1-2 *Symbolic representation of spin angular momenta associated with triplet and singlet states. Contribution of single electron is given with thin arrows and their vector sum with thicker arrow. Z is quantization axis. Adapted from* [3].

The excited triplet state of an organic molecule is always lower in energy than the corresponding excited (open shell) singlet. This is a consequence of exchange interaction: since there is higher probability for the two electron with opposite spin in the singlet state to be nearer, their Columbian repulsion will be more intense [4].

1.1.3 Interaction of molecules with electro-magnetic radiation: transitions and selection rules

The electric field of electro-magnetic radiation interacts with the electric dipole of the molecule and can be treated as a time-dependent perturbation $\hat{H}'$ of the molecular Hamiltonian $\hat{H}$, so that:

$$\hat{H}_{tot} = \hat{H} + \hat{H}' = \hat{H} - \vec{\mu} \cdot \vec{E}$$

where $\vec{\mu}$ is the electric dipole of the molecule and $\vec{E}$ is the electric field of the radiation [1].

Assuming that the electro-magnetic radiation promotes the transition from an initial state Ψ_m to a final state Ψ_n, during the transition the state of the molecule is conveniently described by a superposition of initial and final states:

$$\Psi = a_m \Psi_m + a_n \Psi_n$$

where a_m and a_n are the weight coefficients for the states Ψ_m and Ψ_n respectively. The probability P_n for the molecule to be in the final state Ψ_n in time is a good parameter to monitor the transition in time:

$$P_n = a_n^* a_n \approx \frac{4E_0^2 |\mu_{nm}|^2}{\hbar^2} \frac{sin^2\left(\frac{1}{2}\Delta\omega\, t\right)}{\Delta\omega^2}$$

where

E_0 is the amplitude of the electric field;

$\Delta\omega = \omega - \omega_{nm}$;

ω is the frequency of the electric field;

$\omega_{nm} = \Delta E_{nm}/\hbar = (E_n - E_m)/\hbar;$

$\mu_{nm} = \langle \psi_n | \vec{\mu} | \psi_m \rangle;$

Some important considerations are sketched:

- The probability of transition has a maximum for $\omega = \omega_{nm}$, corresponding to a resonant condition where the energy of the photon absorbed/emitted by the molecule must coincide with the energy gap between initial and final state of the molecule: $\hbar\omega = \Delta E_{nm}$;
- The probability of transition gets higher increasing the intensity of the electromagnetic field;
- The transition electric dipole moment of the molecule, represented by the matrix element $\langle \psi_n | \vec{\mu} | \psi_m \rangle$ is a crucial factor;

Since $\vec{\mu}$ interacts with the molecule's electronic component, the spin and nuclear terms can be factorized and the matrix element can be rewritten:

$$\langle \psi_n | \vec{\mu} | \psi_m \rangle = \langle \varphi_n | \vec{\mu} | \varphi_m \rangle \langle S_n | S_m \rangle \langle N_n | N_m \rangle$$

This gives rise to three main *selection rules* for optical transitions:

- *Symmetry rule*: the term $\langle \varphi_n | \vec{\mu} | \varphi_m \rangle$ and consequently the probability of transition goes to zero if the symmetry between initial and final state is not preserved.
- *Nuclear geometry is preferentially preserved during transitions*: electronic transitions between states with same nuclear configuration are favored. This arises from the term $\langle N_n | N_m \rangle$, called *Franck-Condon factor.*
- *Spin state must be conserved in the transition*: the spin term $\langle S_n | S_m \rangle$ indeed is zero if the initial and final spin states are different. In usual organic molecules transitions between states with same spin multiplicity, e.g. S↔S or T↔T, are allowed, while transitions between states with different spin multiplicity, e.g. S↔T, are forbidden. [a]

Allowed transitions are generally much more probable than forbidden ones, but in real systems selection rules may be not strictly respected.

1.1.4 Photo-physics of organic molecules: Jablonski diagram

Jablonski diagram (Fig.1-3) is a state diagram where molecular electronic states and their relative vibrational sub-states are represented by horizontal lines indicating the relative energies. States are

---

[a] In this work the states of a molecule will be often labelled by S_n and T_n, where S and T refer to the singlet and triplet spin multiplicity respectively while n is a number relative to the energy level of the electronic state in order of increasing energy: n=0 ground state, n=1 first excited state,…

Occasionally a notation will be used referring to the theory of molecular orbitals. The molecular orbitals involved in usual photo-physical processes are π bonding molecular orbital, π* anti-bonding molecular orbital and n that represents a lone pair of electrons. This notation was originally developed for linear molecules but it is often extended to other molecules. d orbitals will be considered for metal-organic compounds (see 1.4) [3 7].

grouped according to spin-multiplicity (S or T) and transitions between states are indicated by arrows [5].

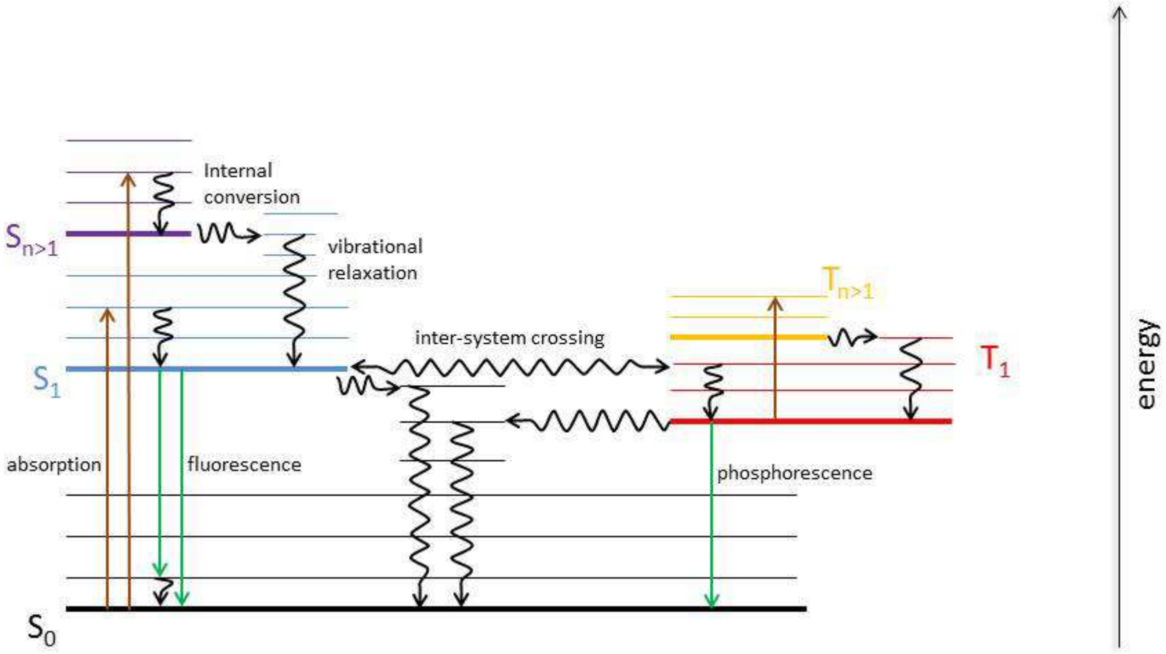

Fig. 1-3 *Jablonski diagram for usual cromophores. Transitions between states are represented by brown (photon absorption), wavy black (non-radiative transitions) and green (radiative transitions) arrows respectively. Energy levels of electronic states are represented by thick lines and different colors, the vibrational sub-levels are represented by thinner lines. Singlet (S) or triplet (T) spin multiplicity is specified.*

Main processes for molecules in solution are described in detail:

- *Absorption*: consists in the absorption of a photon by the molecule. It generally brings a molecule from its singlet ground state S_0 to an excited singlet state S_n of higher energy. It is an extremely fast process occurring with kinetic rate $k \approx 10^{15}$ s^{-1}, and can be considered instantaneous. Absorption may also occur from an excited state to another excited state of higher energy and same spin multiplicity, as in the case of *T-T absorption.*
- *Internal conversion (IC) and vibrational relaxation (VR)*: are the most important non-radiative transitions, i.e. transitions that are not associated with the emission of a photon. IC ($k > 10^{12}$ s^{-1}) is an iso-energetic process between state of the same spin multiplicity where the loss of energy for electronic motion is compensated by nuclear vibrational motion. It implies a coupling between electronic and nuclear motion that would be forbidden by a rigorous application of the Born-Oppenheimer approximation. VR is a transition leading to the lowest vibrational sub-level within the same electronic configuration. It is fast ($k > 10^{11}$ s^{-1}) and associated with heat dissipation. In solution, non-radiative relaxations are often favored because of solvent-induced perturbations: a molecule in its S_n state rapidly (~10^{-12} s) relaxes

to the lower vibrational level of S_1 by IC and/or VR (*Kasha rule*). Because of the *energy-gap law* stating that radiationless transitions generally become exponentially slower as the energy difference between states increases, the non-radiative relaxation $S_1 \rightarrow S_0$ is much slower than $S_n \rightarrow S_1$ and become comparable with radiative processes.

- *Inter-system crossing (ISC)*: is an iso-energetic transition between two states having different spin multiplicity, typically singlet and triplet. ISC is a process that breaks the spin selection rule, it is indeed slow ($k = 10^6$-10^{11} s^{-1} for $S_1 \rightarrow T_1$, $k = 10^{-2}$-10^4 s^{-1} for $T_1 \rightarrow S_0$) and unlikely compared to spin-allowed processes. The physical origin for ISC is related to spin-orbit coupling (SOC), that usually introduces a perturbative term in the molecular Hamiltonian. The extent of the SOC scales with the fourth power of the atomic number Z (SOC~Z^4) and is therefore more intense in the presence of heavy atoms [2]. For some kind of molecules, like *photosensitizers* (see 1.2), the ISC $S_1 \rightarrow T_1$ occurs with high probability and with kinetic rates comparable with those of competitive processes like IC, VR and fluorescence. This may be due to several factors like: (I) SOC and solvent perturbations; (II) small energy gap between S_1 and T_1; (III) presence of a symmetry forbidden $S_1 \rightarrow S_0$ competitive transition; (IV) the *El-Sayed rule*, stating that a compensation may occur between the change of spin state (break of spin selection rule, e.g. in $S_1 \rightarrow T_1$) and the change of orbital angular momentum related to a change of symmetry (break of the symmetry selection rule, e.g. in $n \rightarrow \pi$) so that the total angular momentum is conserved and the process becomes partially allowed [6]. The back ISC transition $T_1 \rightarrow S_0$ is generally slower and less favored than $S_1 \rightarrow T_1$ so that the T_1 state often behaves like a “trap” with a several order of magnitude longer lifetime compared to other excited states.
- *Fluorescence*: is a radiative process associated to the transition between states of the same spin multiplicity. Because of the *Kasha rule*, invariably the transition is $S_1 \rightarrow S_0$ and results in the emission of a photon having energy corresponding to the energy gap between the two states. Fluorescence is a relatively fast process that in solution occurs with $k \approx 10^9$ s^{-1}. The photon emitted for fluorescence is always less energetic than the photon absorbed (*Stokes shift*).
- *Phosphorescence*: is a radiative transition between states of different spin multiplicity, e.g. $T_1 \rightarrow S_0$. It is very unlikely, characterized by very low quantum yields (10^{-4} – 10^{-5}) and $k \approx 10^{-2}$-10^2 s^{-1}, reflecting the extremely long lifetime of the “trap” T_1 state. In solution, phosphorescence decay is indeed essentially determined by the concentration of quenchers of the T_1 state, i.e. species that interact with the molecule and enhance the non-radiative de-excitation rate thus reducing triplet lifetime and emission intensity. The most common and

ubiquitous quencher is molecular oxygen (see 1.2) that typically sets the phosphorescence lifetime in the order of 10^{-6} s, for air-equilibrated solutions[3].

1.2 Singlet oxygen and photosensitization

1.2.1 Singlet Oxygen

The peculiar electronic configuration of the oxygen molecule O_2 gives rise to several unusual properties particularly regarding its magnetic behavior, spectroscopy, energy transfer processes and chemical reactivity. According to the theory of molecular orbitals, the 16 electrons of the molecule are distributed in a configuration where all molecular orbitals are doubly occupied, except the two anti-bonding orbitals π_x* and π_y* that accommodate two unpaired electrons (Fig. 1-4). Three electronic state of different energy can thus be individuated for O_2. The ground state of O_2 is a spin triplet state indicated as $O_2(^3\Sigma_g^-)$ [b] or simply $^3O_2$. The first excited state is a spin singlet state, doubly degenerate, with an energy of ~95 kJ mol^{-1} higher than the ground state. It is indicated as $O_2(^1\Delta_g)$ or simply $^1O_2$, and it is often referred to as *singlet oxygen*. The second excited state is also a (non-degenerate) spin singlet having an energy of ~158 kJ mol^{-1} higher than the ground state and indicated as $O_2(^1\Sigma_g^+)$ (Fig. 1-4). [7] [8] [9]

---

[b] To indicate the molecular states of O_2, the full notation developed for bi-atomic molecules was used:

$$(^{2S+1}\Lambda_{g/u}^{+/-})$$

Λ : symbol ($\Sigma, \Pi, \Delta, \ldots$) corresponding to the quantum number M_L (0,1,2,…) which indicates the projection of the molecular orbital angular momentum
S : quantum number for total spin angular momentum
u/g : parity (ungerade or gerade)
$+/-$: indicates the symmetry with respect to a C2 axis orthogonal to the internuclear axis in the midpoint

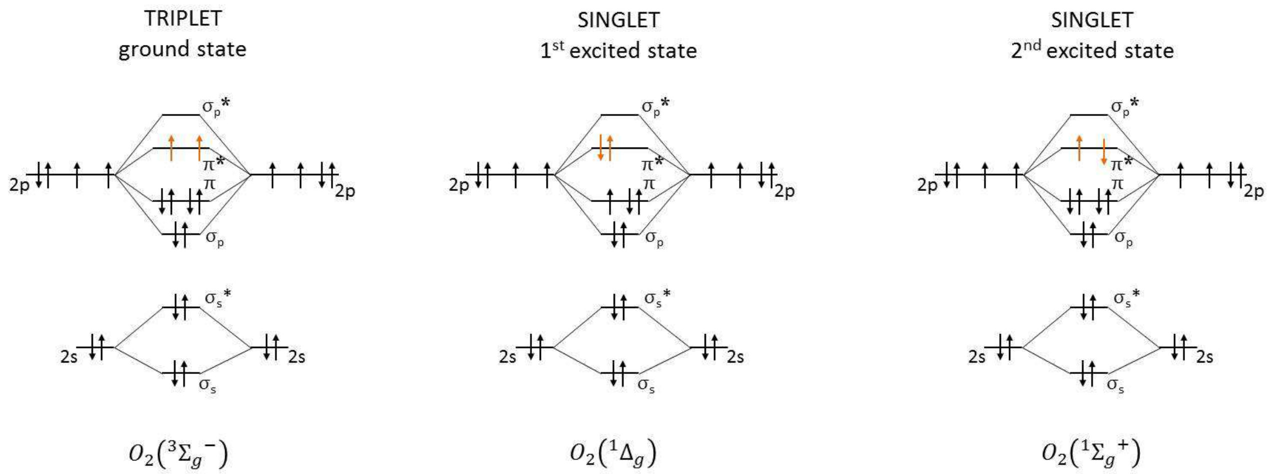

Fig. 1-4 *Electronic configuration of molecular oxygen according to the theory of molecular orbitals. The configurations for the triplet ground state and the excited singlet states are reported.*

In gas phase, i.e. with negligible solvent-induced perturbations, radiative kinetic rates of the transitions between the states $O_2(^3\Sigma_g^-)$, $O_2(^1\Sigma_g^+)$ and $O_2(^1\Delta_g)$ are small (Tab. 1-1), since they are forbidden processes. In solution, the transitions become more probable because of solvent-induced perturbations, and thus faster (Tab. 1-1). However, non-radiative deactivations prevail resulting in low emission quantum yields (10^{-3} – 10^{-7}).[10] The phosphorescence associated to the transition $O_2(^1\Sigma_g^+)$→$O_2(^3\Sigma_g^-)$ is barely detectable in solution, because the non-radiative relaxation $O_2(^1\Sigma_g^+)$→ $O_2(^1\Delta_g)$ prevails. The phosphorescence emission at ~1270 nm associated to the transition $O_2(^1\Delta_g)$→$O_2(^3\Sigma_g^-)$ is weak but detectable with an appropriate detection system. Because of the spin-forbidden character of the transition to the ground state, $O_2(^1\Delta_g)$ is a rather long-living transient state, with a characteristic lifetime of 3-4 μs in aqueous solutions (Tab. 1-1). [11] [8] $O_2(^1\Delta_g)$ thus constitutes the species of interest in biosystems because its relative stability allows the reaction with several substrates.

transition	$\boldsymbol{O_2(^1\Delta_g)\rightarrow O_2(^3\Sigma_g^-)}$	$\boldsymbol{O_2(^1\Sigma_g^+)\rightarrow O_2(^3\Sigma_g^-)}$	$\boldsymbol{O_2(^1\Sigma_g^+)\rightarrow O_2(^1\Delta_g)}$
wavelength (nm) (solution)	1269-1282	765	1914-1936
τ_r (gas)	64.6 min	11.8 s	6.7 min
τ (aqueous solution)	3-4 μs	8.2 ps	-

Tab. 1-1 *Properties associated to the transitions between the energetically lowest electronic states of O_2.*[10] [12]

1.2.2 Photosensitization

Photosensitization is a process where a molecule called *photosensitizer* (PS) is excited to an electronically-excited state by the absorption of a photon and then induces a chemical alteration in a second molecule called *substrate*. The photosensitization proceeds from the excited state of the PS, it is thus subordinate to the absorption of a photon, usually in the UV-visible range, that triggers the reaction. The process requires an interaction between the excited PS (PS*) and the substrate, resulting in an alteration of the latter. Two different typologies of photosensitization can be distinguished: (I) *type I* photosensitization that involves a charge transfer mechanism, e.g. the reduction of photo-excited chlorophylls [13]; (II) *type II* photosensitization that involves an energy transfer mechanism [c], e.g. between excited triplet state of chlorophylls and the carotenoid molecules[14].

Provided that nearly every PS has a singlet ground state, photosensitization may in general proceed from both singlet or triplet excited states. Other de-excitation processes, i.e. fluorescence, IC and VR or phosphorescence, are thus competitive with the photo-reaction. Since photosensitization is a bi-molecular process requiring the interaction of PS* and the substrate, the upper limit for the reaction kinetic will be set by the diffusion kinetic and the concentration of the two species in solution. The lifetime of PS* is therefore crucial since the probability of interaction with the substrate will be higher for longer living excited states. Indeed, in conditions that are significant for applications, photosensitization becomes relevant only when it involves the excited triplet state of the PS (^{3}PS*), whose lifetime is several order of magnitude longer than the one of the excited singlet states.

The substrate in a photosensitized reaction may be a specific target, a solute or a molecule of the solvent, but the most common and wide-spread is $^3O_2$. It efficiently reacts with both singlet and triplet excited state of many PS. However, at usual concentrations or under physiological conditions, only the reaction with ^{3}PS* is significant [8] [15]. The products of the photosensitized reaction involving O_2 fall under the category of so-called *reactive oxygen species* (ROS). If a type I reaction occurs, usually ^{3}PS* is oxidized to $PS^{+\bullet}$ and O_2 is reduced to the radical species *super-oxide anion* ($O_2^{-\bullet}$), that in turn can generate other radicals (Fig. 1-5). In this case the PS needs to be reduced after the photosensitization to recover its initial state.

---

[c] There is no general agreement about the definition of type I and type II reactions. Some authors classify the reactions according to the substrate molecule: if the substrate is O_2 the reaction is type II, otherwise it is type I. Other authors distinguish the reactions according to the primary process: type I involves a charge transfer and type II an energy transfer. Here the second classification is used. [62]

If $^3PS^*$ has a suitable energy (> 95 kJ/mol) a type II reaction may occur where the PS returns to its initial singlet ground state while $^3O_2$ (precisely $O_2(^3\Sigma_g^-)$) is simultaneously excited to an electronically excited singlet state (either $O_2(^1\Sigma_g^+)$ or $O_2(^1\Delta_g)$). Given the fast relaxation $O_2(^1\Sigma_g^+) \rightarrow O_2(^1\Delta_g)$ occurring in solution, $^1O_2$ will be the final product of the reaction (Fig. 1-5). This energy transfer process is called *Dexter* or *exchange* mechanism, and it can be conveniently visualized as the simultaneous transfer of two excited electrons from one species to the other, so that there is no net charge transfer. The process is spin-allowed so it occurs with relatively high probability, but it requires a collision between the two partners since the wavefunctions of the involved electrons must overlap [3].

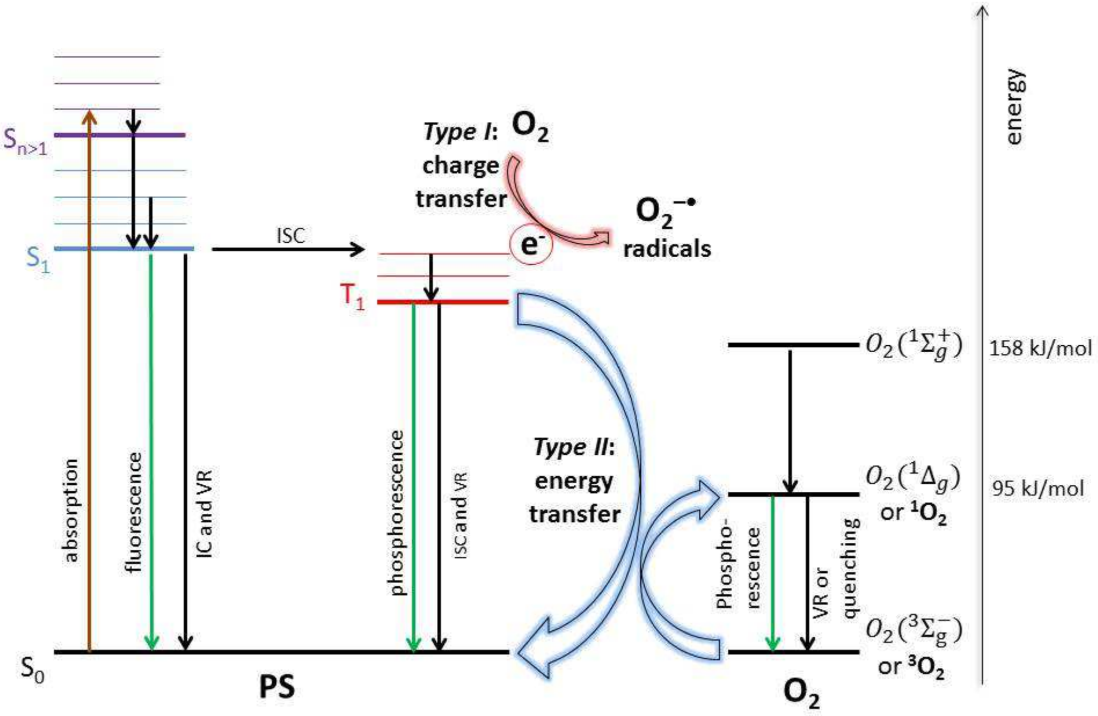

Fig. 1-5 *Simplified Jablonski diagram for the photosensitization of* O_2 *in usual conditions. Non-radiative transitions (IC, VR, ISC or quenching), absorption and radiative transitions (fluorescence and phosphorescence) are indicated with black, brown and green arrows respectively. S and T labels denote respectively singlet and triplet spin multiplicity of the PS. The two types of photosensitization occurring from the excited triplet state (*T_1*) of the PS are sketched.*

The quenching of $^3PS^*$ by O_2-induced photosensitization is so important that in many common air-equilibrated solutions and in absence of other specific quenchers, the experimentally observed lifetime of the triplet state τ_T is essentially determined by the O_2 concentration, according to the equation:

$$\tau_T = \frac{1}{k_T} = \frac{1}{k_{ISC} + k_{phosph} + k_q[O_2]}$$

where τ_T and k_T are the observed triplet state lifetime and decay rate respectively; k_{ISC} and k_{phosph} are the kinetic rates for the mono-molecular processes of triplet state de-excitation, i.e. ISC and phosphorescence respectively; $k_q[O_2]$ is the bi-molecular term accounting for the O_2-induced quenching. It is determined by the O_2 concentration $[O_2]$ and by the quenching rate constant k_q, whose value is diffusion-limited to at most 10^9 M^{-1} s^{-1}. In usual conditions, the mono-molecular processes are really slow and the quenching dominates the kinetic, so that:

$$(k_{ISC} + k_{phosph}) \ll k_q[O_2]$$

An important experimental parameter is the quantum yield of $^1O_2$ photosensitization (Φ_Δ), that reflects how many $^1O_2$ molecules are generated with respect to the photons absorbed by the PS. Since the photosensitization proceeds appreciably only from the $^3PS^*$, in absence of other specific quenchers, it can be written:

$$\Phi_\Delta = \Phi_T S_q S_\Delta$$

where Φ_T is the quantum yield for the triplet state formation;

$S_q = \frac{k_q[O_2]}{k_{ISC}+k_{phosph}+k_q[O_2]}$ is the efficiency of the O_2-induced quenching;

$S_\Delta = \frac{k_{et}}{k_q}$ is the efficiency of the energy transfer process leading to $^1O_2$ generation.

Since $(k_{ISC} + k_{phosph}) \ll k_q[O_2]$, it follows that $S_q \approx 1$ and thus:

$$\Phi_\Delta = \Phi_T S_\Delta$$

Once formed, $^1O_2$ decays in time according to the usual exponential trend of excited states, characterized by an observed lifetime τ_Δ. Because of the high reactivity of $^1O_2$, in biosystems the value of τ_Δ is affected by the presence of quenchers, either physical or chemical. [11] [16]

1.2.3 Reactivity of $^1O_2$ in biosystems

The reactivity of ground state $^3O_2$ is limited by the fact that the outermost electrons have to be spin-paired to react with another molecule. Thus the activation energy for most reactions involving $^3O_2$ is relatively high (at least 95 kJ mol^{-1}) and makes non-catalyzed reaction extremely slow at usual temperatures. $^1O_2$ has all electron spin-paired and is indeed highly reactive with respect to $^3O_2$ without being a free radical. There are two competitive de-activation (quenching) channels for $^1O_2$ and their importance in a biosystem depends on the environment of the molecule:

- *Physical quenching*: $^1O_2$ returns to its ground state without formation of products. The energy is dissipated by interaction with the solvent or by energy transfer to a specific quencher that becomes electronically excited. Relevant examples of physical quenchers, sometimes referred to as *$^1O_2$ scavengers*, are azide (N^{3-}), 1,4-diazabicyclo[2,2,2]octane (DABCO) and carotenoids, whose role is crucial in biology [17].

- *Chemical quenching*: is an actual chemical reaction between $^1O_2$ and a substrate, resulting in the generation of a final and/or intermediate product. $^1O_2$ is electrophilic and readily reacts with electron rich moieties, e.g. the double bonds of lipids, thiols and ascorbate [18]. The chemistry of $^1O_2$ is extremely rich, but in biological systems three main substrates of $^1O_2$ can be individuated: *lipids* (or lipidic moieties), *proteins* and *DNA*.

Membrane lipids are an important target in biological environments. Because of its electrophilic nature, $^1O_2$ preferentially reacts with unsaturated phospholipids or cholesterol generating lipidic hydroperoxide species that in turns may generate free radicals [19] [20]. The nucleobase that is most susceptible to $^1O_2$-mediated oxidation is guanine which constitutes the main target in both isolated and cellular nucleic acids [21]. Proteins are considered the most efficient quenchers of $^1O_2$ in terms of quenching rates, even though the identification of the main target of oxidation in a real bio-sample is affected by different factors like the local concentration, the accessibility of the substrate and the site of $^1O_2$ generation. Tryptophan is the only amino acid inducing a significant physical quenching of $^1O_2$ ($k_q \approx 10^8\ M^{-1}\ s^{-1}$). Other amino acids with high electron density moieties, like double bonds or sulfur groups, are more susceptible to chemical reactions with $^1O_2$. In physiological conditions, important reactivity is observed for Cysteine, Methionine, Tyrosine, Histidine and Tryptophan, which acts as both physical and chemical quencher [22] [23] [24] [25] [26].

The diffusion of $^1O_2$ is an important issue to address for the applications which exploit the high reactivity of this species. In photo-medicine, the extent of $^1O_2$ diffusion within a cell is crucial since it is related to the spatial extent of the oxidative damage/stress caused by the reactions with lipids, proteins or DNA. The radial diffusion distance (d) over time (t) is related to the diffusion coefficient (D) by the equation:

$$d = \sqrt{6Dt}$$

Considering that $^1O_2$ decays in time with a characteristic lifetime τ_Δ, its diffusion will be limited to values of d corresponding at most to $t = 5\tau_\Delta$. Several parameters like temperature, viscosity, solvent, local concentration of O_2 and presence of $^1O_2$ quenchers around the site of photosensitization heavily affect the value of d. In a highly inhomogeneous medium like the cell environment, it is difficult to obtain quantitative results. The most recent studies report an apparent value for $^1O_2$ intra-cellular d in eukaryotic cells corresponding to ~100 nm [27]. Considering the typical size of mammalian cells (tens of μm), the oxidative effect of $^1O_2$ appears to remain confined in the surroundings of the photosensitization site, even thou d is large enough to allow $^1O_2$ to diffuse trough different cellular environments and crossing membranes [28]. A considerably lower amount of literature is available about the diffusion of $^1O_2$ in prokaryotic cells, where $^1O_2$ decays appears to be highly dependent upon the localization of the PS [29] [30] [31].

1.2.4 Production and detection of $^1O_2$

The most wide-spread and efficient method to obtain $^1O_2$ is photosensitization. A considerably large number of efficient PS or photosensitization systems has been individuated and developed. As previously described, photosensitization requires the simultaneous presence of $^3O_2$, light and the PS and may lead to the production of radicals (type I photosensitization) even if the generation of $^1O_2$ is usually favored. An interesting alternative method is the direct photo-activation of $^3O_2$ to $^1O_2$ by mean of the absorption of an IR photon. Although it is somehow more direct, this methods is experimentally demanding since it requires a powerful laser excitation at ~1270 nm, and results 10^4-10^5 times less efficient than photosensitization [32] [33]. Interestingly, the direct excitation of $^3O_2$ to the second excited singlet state $O_2(^1\Sigma_g^+)$ using a 765 nm laser beam was recently reported on a mammalian cell [34].

The election method for detecting the presence of $^1O_2$ is the direct monitoring of its NIR phosphorescence at 1270 nm, that have been used also in the context of this work. This method allows a direct assessment of the presence of $^1O_2$ in a system and also the measurement of its decay kinetics. The efficiency of the photosensitization can be estimated by comparison with a reference PS of known Φ_Δ [35] [36]. Several alternative indirect methods for $^1O_2$ detection exist like the use of chemical traps or luminescent reporters activated by $^1O_2$ [37], detection of delayed fluorescence from the PS [38] or electron paramagnetic resonance. Also photothermal methods like laser induced opto-acoustic spectroscopy or thermal lensing may give useful information, even thou they are not specifically sensitive to $^1O_2$ [39]. Additional information for confirming the presence of $^1O_2$ can be obtained by the introduction of solvent isotopes like D_2O instead of H_2O or specific physical $^1O_2$ quenchers, that induce respectively a stretching and a shortening of τ_Δ [40].

1.3 Photosensitization-based applications

The majority of photosensitization-based applications exploits the photo-inactivation of unwanted cells induced by the generation of ROS. $^1O_2$ is generally recognized as the species that is mainly responsible for the photo-toxicity, even if radicals may play a significant role in some systems. Photosensitization-based medical therapies are the most wide-spread and are generally referred to as *photodynamic therapy* (PDT). The modern PDT developed from the '70s for the treatment of cancer, that has been the main object of research for long, leading to several clinically approved therapies. Photosensitization-based treatments of infections, sometimes referred to as *antimicrobial PDT* (APDT), developed from the '90s and are now gaining growing interest [41].

The main advantage of PDT is probably the selectivity for the target cells/tissue. This is provided by a combination of factors like: the photo-activation of the cytotoxic effect; the selective irradiation of the region to be treated; the preferential localization of the PS on the target cells, that may occur spontaneously or by mean of a delivery system. Additionally, the use of non-ionizing non-mutagenic visible or NIR light is relatively safe and minimally invasive. An important advantage is the possibility of directly visualize the distribution of the drug in a tissue/cell also during the treatment, exploiting the fluorescence emission of several PSs. On the other hand, the main drawback of PDT is probably constituted by the penetration of light in tissues, that is limited to few mm, and heavily restricts the applicability [42] [43] [44] [45] [46].

The interest concerning antimicrobial photosensitization-based methods recently extended beyond the clinical applications. Some interesting example are the development of photo-pesticides for insects or parasites eradication, methods for water disinfection and blood sterilization, the development of self-cleaning tissues and applications for the hygiene of products or packaging materials [47] [16]. One of the most promising non-clinical application concerns the decontamination of food and food-processing environment from common pathogen microorganisms (fungi, yeasts, molds and bacteria, often grown in bio-film). This is particularly important for not-cooked food like fruits, vegetables, sprouts, cheese and cold cuts. In these cases, an important issue is the bio-compatibility of the photosensitizing agent, that must have low impact on the quality of the product [48] [49] [47].

1.3.1 Cytotoxicity: Tumor cells and bacteria

The photosensitized production of ROS inside or in the close vicinity of a cell may result in cell damage and death. As previously discussed, this is mainly a consequence of the high reactivity of $^1O_2$ towards multiple targets, i.e. lipids, proteins and DNA. Both eukaryotic and prokaryotic cells can be inactivated by photosensitization. Tumor cells, fungi, viruses, parasites or pathogen bacteria are the main targets. The efficacy of the photo-induced cytotoxicity in a real biosystem is affected by a large number of factors. However, given the limited diffusion of $^1O_2$ (see 1.2.3), the localization of the PS at the cellular level appears to be a crucial parameter. The results reported in this work only involved in vitro studies of photosensitization on tumor cells (cell lines HeLa and PC3) and on bacterial cells in suspension (*Staphylococcus aureus*, *Escherichia coli* and *Bacillus subtilis*). A quick overview of few concepts is reported below:

- *Tumor cells:* three mechanisms of death are typically reported for tumor eukaryotic cells, whose contribution is variable according to the conditions and the system under study: (I) *necrosis* is a traumatic cell death that follows a drastic perturbation, e.g. consequence of a fast localized production of $^1O_2$ in relatively large amount. It typically occurs for ROS initially produced on the plasma membrane. In a tissue, necrosis is usually followed by other responses like inflammation, that may reinforce the tumor eradication; (II) *apoptosis* is a programmed cell death that may be induced by $^1O_2$ produced at specific locations (e.g. mitochodria or lysosomes), that triggers a cascade of controlled events resulting in cell death; (III) *autophagy-associated* cell death, occurring in a tissue, can be stimulated by various stress signals including oxidative stress, particularly when ROS are generated on endoplasmic reticulum. For tumor eradication it must be considered that, beside the damage at the cellular level, photosensitization often induce effects at the tissue level, e.g. vascular damaging, or important system responses like inflammation and immune-responses [42] [50] [44] [51].
- *Bacterial cells:* infectious diseases constitute a challenging health problem since the rapid evolutionary change, the large number of pathogens bacteria and the development of multi-resistant strains are impairing the efficacy of traditional treatments based on antibiotics. The growing interest concerning antimicrobial photosensitization-based applications is indeed due to the observation that no development of resistant species was observed after several photo-treatments [52] [53]. From the point of view of applications, bacteria can be conveniently divided into two categories according to their anatomy. *Gram-positive* bacteria have one cell membrane surrounded by periplasmic space and an external 20-80 nm thick protective wall, mainly constituted by peptidoglycan layers. This structure is a rather porous barrier and allows several photosensitizing agents to diffuse to the plasma membrane and possibly inside the cell. In *Gram-negative* bacteria there are two lipid bilayers sandwiching a peptidoglycan layer, and an additional 10-15 nm thick outer element is present, mainly constituted by lipopolysaccharide, lipoproteins and teichoic or lipoteichoic acid. This gives rise to a highly packed and negatively charged external surface that inhibits the penetration

of compounds with molecular weight larger than 600-700 Da or with lipophilic character. It is generally recognized that small cationic PSs efficiently diffuse through the external membrane to the sensitive inner membrane and are thus more efficient for the photo-inactivation of these bacteria [52 54 55].

1.3.2 Photosensitizers

Since PDT of cancer have been the main object of research for long, photosensitizing agents were conveniently classified into three generations that reflect the development of research in this field. *First generation PSs* usually refer to Photofrin® and Haematoporphyrin derivatives, that were the first approved for clinical treatment of cancer. They are constituted by a complex mixture of different porphyrin compounds, based on a tetrapyrrole structure, found as monomers, dimers and oligomers [44]. *Second generation PSs* are generally intended to be pure single compounds, often synthetic, developed for meeting the specific requirements of the therapy. More recently, the research is focusing on the development of systems where a PS is combined to a specific delivery system [56]. The aim is mainly to enhance the selectivity for target cells and allow for a more reliable diagnosis, e.g. through direct imaging of the photosensitizing agent in tissues. These are sometimes referred to as *third generation PSs* and their use can be included in the so-called *theranostic* applications (see 1.5) [16 43].

An overview of important types of PSs is proposed, where the compounds are classified in broad categories according to their origin [43 11 50]:

(I) *Structures based on tetrapyrrole* are wide-spread and extremely diversified, but they all share a structural core constituted by the tetrapyrrole ring. They include *porphyrins*, *chlorins*, *bacteriochlorins* and *phtalocyanines*. The majority of clinically approved PSs for PDT of cancer falls under this category;

(II) *Synthetic dyes* cover a broad range of PSs including *phenothiazinium salts* like Methylene Blue or Toluidine Blue, *xanthene dyes* like Rose Bengal, *squaraines*, *boron-dipyrromethene (BODIPY)* dyes, *phenalenones* and *transition metal compounds*. Several compounds of this category have been successfully exploited for antimicrobial purposes;

(III) *Natural PSs* are usually easy to obtain and likely bio-compatible. Relevant examples are *chlorophylls*, *flavins*, *coumarins*, *curcuminoids* and *polihydroxi-quinones* like hypericin or hypocrellin;

(IV) *Artificial nanostructures* like fullerenes and semiconductor materials e.g. TiO_2 nano-particles, are recently developing.

The properties of a good PS are ultimately established by its specific perspective of application, but some general features can be individuated: (I) high molar extinction coefficient in the visible range of the spectrum; (II) high values of Φ_T and Φ_Δ; (III) purity of the compound, with suitable chemical and photo-stability; (IV) low dark toxicity and bio-compatibility; (V) preferential interaction with the target cells and possibility of easy clearance after treatment; (VI) water-solubility; (VII) fluorescence emission; (VIII) maximum absorption between 600-800 nm, where excitation light more efficiently penetrate tissues. The size, together with the electrostatic charge of the photosensitizing agent, are particularly important parameters for antimicrobial applications, since they may affect the ability of the drug to penetrate the cell wall [50 54 11].

1.4 Triplet emitters

Few basic concepts are reported concerning the peculiar photo-physical properties of the metal-organic compounds called *triplet emitters*. The photo-physics of usual organic dyes involve frontier molecular orbitals, generally n, π and π*. For organo-transition metal complexes, also the d (or f) orbitals of the metal must be considered since they are involved in optical transitions. Two components are usually distinguished in these complexes: the metal atom and the ligand, i.e. the organic portion. The d orbital is spatially centered on the metal, while π and π* orbitals are mainly localized on the ligand portion. The spatial localization of the orbitals involved in the transition is extremely important for this class of compounds, so that the transitions are classified as:

- *Metal-centered* (MC): involving orbitals mainly located on the metal, usually these are relevant only for f-f transitions in lanthanides;
- *Ligand-centered* (LC): involving orbitals mainly located on the ligand portion, typically π→π*;
- *Charge transfer transitions* (CT): where orbitals centered on the metal and on the ligand are involved. For the complexes studied, only *metal-to-ligand charge transfer* (MLCT) transitions are significant, where the an electron is excited from an orbital mainly centered on metal to one mainly localized on the ligand, e.g. d→ π*;

For describing the photo-physical properties of triplet emitters, both LC and MLCT transitions must be considered. In many triplet emitter molecules, two photo-excitations are possible from the ground state: MLCT (d→ π*), leading to a dπ* excited state; and LC (π→π*), leading to an ππ* excited state (see Fig. 1-6 A).

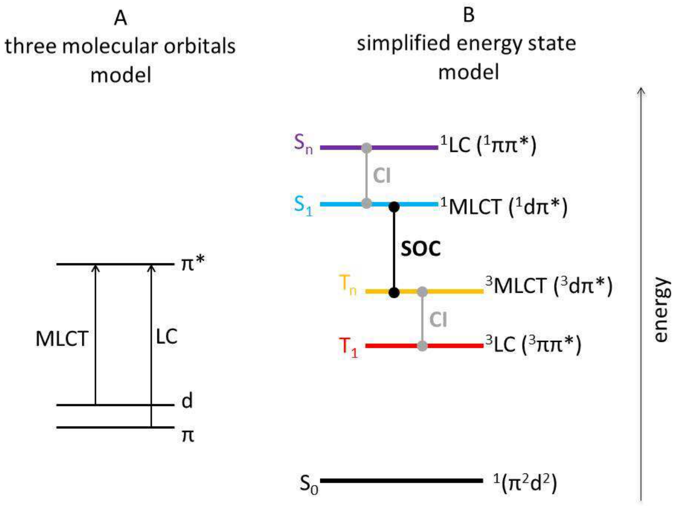

Fig. 1-6 *A: simplified introductory three molecular orbitals model for a compound with single d, π and π* orbitals. d and π are the HOMO and the HOMO-1 respectively, while π* is the LUMO of the transitions. B: simplified energy state model where spin states are considered, different labels are reported for electronic states. The coupling of LC and MLCT states due to CI and singlet and triplet states due to SOC are represented with grey and black vertical lines respectively.*

As represented in Fig. 1-6 B, if the spin of the electrons is considered, eight excited states exist:

- two singlet states: ^{1}dπ* (or ^{1}MLCT) and ^{1}ππ* (or ^{1}LC);
- six triplet states: ^{3}dπ*(or ^{3}MLCT) and ^{3}ππ* (or ^{3}LC);

Energetically, excited triplet states are always lower in energy that the corresponding singlet states, but the splitting between singlet and triplet is higher for LC states (ππ*) than for MLCT (dπ*). This is a consequence of the lower repulsion between electrons on spatially separated orbitals.

With respect to the usual quantum mechanical description of organic molecules, two additional contributions must be taken into account for an adequate description of triplet emitters: SOC and configuration interaction (CI). As previously discussed, SOC is at the basis of the coupling between singlet and triplet states. Since SOC is more relevant in the presence of heavy atoms, it will be rather strong for molecules containing metal atoms. As explained in Section 1.1, the electronic wavefunction of a molecule is conveniently retrieved using a mean field approximation (Hartree – Fock method), where the electrons are considered independent and the electron-electron interactions are treated as an averaged effect. However electrons do interact, and in metal-organic complexes their relative interactions can be substantially different according to their spatial localization, e.g. for LC or MLCT states. A more refined description of molecular states that introduces additional terms to the mean field approximation is constituted by the CI. This enables a coupling between LC and MLCT excited states, so that the state of electrons cannot be identified as purely LC or purely

MLCT, when CI is considered. The overall effect of SOC and CI is that singlet and triplet, or LC and MLCT cannot be regarded as "pure" classifications: the excited states are actually mixed (Fig. 1-6 B). This gives rise to the peculiar photo-physical properties of triplet emitters [3] [4].

SOC heavily affects the photo-physical behavior since it confers a "singlet" character to an excited triplet state and thus promotes the transition to the singlet ground state, that results partially allowed. In turn, the mixing of states due to CI also affects the photo-physical properties since it introduces indirect SOC routes. A simplified model for a generic quasi-square planar triplet emitter, which is the type of compounds used in this work, is presented in Fig. 1-7.

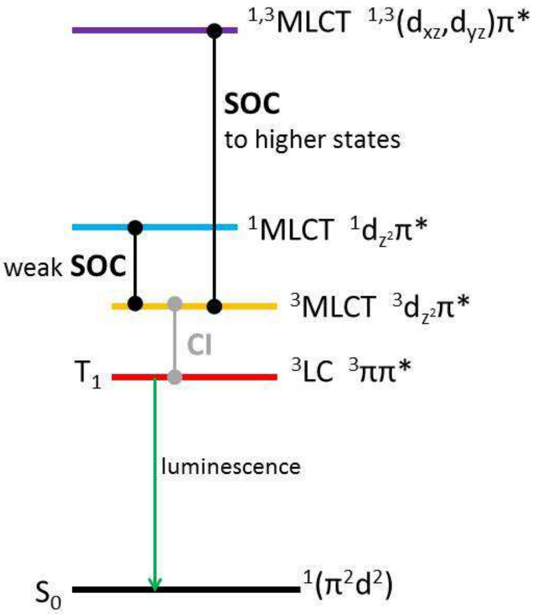

Fig. 1-7 *Schematic simplified diagram for quasi-square planar triplet emitters.*

In these compounds, the SOC between ^{3}LC and ^{1}MLCT, namely $^3\pi\pi^*$ and $^1d\pi^*$, is negligibly weak. The SOC between ^{1}MLCT and ^{3}MLCT, namely $^1d\pi^*$ and $^3d\pi^*$, is considerable only when different d-orbitals are involved (i.e. d_{z^2} and d_{xz} or d_{xz}). For quasi-square planar configuration the energy difference between these states is rather high (~0.5eV) and thus the strength of SOC is weaker when compared to quasi-octaedral complexes. The CI is indeed crucial since it mixes the lowest ^{3}LC state ($^3\pi\pi^*$) with ^{3}MLCT ($^3d_{z^2}\pi^*$) introducing an indirect coupling between the low laying ^{3}LC and the ^{1}MLCT states of higher energy. This indirect SOC route is the dominant process responsible for photo-luminescence in many complexes.

When compared to common organic dyes, these compounds show unusual photo-physical behavior. The emission of fluorescence associated to the transition $S_1 \rightarrow S_0$, which is the most probable radiative process in common dyes, is not observable for triplet emitters. Actually the definition of a “pure” S_1 excited singlet state loose its meaning because of the mixing of excited states. In usual organic compounds $T_1 \rightarrow S_0$ transitions are strongly unlikely, and consequently the emission of phosphorescence is almost totally quenched ($\Phi \approx 10^{-4}$ - 10^{-5}) and extremely slow (up to minutes in absence of O_2, see 1.1). In triplet emitters, the admixture of a singlet character to the ^{3}LC state (T_1), drastically increases the probability of a radiative transition to the ground state, that occurs with a decay time several order of magnitude faster than a typical phosphorescence and with a high quantum yield. The emission of triplet emitters, properly indicated as *luminescence*, is additionally widely tunable, according to the features of the molecule. Because of the triplet state character of the excited state, the luminescence is often affected by the presence O_2 and the molecules may act as PS. A large number of triplet emitters have been synthesized in order to meet the requirements of specific applications. They are usually developed for organic light emitting diode (OLED) devices, but recently their peculiar properties of photo-luminescence make them attractive as sensors for bio-imaging [4] [57] [58].

1.5 Theranostics

Nanomedicines are carrier systems with sub-µm size developed to improve the delivery of a therapeutic agent in a biosystem. Relevant examples of nanomedicines are liposomes, polymers, micelles, nanoparticles and antibodies. Beside the drug delivery to a target site and the therapeutic action, these formulations have been widely exploited for imaging applications as well, e.g. for the delivery of a contrast agent. In the last decade, the research about nanomedicines focused on the development of minimally invasive systems where a therapeutic agent and a diagnostic agent for imaging are combined within the same nano-sized formulation. Since these systems provide both therapeutic and diagnostic functionality, allowing the detection and the treatment of diseases in a single procedure, they are referred to as *theranostic* agents [59] [60] [61].

Theranostic formulations greatly differ in size, shape, targeting mechanism, therapeutic action and imaging modality. However, few common key features can be recognized: (I) *a component or moiety for imaging* that enables the diagnostic functionality. Common examples are metallic or magnetic compound for magnetic resonance imaging, fluorescent reporters for optical imaging or radio-isotopes for positron emission tomography or single-photon emission computed tomography. (II) a *coating portion* to confer stability, solubility, bio-compatibility, providing the possibility to insert specific groups for conjugations with other functional components. Polymers or surfactants are common examples of coating portions, e.g. forming liposomal of micellar structures or used for the coating of nanoparticles. (III) *drug loading ability* that enables the therapeutic functionality. The interaction with the therapeutic agent can be physical, e.g. through encapsulation of the drug in a polymer matrix, or through the location of a hydrophobic drug in the lipid phase of liposomes or micelles; or chemical, e.g. through a covalent link to a specific group of the carrier portion. Controlled release or activation of the therapeutic agent in response to a specific parameter like pH, temperature, light, ultrasounds or a chemical species, is preferable to impart selectivity and minimize invasiveness [61] [56].

1.6 Chapter Bibliography

1. Bransden, B. H. & Joachain, C. J. *Quantum Mechanics (2nd Edition)*. (Pearson Education Limited, 2000).
2. Eisberg, R. M. & Resnick, R. *Quantum Physics of Atoms, Molecules, Solids, Nuclei and Particles*. (Wiley, 1985).
3. Michl, J. in *Handbook of Photochemistry, Third Edition* 1–47 (Taylor & Francis, 2006).
4. Yersin, H. & Finkenzeller, W. J. in *Highly Efficient OLEDs with Phosphorescent Materials* 1–39 (WILEY-VCH Verlag, 2008).
5. Braslavsky, S. E. Glossary of terms used in photochemistry, 3rd edition (IUPAC Recommendations 2006). *Pure and Applied Chemistry* **79,** 293 (2007).
6. El-Sayed, M. A. Triplet state. Its radiative and nonradiative properties. *Acc. Chem. Res.* **1,** 8–16 (1968).
7. Cotton, F. A., Wilkinson, G. & Gaus, P. L. *Principi di chimica inorganica*. (CEA, 1991).
8. Schweitzer, C. & Schmidt, R. Physical Mechanisms of Generation and Deactivation of Singlet Oxygen. *Chem. Rev.* **103,** 1685–1758 (2003).
9. Laing, M. The three forms of molecular oxygen. *J. Chem. Educ.* **66,** 453 (1989).
10. Weldor, D., Poulsen, T. D., Mikkelsen, K. V & Ogilby, P. R. Singlet Sigma: The ‘Other’ Singlet Oxygen in Solution. *Photochem. Photobiol.* **70,** 369–379 (1999).
11. Lang, K., Mosinger, J. & Wagnerová, D. M. Photophysical properties of porphyrinoid sensitizers non-covalently bound to host molecules; models for photodynamic therapy. *Coord. Chem. Rev.* **248,** 321–350 (2004).
12. Wilkinson, F. & Brummer, J. G. Rate constants for the decay and reactions of the lowest electronically excited singlet state of molecular oxygen in solution. *J. Phys. Chem. Ref. Data* **10,** (1981).
13. Bannister, T. T. Photoreduction of Chlorophyll a in the Presence of Ascorbic Acid in Pyridine Solutions. . *Plant Physiol.* **34,** 246–254 (1959).
14. Beddard, G. S., Davidson, R.S. & Trethewey Quenching of chlorophyll fluorescence by [beta]-carotene. *Nature* **267,** 373–374 (1977).
15. Schmidt, R. Photosensitized Generation of Singlet Oxygen. *Photochem. Photobiol.* **82,** 1161–1177 (2006).
16. DeRosa, M. & Crutchley, R. Photosensitized singlet oxygen and its applications. *Coord. Chem. Rev.* 351–371 (2002).
17. Foote, C. S., Chang, Y. C. & Denny, R. W. Chemistry of singlet oxygen. X. Carotenoid quenching parallels biological protection. *J. Am. Chem. Soc.* **92,** 5216–5218 (1970).
18. Kramarenko, G. G., Hummel, S. G., Martin, S. M. & Buettner, G. R. Ascorbate Reacts with Singlet Oxygen to Produce Hydrogen Peroxide. *Photochem. Photobiol.* **82,** 1634–1637 (2006).
19. Foote, C. S. Mechanisms of Photosensitized Oxidation. *Science* **162,** 963–970 (1968).
20. Girotti, A. W. & Korytowski, W. in *Singlet Oxygen: Applications in Biosciences and Nanosciences* (eds. Nonell, S. & Flors, C.) 411–415 (Royal Society of Chemistry, 2016).
21. Cadet, J., Douki, T., Ravanat, J. L. & Di Mascio, P. in *Singlet Oxygen: Applications in Biosciences and Nanosciences* (eds. Nonell, S. & Flors, C.) 395–403 (Royal Society of Chemistry, 2016).
22. Michaeli, A. & Feitelson, J. Reactivity of Singlet Oxygen Towards Amino Acids and Peptides. *Photochem.*

Photobiol. **59,** 284–289 (1994).

23. Rougee, M., Bensasson, R. V, Land, E. J. & Pariente, R. Deactivation of Singlet Molecular Oxygen by Thiols and Related Compounds, Possible Protectors against Skin Photosensitivity. *Photochem. Photobiol.* **47,** 485–489 (1988).
24. Maskos, Z., Rush, J. D. & Koppenol, W. H. The hydroxylation of tryptophan. *Arch. Biochem. Biophys.* **296,** 514–520 (1992).
25. Jin, F., Leitich, J. & von Sonntag, C. The photolysis (λ = 254 nm) of tyrosine in aqueous solutions in the absence and presence of oxygen. The reaction of tyrosine with singlet oxygen. *J. Photochem. Photobiol. A Chem.* **92,** 147–153 (1995).
26. Matheson, I. B. C. & Lee, J. Quenching of photophysically formed singlet (1Δg) oxygen in solution by amines. *J. Am. Chem. Soc.* **94,** 3310–3313 (1972).
27. Hatz, S., Poulsen, L. & Ogilby, P. R. Time-resolved singlet oxygen phosphorescence measurements from photosensitized experiments in single cells: effects of oxygen diffusion and oxygen concentration. *Photochem. Photobiol.* **84,** 1284–90 (2008).
28. Ogilby, P. R. Singlet oxygen: there is indeed something new under the sun. *Chem. Soc. Rev.* **39,** 3181–209 (2010).
29. Maisch, T. *et al.* The role of singlet oxygen and oxygen concentration in photodynamic inactivation of bacteria. *Proc. Natl. Acad. Sci.* **104,** 7223–7228 (2007).
30. Ragàs, X., Agut, M. & Nonell, S. Singlet oxygen in Escherichia coli: New insights for antimicrobial photodynamic therapy. *Free Radic. Biol. Med.* **49,** 770–776 (2010).
31. Ragàs, X. *et al.* Singlet Oxygen in Antimicrobial Photodynamic Therapy: Photosensitizer-Dependent Production and Decay in E. coli. *Molecules* **18,** 2712–2725 (2013).
32. Krasnovsky, A. A., Kozlov, A. S. & Roumbal, Y. V. Photochemical investigation of the IR absorption bands of molecular oxygen in organic and aqueous environment. *Photochem. Photobiol. Sci.* **11,** 988–997 (2012).
33. Anquez, F. *et al.* in *Singlet Oxygen: Applications in Biosciences and Nanosciences* (eds. Nonell, S. & Flors, C.) 77–82 (Royal Society of Chemistry, 2016).
34. Bregnhøj, M., Blázquez-Castro, A., Westberg, M., Breitenbach, T. & Ogilby, P. R. Direct 765 nm Optical Excitation of Molecular Oxygen in Solution and in Single Mammalian Cells. *J. Phys. Chem. B* **119,** 5422–5429 (2015).
35. Gorman, A. A., Krasnovskii, A. A. & Rodgers, M. A. J. Singlet oxygen infrared luminescence: unambiguous confirmation of a solvent-dependent radiative rate constant. *J. Phys. Chem.* **95,** 598–601 (1991).
36. Jimenez-Banzo, A., Ragas, X., Kapusta, P. & Nonell, S. Time-resolved methods in biophysics. 7. Photon counting vs. analog time-resolved singlet oxygen phosphorescence detection. *Photochem. Photobiol. Sci.* **7,** 1003–1010 (2008).
37. Ruiz-González, R. & Zanocco, A. L. in *Singlet Oxygen: Applications in Biosciences and Nanosciences* (eds. Nonell, S. & Flors, C.) 105–117 (Royal Society of Chemistry, 2016).
38. Scholz, M., Biehl, A.-L., Dedic, R. & Hala, J. The singlet-oxygen-sensitized delayed fluorescence in mammalian cells: a time-resolved microscopy approach. *Photochem. Photobiol. Sci.* (2015). doi:10.1039/C4PP00339J
39. Braslavsky, S. E. & Heibel, G. E. Time-Resolved Photothermal and Photoacoustic Methods Applied to Photoinduced Processes in Solution. *Chem. Rev.* **92,** 1381–1410 (1992).

40. Redmond, R. W., Heihoff, K., Braslavsky, S. E. & Truscott, T. G. Thermal-Lensing and Phosphorescence Studies on the Quantum Yield and Lifetime of Singlet Molecular Oxygen (1Δg) Sensitized by Hematoporphyrin and Related Porphyrins in Deuterated and Non-Deuterated Ethanols. *Photochem. Photobiol.* **45,** 209–213 (1987).
41. Moan, J. & Peng, Q. in *Photodynamic Therapy* (ed. Patrice, T.) **2,** 1–18 (The Royal Society of Chemistry, 2003).
42. Agostinis, P. *et al.* Photodynamic therapy of cancer: An update. *CA. Cancer J. Clin.* **61,** 250–281 (2011).
43. Ormond, A. B. & Freeman, H. S. Dye Sensitizers for Photodynamic Therapy. *Materials (Basel).* **6,** 817–840 (2013).
44. Dougherty, T. J. *et al.* Photodynamic therapy. *J. Natl. Cancer Inst.* **90,** 889–905 (1998).
45. Jori, G. Tumour photosensitizers: approaches to enhance the selectivity and efficiency of photodynamic therapy. *J. Photochem. Photobiol. B.* **36,** 87–93 (1996).
46. Cló, E., Snyder, J. W., Ogilby, P. R. & Gothelf, K. V. Control and Selectivity of Photosensitized Singlet Oxygen Production: Challenges in Complex Biological Systems. *ChemBioChem* **8,** 475–481 (2007).
47. Alves, E. *et al.* Potential applications of porphyrins in photodynamic inactivation beyond the medical scope. *J. Photochem. Photobiol. C Photochem. Rev.* **22,** 34–57 (2015).
48. Luksienė, Z. & Zukauskas, A. Prospects of photosensitization in control of pathogenic and harmful micro-organisms. *J. Appl. Microbiol.* **107,** 1415–1424 (2009).
49. Luksiene, Z. & Brovko, L. Antibacterial Photosensitization-Based Treatment for Food Safety. *Food Eng. Rev.* **5,** 185–199 (2013).
50. Abrahamse, H. & Hamblin, M. R. New photosensitizers for photodynamic therapy. *Biochem. J.* **473,** 347–364 (2016).
51. Kessel, D. & Reiners, J. J. Apoptosis and Autophagy After Mitochondrial or Endoplasmic Reticulum Photodamage. *Photochem. Photobiol.* **83,** 1024–1028 (2007).
52. Jori, G., Camerin, M., Soncin, M., Guidolin, L. & Coppellotti, O. in *Photodynamic Inactivation of Microbial Pathogens: Medical and Environmental Applications* **11,** 1–18 (The Royal Society of Chemistry, 2011).
53. Hamblin, M. R. & Hasan, T. Photodynamic therapy: a new antimicrobial approach to infectious disease? *Photochem. Photobiol. Sci.* **3,** 436–450 (2004).
54. Sperandio, F. F., Huang, Y.-Y. & Hamblin, M. R. Antimicrobial Photodynamic Therapy to Kill Gram-negative Bacteria. *Recent Pat Antiinfect Drug Discov* **8,** 1–23 (2013).
55. Kharkwal, G. B., Sharma, S. K., Huang, Y.-Y., Dai, T. & Hamblin, M. R. Photodynamic therapy for infections: Clinical applications. *Lasers Surg. Med.* **43,** 755–767 (2011).
56. Planas, O. *et al.* in *Photochemistry: Volume 42* **42,** 233–278 (The Royal Society of Chemistry, 2015).
57. Mauro, M., Aliprandi, A., Septiadi, D., Kehr, N. S. & De Cola, L. When self-assembly meets biology: luminescent platinum complexes for imaging applications. *Chem. Soc. Rev.* **43,** 4144–4166 (2014).
58. Strassert, C. A. *et al.* Switching on luminescence by the self-assembly of a platinum(II) complex into gelating nanofibers and electroluminescent films. *Angew. Chemie - Int. Ed.* **50,** 946–950 (2011).
59. Lammers, T., Aime, S., Hennink, W. E., Storm, G. & Kiessling, F. Theranostic Nanomedicine. *Acc. Chem. Res.* **44,** 1029–1038 (2011).
60. Bardhan, R., Lal, S., Joshi, A. & Halas, N. J. Theranostic Nanoshells: From Probe Design to Imaging and Treatment of Cancer. *Acc. Chem. Res.* **44,** 936–946 (2011).

61. Caldorera-Moore, M. E., Liechty, W. B. & Peppas, N. A. Responsive Theranostic Systems: Integration of Diagnostic Imaging Agents and Responsive Controlled Release Drug Delivery Carriers. *Acc. Chem. Res.* **44,** 1061–1070 (2011).

62. Foote, C. S. Definition of type I and type II photosensitized oxydation. *Photochem. Photobiol.* **54,** 695 (1991).

2 Aim of the work: proteins as carriers for photo-physically active molecules in biosystems

2.1 Proteins

In nature, many proteins have a carrier function. Carrier proteins are able to interact with a molecule (ligand) or a class of molecules at a specific binding site, with a binding equilibrium that is often sharply modulated according to the environment. Probably the most well-known carrier proteins are albumins that constitute the most abundant fraction of plasma proteins. They are rather a-specific carriers, able to bind chemically different molecules, and they are extremely important in determining the pharmacokinetics of a drug [1]. Proteins belonging to the globin superfamily, like hemoglobin or myoglobin, are other ubiquitous carrier proteins whose primary function concerns the storage and transport of gaseous ligands like O_2 or NO. The binding of these gases occurs at the metal center of the prosthetic heme group, which is based on a tetrapyrrole ring structure. Proteins belonging to the family of lipocalins are another example of wide-spread diversified proteins able to bind and carry small hydrophobic ligands like retinoids or lipids.

The idea at the basis of this research follows an approach typical of nanomedicine where the structure of these proteins is viewed as a nanostructured scaffold, suitable for the conjugation with active drugs. Due to their biological function of carriers, protein-based nanostructures show interesting potential as theranostic agents. Indeed, the properties of some carrier proteins match the distinctive traits of the *coating portion* in a theranostic formulation (see 1.5):

- *nano-size*: globular proteins like albumins, globins or lipocalins typically have a size of ~10 nm, that is less than many other theranostic carriers like nanoparticles or liposomes;
- *water-solubility*: cytoplasmic proteins live in water and several carrier proteins are stable at relatively high concentrations in physiological environment. They do not require any coating or chemical modification to avoid precipitation.
- *bio-compatibility*: if carrier proteins are spontaneously present in a biosystem, their use as drug delivery agents avoids the introduction of additional exogenous products.
- *reproducibility and availability*: many common carrier proteins are easily available in large amounts with a high level of purity. Their well-defined structure ensures homogeneity in size, weight and properties. This is an advantage over other systems, e.g. micelles or liposomes, for which the achievement of mono-disperse, homogeneous populations may be non-trivial.
- *flexibility*: proteins can be engineered for the improvement of a specific property, e.g. the preferential interaction with a cellular target or the conjugation with a specific compound.

These modifications can be obtained with chemical reactions involving specific groups in the side chains of amino acids or through the expression of mutants and chimeric structures. The possibility and the ease of introducing modifications is variable depending on the specific type of protein.

- *selectivity*: some proteins spontaneously show preferential interaction with membranes or with the surface of some types of cells. Modifications may improve the selectivity.
- *loading with a drug*: this is a distinctive feature of a theranostic carrier. If the active drug is sterically and chemically similar to the native ligand, it will be likely to interact with a significant affinity at the protein's binding site.

In this work, three wide-spread proteins belonging to three distinct classes of proteins, i.e. albumins, globins and lipocalins, were used. As previously mentioned, for the purpose of this research, these proteins were not addressed to elucidate their biological function or their enzymatic behavior. They were rather intended as basic nanostructures for the development of theranostic formulations. *Apo-myoglobin* (apoMb) from horse heart, namely myoglobin deprived of the natural heme cofactor, and bovine *β-lactoglobulin* (βLG), respectively belonging to the globin and lipocalin families, constituted the main object of investigation. *Bovine Serum Albumin* (BSA), was occasionally used as a sort of reference protein, since it is known to interact with a wide range of compounds. ApoMb and βLG were chosen because they are wide-spread and well-known representative of their respective families. They can be both generically considered as carrier proteins, even if they are extremely different from several points of view like structure, origin, function and solvation properties. Few important aspects are sketched below:

- *structure*: apoMb (~17000 Da) is a small globular protein characterized by the typical eight α-helix strands folding of globins that wraps a main hydrophobic pocket able to accommodate the heme. βLG (~18400 Da) is found in two slightly different isoforms A and B, differing for three amino acid residues. It shows the typical eight-stranded β-barrel folding of lipocalins that encloses an internal hydrophobic cavity, suitable for the binding of linear hydrocarbon portions of molecules. A pH-sensitive loop act as a gate over the binding site (Tanford transition) [2]. βLG is often found as a homodimer in its native conditions [3] [4]. The structure of the dimer shows two additional hydrophobic clefts, located at the interface between the monomers. The B isoform was used in this work.
- *origin and function*: myoglobin, from which apoMb is obtained, is an abundant cytoplasmic protein found in the cardiac and skeletal muscles of all vertebrates [5]. Its primary function is to facilitate O_2 diffusion, even if a more complex allosteric functionality [6] [7] and a role in

NO scavenging have been proposed [8]. βLG is the most abundant protein of cow's milk whey, and it is responsible also for a significant allergenic response in some humans. The biological function(s) of this protein has not yet been clearly identified even if the presence of the internal cavity suggests a carrier functionality [9] [4] [3].

- *solvation*: myoglobin is soluble in aqueous media up to concentration of ~1 mM. ApoMb can be easily obtained from the native protein in large amounts and it is sufficiently stable for experiments or applications. It presents several charged residues on its surface, rather homogeneously distributed, so that its isoelectric point (pI) is of 7.2. The protein is thus surrounded by a solvation shell even if its net charge is close to zero in physiological conditions. Reconstitution of myoglobin from apoMb by titration with heme or other porphyrin compounds, e.g. Zn-protoporphyrin IX, is possible [10]. βLG is readily soluble in aqueous buffers up to concentrations close to mM, even though it tends to form dimers and oligomers at physiological concentrations (at 100 µM, the concentration in milk whey, the protein is fully dimeric). Solvation properties of this protein are unusual. It indeed results extremely resistant to denaturation induced by polar organic solvents like DMSO, retaining the native structure up to DMSO concentrations of 50-60% [11]. Recent studies based of Tera-Hertz spectroscopy showed that βLG is a relatively hydrophobic protein, since it does not display long-range hydration dynamics, as observed for other hydrophilic proteins [12] [13] [14].

2.2 Photo-physically active compounds

Some photo-physically active molecules were tested as functional components to be conjugated with the protein-based nanostructured scaffold. In the purposes of this research, the attention was mainly focused on PSs as active compounds. The resulting theranostic formulations were then meant to exploit photosensitization as therapeutic action. Additionally, two specific Pt-based triplet emitters were tested as active components, and showed interesting potential as tool for noninvasive bio-imaging rather than for theranostic applications.

Few representative PSs were selected for the experiments. The primary requirement for the choice of the PS is the possibility to be efficiently loaded on the protein-based structure. Additionally, naturally-occurring PSs were preferred in this work since they are well-known, easy to purchase, with no need of synthetic preparation and relatively safe. It must be pointed out that, although the present research was restricted to few natural compounds, several other PSs belonging to diverse classes (see 1.3.2) are potentially suitable for the development of similar theranostic formulations. Indeed, the properties required are quite common. Some of them are reported below:

- *hydrophobicity*: this is a critical issue regarding photo-physically active molecules since many of them show completely or partially hydrophobic structures. Accordingly, many common PSs are poorly soluble under physiological conditions and form aggregates in aqueous solvents. Aggregation often constitutes a relevant problem for bio-applications since it promotes fast non-radiative $S_1 \rightarrow S_0$ relaxations of the photo-excited molecule, impairing important photo-physical properties, like fluorescence emission or triplet state formation, and making the molecule substantially inactive. Thus hydrophobic PSs are photo-active only when they are solubilized by a structure that counteracts their aggregation. In the formulations developed in this work, the solubilizing structure was constituted by the protein-based nanostructure. It must be specified that several hydrophobic PSs, e.g. porphyrins, are spontaneously and a-specifically solubilized by membranes in the cell environment, where they recover functionality. However, the use of a nano-carrier system is always preferable since it allows a more controlled delivery.
- *binding with the protein*: this is the crucial requirement. Since hydrophobic PSs were used, the interaction occurred spontaneously at the hydrophobic cavities of the selected proteins. The affinity of the two species is variable according to the accessibility of the binding site and the steric and chemical properties of the PS. Beside hydrophobic effect, some PS showed a specific strong chemical affinity to the protein. It was the case of the Zn-protoporphyrin IX, whose metal ion could be coordinated by the proximal Histidine residue of apoMb. Unlike other theranostic formulations, the binding of the PS to the protein-based structure often occurs with a 1:1 stoichiometry thus allowing a precise control of the drug doses.
- *therapeutic and diagnostic functionality*: in these protein-based formulations, the aggregation of the hydrophobic active compound is limited or prevented by the binding with protein matrix. This fact has important consequences on the functionality of the molecule. First the protein-bound PS is monomeric and thus solubilized in the aqueous environment, it is stable and embedded in a bio-compatible system. More importantly, the PS recovers its ability to photosensitize the production of $^1O_2$ and its ability to emit fluorescence, that is almost completely lost in the aggregated form. Consequently, the nanostructured system offers, in a single molecular species, a therapeutic functionality, based on photosensitization, and a diagnostic functionality based on fluorescence emission. So that it can be considered a real theranostic formulation to all practical purposes.

It should be pointed out that, in these formulations, the PS constitutes the only active component, retaining both the therapeutic and the diagnostic potential within the same molecule. This may be not ideal since fluorescence and photosensitization are competitive processes. Thus compounds that are efficient $^1O_2$ generators are likely to be poorly fluorescent. However, the direct emission of fluorescence by the therapeutically active compound constitutes an advantage for achieving a precise imaging. Indeed, no need to introduce additional fluorescent reporters bound to the nanostructure is required. Since there is no spatial separation between the active compound and the fluorescent tag, the imaging resolution can be pushed to its limit without running into systematic errors. It will be shown in the following that it has been indeed possible to image a PS with super-resolution microscopy techniques. This is of particular importance since it opens the possibility to identify with a resolution of tens of nm, the localization of a PS at the cellular level, that appears to be the most important parameter for the efficacy of photosensitization-based treatments (see 1.3). Additionally, the versatility of some protein-based nanostructures may allow the labelling with an additional fluorescent reporter, thus potentially enabling the possibility of co-localize the active component (PS) and the carrier portion in the same experiment, directly monitoring the process of drug release.

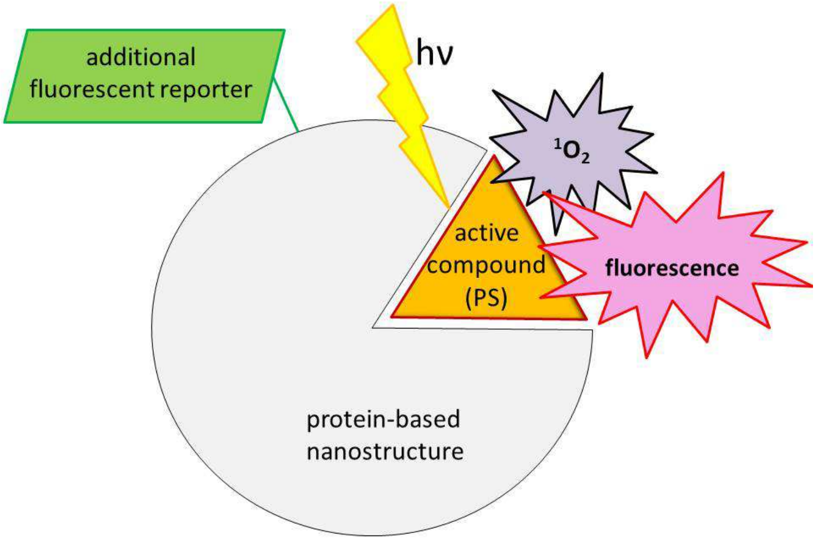

Fig. 2-1 *Schematic representation of a protein-based theranostic formulation exploiting a PS as photo-physically active compound.*

2.3 Chapter bibliography

1. Jacobson, O., Kiesewetter, D. O. & Chen, X. Albumin-Binding Evans Blue Derivatives for Diagnostic Imaging and Production of Long-Acting Therapeutics. *Bioconjug. Chem.* (2016). doi:10.1021/acs.bioconjchem.6b00487
2. Tanford, C., Bunville, L. G. & Nozaki, Y. The Reversible Transformation of β-Lactoglobulin at pH 7.51. *J. Am. Chem. Soc.* **81,** 4032–4036 (1959).
3. Kontopidis, G., Holt, C. & Sawyer, L. Invited Review: β-Lactoglobulin: Binding Properties, Structure, and Function. *J. Dairy Sci.* **87,** 785–796 (2015).
4. Mercadante, D. *et al.* Bovine β-Lactoglobulin Is Dimeric Under Imitative Physiological Conditions: Dissociation Equilibrium and Rate Constants over the pH Range of 2.5–7.5. *Biophys. J.* **103,** 303–312 (2012).
5. Ordway, G. A. & Garry, D. J. Myoglobin: an essential hemoprotein in striated muscle. *J. Exp. Biol.* **207,** 3441 LP-3446 (2004).
6. Frauenfelder, H., Mcmahon, B. H., Austin, R. H., Chu, K. & Groves, J. T. The role of structure , energy landscape , dynamics , and allostery in the enzymatic function of myoglobin. *Proc. Natl. Acad. Sci.* **98,** 2370–2374 (2001).
7. Frauenfelder, H., Fenimore, P. W. & McMahon, B. H. Hydration, slaving and protein function. *Biophys. Chem.* **98,** 35–48 (2002).
8. Brunori, M. Nitric oxide moves myoglobin centre stage. *Trends Biochem. Sci.* **26,** 209–210 (2001).
9. Diarrassouba, F., Liang, L., Remondetto, G. & Subirade, M. Nanocomplex formation between riboflavin and β-lactoglobulin: Spectroscopic investigation and biological characterization. *Food Res. Int.* **52,** 557–567 (2013).
10. Ascoli, F., Rossi Fanelli, M. R. & Antonini, E. Preparation and Properties of Apohemoglobin and Reconstituted Hemoglobins. *Methods Enzymol.* **76,** 72–87 (1981).
11. Arakawa, T., Kita, Y. & Timasheff, S. N. Protein precipitation and denaturation by dimethyl sulfoxide. *Biophys. Chem.* **131,** 62–70 (2007).
12. Vondracek, H., Dielmann-Gessner, J., Lubitz, W., Knipp, M. & Havenith, M. THz absorption spectroscopy of solvated β-lactoglobulin. *J. Chem. Phys.* **141,** 22D534 (2014).
13. Ebbinghaus, S. *et al.* An extended dynamical hydration shell around proteins. *Proc. Natl. Acad. Sci.* **104,** 20749–20752 (2007).
14. Heyden, M. *et al.* Long-Range Influence of Carbohydrates on the Solvation Dynamics of Water—Answers from Terahertz Absorption Measurements and Molecular Modeling Simulations. *J. Am. Chem. Soc.* **130,** 5773–5779 (2008).

3 Materials and Methods

3.1 Materials

The photo-active molecules Hypericin (Hyp), Zinc-protoporphyrin IX (Zn-PP IX), fluorescein isothiocyanate (FITC), Rose bengal (RB), tetrakis-(4-sulfonatophenyl)-porphine (TPPS) and 5,10,15,20-tetrakis(1-methyl-4-pyridinium)porphine tetra(*p*-toluenesulfonate) (TMPyP) were purchased from HWI Analytik GmbH (Hyp) or Sigma-Aldrich (others). The triplet emitter molecules AG113 and AG97 were synthesized in the lab of Dr. C.A. Strassert at the University of Münster. The proteins Myoglobin from horse heart, βLG (isoform B) and BSA were purchased from Sigma Aldrich. For liposomes experiments 1,2-dilauroyl-*sn*-glycero-3-phosphocholine (DLCP) from Avanti Polar Lipids are used. All samples have been stored in the dark and used immediately after preparation.

3.2 ApoMb preparation

ApoMb is prepared from the holoprotein using standard biochemical procedures: heme is removed by cold (− 30 °C) acid acetone or methyl ethyl ketone methods of extraction [1]. Samples are extensively dialyzed against aqueous buffer after the extraction, centrifuged several times and suspended in phosphate buffer saline (PBS) at pH 7.4. The purity of the sample is checked spectroscopically. The concentration of the apoMb stock is calculated from the absorption at 280 nm ($\varepsilon = 15\,800\ \mathrm{cm^{-1}\ M^{-1}}$) and heme contamination is estimated from the absorption at 408 nm ($\varepsilon = 179\,000\ \mathrm{cm^{-1}\ M^{-1}}$) [2]. In all the preparations, heme contamination is typically 0.5% of the total protein content.

3.3 ApoMb reconstitution with Zn-PP IX

To reconstitute Zn-PP IX into apoMb, the dye was dissolved in a 10 mM NaOH solution and added dropwise to a PBS solution of apoMb until an equimolar concentration is reached. The whole procedure is carried out at 4 °C under dim light. The solution is kept in the dark with continuous and gentle stirring for 24 h. The sample is then centrifuged, and the supernatant is extensively dialyzed against a PBS solution. The obtained stock solution of Zinc-substituted myoglobin is spectroscopically checked to assess sample purity. A 1:1 stoichiometry between Zn-PP IX and apoMb has been regularly observed. The concentration of Zinc-substituted myoglobin is calculated from the absorption at 554 nm ($\varepsilon = 10\,400\ \mathrm{cm^{-1}\ M^{-1}}$) [3].

3.4 Liposomes preparation

DLPC liposomes are prepared according to the injection method: 10 mM (7 mg/mL) DLPC are dissolved in ethanol; the ethanolic solution (0.7 mL) is slowly injected into 20 mL of a magnetically stirred 10 mM phosphate buffer, pH 7, thermostated at 30°C, above the transition temperature (T = -1 °C for DLPC). This procedure gives small unilamellar vesicles (SUV), of mean external radius R ≈ 26 nm [4]. Hyp-loaded liposomes were prepared by adding small amounts of concentrated Hyp in dimethyl sulfoxide to the liposomal dispersions.

3.5 Labelling of BSA with FITC

Concentrated stock solution of FITC in PBS buffer pH = 7.4 are added to a solution of BSA in the same buffer until a molar ratio dye : protein of ~ 5:1. The solution is stirred overnight at 4°C and then purified by means of a disposable Sephadex PD-10 (G-25 M) column. The evaluation of the ratio dye : protein for the purified product is made spectroscopically according to a previously established method [5]. Under the considered conditions, an average number of ~ 1.7 FITC per BSA molecule is obtained.

3.6 General spectroscopic instrumentation

Absorption spectra are recorded using a Jasco V-650 or a Varian Cary 6000i. Fluorescence emission spectra are recorded with a Horiba Jobin Yvon Spex-Fluoromax or a Perkin Elmer LS50 spectrofluorometers. For steady state anisotropy studies, two Glan Taylor polarizers were placed before sample excitation and before fluorescence detection.

For the majority of the systems investigated, fluorescence decays are recorded by a Fluotime 200 time-correlated single photon counting (TCSPC) system (PicoQuant GmbH, Berlin, Germany) with pulsed LED excitation and detection via a PicoQuant's PMA 182-M single photon detector. The excitation is usually set at 450 or 375 nm.

For measurements performed on systems involving triplet emitters as photo-active molecules, a rather different detection system is used, where steady-state excitation and emission spectra as well as emission lifetimes are measured with a FluoTime300 spectrometer from PicoQuant. The spectrometer is equipped with a 300 W ozone-free Xe lamp coupled with a Czerny-Turner monochromator as steady-state excitation source and various pulsed diode lasers (pulse width < 80 ps, usually a 375 nm excitation is used) as excitation source for time-resolved measurements. An emission monochromator coupled to a UV-Vis sensitive PMA Hybrid 40 enable sensitive measurements in the UV-Vis region of the spectrum. Steady-state spectra and fluorescence lifetimes are recorded in TCSPC mode by a PicoHarp300 (channel width: min 4; max 512 ps). Longer luminescence lifetimes are recorded in Multi-Channel Scaling (MCS) mode by a NanoHarp250 (channel width: min 32 ns; max 2.15 s).

Lifetime analysis is performed using the commercial FluoFit software by PicoQuant. For ns decays a re-convolution mode is used for the fitting, where the exponential model is combined with an acquired instrument response function (IRF) and adjusted to the measured signal. The quality of the fit is assessed by minimizing the reduced chi squared function and visual inspection of the weighted residuals and their autocorrelation.

3.7 $^1O_2$ measurements

The time-resolved $^1O_2$ phosphorescence signals and Φ_Δ values are determined by direct detection of $^1O_2$ phosphorescence at 1275 nm using a modified PicoQuant Fluotime 200 system. A diode-pumped pulsed Nd:YAG laser (FTSS355-Q, Crystal Laser) working at 10 or 1 kHz repetition rate (λ_{exc} = 532 nm, 1.2 µJ per pulse) is used for excitation; the NIR luminescence from the sample is detected at 90° by a H9170-45 NIR-PMT module (Hamamatsu) working in photon counting mode and a NanoHarp 250 multichannel scaler (PicoQuant, Germany). The time-resolved phosphorescence signals, showing the typical rise and decay, are fitted with the equation:

$$S = S_0 \frac{\tau_\Delta}{\tau_\Delta - \tau_T}\left(e^{-t/\tau_\Delta} - e^{-t/\tau_T}\right) + y_0$$

where τ_T and τ_Δ are the lifetime of the photosensitizer triplet state and of $^1O_2$ respectively, y_0 is an offset due to instrument dark counts and S_0 is an instrumental quantity proportional to Φ_Δ. The value of Φ_Δ is obtained by comparison with reference PSs. Sample and references are dissolved in the same solvent and air-equilibrated. Reference concentrations were adjusted so that the value of absorbance (< 0.1) at the excitation wavelength resulted to be the same of the sample. Time-resolved signals were acquired and fitted using the above equation. The value for Φ_Δ is then retrieved comparing the S_0 values for sample and references:

$$\Phi_{\Delta,sample} = \Phi_{\Delta,ref} \frac{S_{0,sample}}{S_{0,ref}}$$

Occasionally, a slightly different method is used for the determination Φ_Δ, with the advantage that there is no necessity of adjusting the absorbances of sample and references to the same value at the excitation wavelength. For each PS (sample or reference) 5 or 6 solutions are prepared at different concentrations, with absorbance values at the excitation wavelength between 0.01 and 0.1. The time-resolved phosphorescence signals of each solution are recorded and fitted. For each PS, the S_0

values obtained were plotted against the sample absorption factor ($1\text{-}10^{-A}$), where A is the sample absorbance at the excitation wavelength. Data are well fitted using a linear model with zero intercept and Φ_Δ is then calculated comparing the slopes of sample and references:

$$\Phi_{\Delta,sample} = \Phi_{\Delta,ref} \frac{S_{A,sample}}{S_{A,ref}}$$

where $S_{A,sample}$ and $S_{A,ref}$ are the slopes obtained respectively for sample and the reference PSs [6].

3.8 Fluorescence Correlation Spectroscopy

Fluorescence Correlation Spectroscopy (FCS) experiments are performed using a Microtime 200 from Picoquant, based on an inverted confocal microscope (Olympus IX70) equipped with two SPADs (Single Photon Avalanche Diodes, Perkin Elmer) used in the cross correlation mode. Excitation was achieved by a 475 nm picosecond diode laser (pulse width ~50 ps, repetition rate 20 MHz) and fluorescence emission was collected through a bandpass filter centered at 650 nm and split with a 50/50 splitter between the two detection channels. The same setup allowed the determination of fluorescence decays occurring from the instrument's focal volume, through a TCSPC operation.

FCS is useful to determine the diffusion coefficient of molecules taking advantage of the spontaneous thermal fluctuations in the fluorescence emission intensity of freely diffusing fluorophores in solution [7] [8] [9]. For the systems under investigation, the retrieved fluorescence cross-correlation signal G(τ) is generally well described by a model comprising diffusion of one or two molecular species and a triplet decay, according to the equation:

$$G(\tau) = \left(1 - T + Te^{-\frac{\tau}{\tau_T}}\right) \cdot \frac{1}{V_{eff}\langle C\rangle} \cdot \sum_i \left(\frac{1}{(1 + \frac{\tau}{\tau_{D_i}})} \cdot \frac{1}{\sqrt{1 + (w_0/z_0)^2 \cdot \frac{\tau}{\tau_{D_i}}}} \right)$$

where ‹C› is the average local concentration of fluorophores, optimal single molecule conditions are obtained for nano-molar values; V_{eff} is the effective excitation volume (~ 1fl); w_0 and z_0 are calibration parameters corresponding to the lateral and axial radius of the focal volume respectively; τ_{Di} is the average time required for the *i*-th diffusing fluorophore to cross the focal volume; T and τ_T are respectively the fraction and the decay lifetime of molecules found in a dark state, which is a non-fluorescent state typically corresponding to the triplet. The values for the diffusion coefficient of the *i*-th species is retrieved from the diffusion time according to the equation $D_i = \frac{w_0^2}{4\tau_{D_i}}$. The analysis of the cross-correlation or TCSPC signal is performed using the commercial SymPhoTime software by PicoQuant.

3.9 Laser Flash Photolysis

Laser Flash Photolysis is used to measure the decay of molecules triplet state using a previously described setup [10]. Briefly, the sample is excited with a ns pulsed laser excitation at 532 nm generated by a Q-switched Nd:YAG Spectron laser (repetition rate 1 Hz, 5 mJ per pulse). The transient T-T absorption following the photo-excitation is monitored with a probe beam oriented at 90° with respect to the excitation beam. The probe light is generated by a Xe arc lamp and the detection wavelength is selected by means of two monochromators placed before and after the sample. The transmitted light is collected by a PMT coupled to a digital oscilloscope. A baseline is acquired in absence of the probe light and subtracted to the signal, then the time-resolved differential absorbance $\Delta A(t)$ is calculated and fitted with an exponential model.

3.10 Femtosecond transient absorption spectroscopy

The experimental set-up was described previously [11] [12]. Briefly, it is based on an amplified Ti:sapphire laser system delivering pulses with time duration of ~100 fs. The output is frequency doubled for exciting the sample at 400 nm (pump energy = 0.15 μJ per pulse), while the time evolution of the photo-excited sample is monitored by a second spectrally broad UV-visible pulse, the white continuum probe pulse, generated by focusing the fundamental beam on a calcium fluoride plate. The probe pulse is delayed with respect to the pump by means of a suitable optical line that allows to scan a time interval up to 2 ns after excitation. The repetition rate of the laser system is set at 100 Hz and the sample is kept under continuous stirring by means of a small magnet inside the cuvette (path length = 2 mm). All the measurements are carried out by setting the relative pump-probe polarization at the magic angle (54, 7°). The detection system consists of two linear CCD arrays (Hamamatsu S8377-256Q), coupled to a spectrograph (Jobin Yvon CP 140-1824) and controlled by a home-made front-end circuit. The signals are fed into a simultaneous analog-to-digital conversion board (Adlink DAQ2010) and data are acquired by means of a LabVIEW written computer program. By repeating the sequence as a function of the pump-probe delay, it is possible to obtain the dynamical evolution of the transient absorbance $\Delta A(\lambda, t)$. Kinetics extracted at different wavelengths are fitted with a multi-exponential function, convoluted with a Gaussian instrumental function (FWHM = 160 fs). Furthermore, global analysis [13] of kinetics recorded in the whole probed spectral range were applied. A sequential model was used to extract the spectral features of interest, associated with each transient.

3.11 STED nanoscopy

Stimulated emission depletion (STED) nanoscopy has been performed using a custom made setup equipped with a supercontinuum pulsed laser source (ALP-710-745-SC, Fianium LTD). The excitation wavelength is selected by means of an acusto-optic tunable filter, while the STED wavelength is predefined by the laser outputs. The laser has a repetition frequency of 20 MHz and a pulse width of about 100 ps. In all the reported experiments, a 566 nm wavelength is used for excitation and a 715 nm for STED. The doughnut shape of the STED beam is realized by a vortex phase plate (RPC photonics inc.). The beams are scanned on the sample by galvanometer mirrors (Till-photonics, FEI Munich GmbH), focused by a HCX PL APO CS 100x 1.4NA oil (Leica Microsystems) objective. Fluorescence is collected by an avalanche photodiode (SPCM-AQRH-13-FC, Excelitas Technologies) in the spectral window 670 – 640 nm.

In order to study the STED efficiency the fluorescence depletion curve is measured. For this experiment the STED beam is Gaussian shaped and several images are acquired varying the STED power. The resulting fluorescence depletion curves were described by the following equation [14] [15] and the data fitted accordingly:

$$DC = (1-\alpha)DC(I_{STED}) + \alpha$$

$$DC(I_{STED}) \approx \frac{1 + \frac{I_{STED}}{I_S}\exp\left(-k_{S1}\tau_{STED}\left(1+\frac{I_{STED}}{I_S}\right)\right)}{1+\frac{I_{STED}}{I_S}}$$

Where α is an additive constant describing the level of non-saturable fluorescence, I_{STED} is the STED beam power, I_S is the intensity of the STED beam at which the rate of stimulated emission equals the spontaneous decay, k_{S1} is the spontaneous decay rate and τ_{STED} is the STED pulse width.

3.12 Confocal microscopy

Cell suspensions in sterile PBS were drop-casted on a coverslip and imaged by means of an A1r MP NIKON confocal microscope (Nikon Instruments). The samples were excited by focusing a laser beam through a Plan Apo vc 100×, 1.4 NA oil immersion objective. The fluorescence was collected by the same lens and detected in the spectral window between 600 and 670 nm by means of a GaAsP photomultiplier tube (PMT), whereas the transmitted laser light was detected by a PMT through a condenser lens.

3.13 Spinning disk microscopy

Cell suspensions in transparent medium containing the photosensitizing agent are imaged by means of a Yokogawa CSU-X1 spinning disk confocal unit mounted on a TiE inverted microscope by NIKON (Nikon Instruments). The emission is collected with an iXon EMCCDs (Andor Technology). The system is equipped with an Okolab incubation system, suitable to image living cells.

3.14 Binding isotherm

The binding of Hyp to a protein-based structure is monitored with an experiment where a Hyp solution in buffer is titrated with increasing protein concentration, obtained adding small aliquots of a concentrated protein solution in the same buffer under constant experimental conditions and fixed temperature. For each concentration, a fluorescence emission spectrum is collected and the values of the integrated fluorescence emission, corrected by the dilution factor, are reported as a function of the protein concentration (binding isotherm). Assuming that unbound Hyp in the aqueous buffer is negligibly fluorescent, the observed fluorescence emission is proportional to the amount of complex Hyp-protein. The values of the association K_a or dissociation K_d constant for the complex formation are retrieved by a fitting of the binding isotherm curve with a model considering the chemical equilibrium:

$$\mathrm{Hyp} + \mathrm{protein} \rightleftarrows \mathrm{complex}$$

The association constant is defined as:

$$K_a = \frac{[comp]}{[pr][Hyp]}$$

where:

$$[pr] = [pr]_{tot} - [comp]$$

$$[Hyp] = [Hyp]_{tot} - [comp]$$

An expression for the complex concentration at the equilibrium is obtained:

$$[comp] = \frac{1}{2K_a}\left(K_a[pr]_{tot} + K_a[Hyp]_{tot} + 1 - \sqrt{(K_a[pr]_{tot} + K_a[Hyp]_{tot} + 1)^2 - 4{K_a}^2[pr]_{tot}[Hyp]_{tot}}\right)$$

In the presence of a large excess of protein with respect to Hyp, a condition that often occurs in the systems under study, the expression can be simplified to:

$$[comp] \approx \frac{K_a[pr]_{tot}[Hyp]_{tot}}{1 + K_a([pr]_{tot}+[Hyp]_{tot})}$$

The measured integrated fluorescence emission F can be expressed as:

$$F = F_{comp}[comp] + F_{Hyp}[Hyp]$$

where F_{comp} and F_{Hyp} are scaling factor proportional to the fluorescence quantum yields of the complex and unbound Hyp respectively [16]. Since unbound Hyp is negligibly fluorescent $F_{comp} >> F_{Hyp}$ and the term containing F_{Hyp} can be accordingly neglected.

3.15 Microbial growth and photo-inactivation

Three bacterial strains have been used in this work: *E. coli* CECT101 and *S. aureus* CECT239 both obtained from the Spanish Type Culture Collection (CECT) and *B. subtilis* 168WT, a kind gift of Dr. Wolfgang Gärtner (MPI for Chemical Energy Conversion, Mülheim a.d. Ruhr, Germany). Vegetative bacterial cells are grown in sterile Triptic Soy Broth (*E. coli* and *S. aureus*) or in Brain Heart Infusion broth (*B. subtilis*) at 37°C until an optical density at 600 nm corresponding to 0.4 (*E. coli* and *S. aureus*) or 0.5 (*B. subtilis*). After the incubation period, the cells suspensions were washed three times in sterile PBS by means of centrifugation and resuspension and then incubated in the dark with the photosensitizing agent for 30 min at room temperature (*E. coli* and *S. aureus*) or for 90 min at 37°C (*B. subtilis*). Spectroscopic measurements are performed just after the incubation period. Photo-inactivation experiments are performed according to a previously described standard method [16] [17]: after the incubation period the suspensions are placed in 96-wells plates, irradiated with green light for 15 or 30 min (18 and 37 J/cm^2) and serially diluted until 10^{-6} times the original concentration. The diluted samples are seeded on Triptic Soy (or Brain Heart Infusion) agar and colony forming units (CFUs) are counted after ~24 h incubation in the dark at 37°C to calculate the survival fraction. Experiments were carried out in duplicate.

3.16 Tumor cell cultures and viability essays

All culture media and supplements were purchased from Euroclone. PC3 cells and HeLa cells were obtained from ECACC. Dimethyl thiazolyl diphenyl tetrazolium (MTT) was purchased from Applichem. PC3 human prostate adenocarcinoma cells are grown in Ham F12, supplemented with 5% FBS and 1% penicillin-streptomycin solution. HeLa human cervical cancer cells are grown in EMEM supplemented with 1% antibiotic solution, 1% glutamine, 1% non-essential aminoacid solution and 10% FBS. Both the cell lines were maintained in a humidified atmosphere of 95% air, 5% CO_2 at 37°C.

MTT assay is used to evaluate PC3 and HeLa viability. Cells are seeded in 96-well cell culture plates at the density of $3x10^5$ cells/ml and the day after, they are starved and treated with different concentrations of photosensitizing agent and controls, avoiding the exposure to natural light. Immediately after the treatment, cells are exposed to light for different times and then maintained for 24 hours in a humidified atmosphere with 5% CO_2 at 37°C, without light exposure. MTT is finally added at the concentration of 1 mg/ml and incubated for 2 hours. The resulting formazan crystals were solubilized with DMSO and the absorbance was measured at 550 nm using an ELISA plate reader (Sunrise, TECAN).

3.17 Modeling

3.17.1 ApoMb-Hyp

Formation of the apoMb–Hyp complex is modelled by the AutoDock software. A Lamarckian algorithm is used to search the different conformations with a semi empiric force field for the energy estimation (10 iterations).

3.17.2 2βLG-Hyp: docking

The molecular modeling studies were performed by the group of prof. F. Javier Luque at the University of Barcelona (Spain). The protein model for the bovine βLG dimer is derived from the X-ray crystallographic structure (PDB entry 1BEB) [18]. The structure is refined by including addition of hydrogen atoms using the xLEAP facility in AMBER12 and the parm99SB force field, removal of non-standard residues (sulphate anion) and generation of the disulfide bonds Cys66-Cys160 and Cys106-Cys119. Since the N- and C-terminal segments are not observed in the X-ray structure, N-methylamine and acetyl capping groups are added to the C- and N-terminus, respectively.

The binding of Hyp is explored by means of docking calculations carried out with GLIDE [19] [20]. Since the size of Hyp precludes its binding to the cavity shaped in the interior of the lipocalin-type β-barrel, docking is performed in the two pockets formed at the interface of the monomers in the dimeric complex. The first pocket includes the solvent-exposed residues inside a cube of 39300 $Å^3$, centered between side chains of residues Arg148 of one monomer and Asp137 of the other. The second cavity is defined by the exposed residues inside a cube of the same size centered at the midpoint of the segment that connects the side chains of residue Trp61 in each monomer. Default settings are used and the best poses are clustered according to the RMSD between its heavy atoms using a threshold of 2.0 Å and subsequently re-evaluated using the Glide-XP scoring function.

3.17.3 2βLG-Hyp: molecular dynamics

The binding mode derived from docking studies is further checked by means of Molecular Dynamics (MD) simulations of the complex between 2βLG and Hyp. GPU accelerated PMEMD [21] module from the AMBER12 software package is used to run the simulations. The Parm99SB force field is used for the protein, the gaff force field [22] is used to assign parameters to Hyp and Joung and Cheatham parameters were used to describe the counterions [23]. The ligand charge distribution is determined from a fit to the HF/6-31G(d) electrostatic potential obtained with Gaussian09 using the RESP [24] protocol as implemented in the Antechamber module of AmberTools 1.5 software package.

The simulated system includes the complex between the dimeric protein and the ligand, the crystallographic solved water molecules, and 16 Na+ cations, added to neutralize the system prior to solvation in a truncated octahedral box of TIP3P water molecules[25]. The final system comprise around 72000 atoms, including around 22000 water molecules. The geometry of the system is minimized in four steps. First, water molecules are refined though 4500 steepest descent algorithm followed by 10500 steps of conjugate gradient. Then, protein and ligand hydrogen atoms positions are optimized using 500 steps of steepest descent and 4500 of conjugate gradient. Next the ligand, water molecules and counterions are further optimized with 2000 steps of steepest descent and 6000 of conjugate gradient and, finally the whole system is optimized with 2500 steps of steepest descent and 4500 of conjugate gradient. At this point, 3 different replicas are generated by randomly assigning 3 different sets of velocities to the initial coordinates, all fitting a Maxwell distribution for a temperature of 50 K. For each one of the replicas, thermalization is performed in the NVT ensemble during five 25 ps steps, using a time step of 1 fs and increasing the temperature from 50 to 298 K. Concomitantly, the inhibitor and the residues in the binding site are restrained during thermalization using a variable restraint force. Thus, a force constant of 5 kcal mol^{-1} $Å^{-2}$ is used in the first stage of thermalization, and is subsequently decreased by increments of 1 kcal mol^{-1} $Å^{-2}$ in the next stages. Prior to the production runs, a short MD simulation of 1 ns in the NPT ensemble is conducted in order to allow the system to achieve a stable density value at 1 bar. For each replica, an 50 ns production trajectories is run using SHAKE for bonds involving hydrogen atoms, allowing for a timestep of 2 fs, in conjunction with periodic boundary conditions at constant volume and temperature (298 K; Langevin thermostat with a collision frequency of 3 ps^{-1}), particle mesh Ewald for long-range electrostatic interactions, and a cutoff of 10 Å for nonbonded interactions.

3.17.4 2βLG-Hyp in PBS-DMSO solvent

Set up of the DMSO/Water (17% v/v) solvent box. Following the procedure reported by Alvarez and Barril [26], a single molecule of DMSO is built using the Molecular Operating Environment (MOE) and optimized to the HF/6-31G(d) level of theory using Gaussian 09. Partial charges are derived for the optimized structure using the RESP procedure [27] [24] and atom types are assigned according to the General Amber Force Field [22] using Antechamber. The initial DMSO-water (17% v/v) box is obtained by solvating 6 DMSO molecules in a box of 88 TIP3P [25] [28] water molecules, minimized (3500 steps of steepest descent followed by 6400 steps of conjugate gradient) and thermalized in three steps of 100 ps where the temperature is gradually increased from 50 K to 298 K in the NVT ensemble. Then, the volume of the box is equilibrated under constant pressure and temperature in two stages of 100 ps. Throughout all pre-equilibration stages temperature is controlled by a Langevin thermostat with a collision frequency of 3 ps^{-1}; long-range electrostatics are treated using particle mesh Ewald summation; a cutoff of 4 Å is applied to all non-bonded interactions, and SHAKE [29] is employed to constraint all bonds involving hydrogen atoms. All simulations on this stage are performed with the sander module of AmberTools15.

Set up of simulation systems. The βLG dimer is constructed from the X-ray crystallographic structure 1BEB deposited in the Protein Data Bank, while the previously reported docking-derived model is used as starting structure to build the 2βLG-Hyp complex. Two disulfide bridges (Cys66-Cys160 and Cys106-Cys119) are set up on each monomer of βLG. The simulated system is solvated on a truncated octahedron box of TIP3P water molecules and the appropriate number of Na$^+$ counterions is added to neutralize the total charge. The ff14SB-ildn force field [30] is used for the protein, while Hyp is parameterized using the General Amber Force Field in conjunction with RESP (HF/6-31G(d)) charges, and Joung and Cheatham[31] [23] parameters to model the counterions, as implemented in the Antechamber module of AmberTools15 software package. Each system comprises around 60000 atoms, including the protein-ligand complex, 900 DMSO molecules, 14000 water molecules and 9 Na$^+$ counterions in a simulation box of 625 000 Å^3

The geometry of the system is minimized in five cycles that combined 3500 steps of steepest descent algorithm followed by 6500 of conjugate gradient. Thermalization is performed in 3 steps of 125 ps, where the temperature is gradually increased from 50 K to 298 K, while the protein and ligands are restrained with a force constant that is concurrently reduced from 1 kcal mol^{-1} Å^{-2} to 0.1 kcal mol^{-1} Å^{-2}. Prior to the production runs, each system is subjected to a 0.5 ns simulation on the NPT ensemble to equilibrate the density of the system. During the thermalization and equilibration stages a timestep of 1 fs is employed using SHAKE to constraint bonds involving hydrogen atoms. The productions runs consist of 250 ns using SHAKE for bonds involving hydrogen atoms, a time step of 2 fs, periodic boundary conditions at constant volume and temperature (298 K; Langevin thermostat with a collision frequency of 3 ps^{-1}), particle mesh Ewald to handle long-range electrostatic interactions, and applying a cutoff of 10 Å to all nonbonded interactions. Sander module is employed for the minimization stage, while the CUDA accelerated version of PMEMD [21] is used thorough the heating, equilibration and production stages, both modules being available in the standard distribution of AMBER15.

3.18 Chapter Bibliography

1. Ascoli, F., Rossi Fanelli, M. R. & Antonini, E. Preparation and Properties of Apohemoglobin and Reconstituted Hemoglobins. *Methods Enzymol.* **76,** 72–87 (1981).
2. Harrison, S. C. & Blout, E. R. Reversible Conformational Changes of Myoglobin and Apomyoglobin Reversible Conformational Changes and Apomyoglobin of Myoglobin. **240,** 299–303 (1965).
3. Lepeshkevich, S. V *et al.* Photosensitized Singlet Oxygen Luminescence from the Protein Matrix of Zn-Substituted Myoglobin. *J. Phys. Chem. A* **118,** 1864–1878 (2014).
4. Kremer, J. M. H., Van der Esker, M. W., Pathmamanoharan, C. & Wiersema, P. H. Vesicles of variable diameter prepared by a modified injection method. *Biochemistry* **16,** 3932–3935 (1977).
5. Viappiani, C. Use of nonradiative decays of extrinsic fluorophores as structural and dynamical probes in protein environments: Fluorescence quenching. *Biophys. Chem.* **50,** 293–304 (1994).
6. Nonell, S. & Braslavsky, S. E. in *Singlet Oxygen, UV-A, and Ozone* (ed. Lester Packer, H. S. B. T.-M. in E.) **Volume 319,** 37–49 (Academic Press, 2000).
7. Haustein, E. & Schwille, P. Fluorescence Correlation Spectroscopy: Novel Variations of an Established Technique. *Annu. Rev. Biophys. Biomol. Struct.* **36,** 151–169 (2007).
8. Tian, Y., Martinez, M. M. & Pappas, D. Fluorescence Correlation Spectroscopy: A Review of Biochemical and Microfluidic Applications. *Appl. Spectrosc.* **65,** 115–124 (2011).
9. Elson, E. L. Fluorescence Correlation Spectroscopy: Past, Present, Future. *Biophys. J.* **101,** 2855–2870 (2011).
10. Abbruzzetti, S. *et al.* Time-resolved methods in Biophysics. 2. Monitoring haem proteins at work with nanosecond laser flash photolysis. *Photochem. Photobiol. Sci.* **5,** 1109–1120 (2006).
11. Marcelli, A., Foggi, P., Moroni, L., Gellini, C. & Salvi, P. R. Excited-State Absorption and Ultrafast Relaxation Dynamics of Porphyrin, Diprotonated Porphyrin, and Tetraoxaporphyrin Dication. *J. Phys. Chem. A* **112,** 1864–1872 (2008).
12. Foggi, P., Neuwahl, F. V. R., Moroni, L. & Salvi, P. R. S1 → Sn and S2 → Sn Absorption of Azulene: Femtosecond Transient Spectra and Excited State Calculations. *J. Phys. Chem. A* **107,** 1689–1696 (2003).
13. van Wilderen, L. J. G. W., Lincoln, C. N. & van Thor, J. J. Modelling Multi-Pulse Population Dynamics from Ultrafast Spectroscopy. *PLoS One* **6,** e17373 (2011).
14. Vicidomini, G. *et al.* STED Nanoscopy with Time-Gated Detection: Theoretical and Experimental Aspects. *PLoS One* **8,** e54421 (2013).
15. Leutenegger, M., Eggeling, C. & Hell, S. W. Analytical description of STED microscopy performance. *Opt. Express* **18,** 26417–26429 (2010).
16. Comas-Barceló, J. *et al.* A self-assembled nanostructured material with photosensitising properties. *RSC Adv.* **3,** 17874 (2013).
17. Demidova, T. N. & Hamblin, M. R. Photodynamic Inactivation of Bacillus Spores, Mediated by Phenothiazinium Dyes. *Appl. Environ. Microbiol.* **71,** 6918–6925 (2005).
18. Brownlow, S. *et al.* Bovine β-lactoglobulin at 1.8 Å resolution — still an enigmatic lipocalin. *Structure* **5,** 481–495 (1997).
19. Friesner, R. A. *et al.* Glide: A New Approach for Rapid, Accurate Docking and Scoring. 1. Method and Assessment of Docking Accuracy. *J. Med. Chem.* **47,** 1739–1749 (2004).
20. Halgren, T. A. *et al.* Glide: A New Approach for Rapid, Accurate Docking and Scoring. 2. Enrichment Factors

in Database Screening. *J. Med. Chem.* **47,** 1750–1759 (2004).

21. Salomon-Ferrer, R., Götz, A. W., Poole, D., Le Grand, S. & Walker, R. C. Routine Microsecond Molecular Dynamics Simulations with AMBER on GPUs. 2. Explicit Solvent Particle Mesh Ewald. *J. Chem. Theory Comput.* **9,** 3878–3888 (2013).
22. Wang, J., Wolf, R. M., Caldwell, J. W., Kollman, P. A. & Case, D. A. Development and testing of a general amber force field. *J. Comput. Chem.* **25,** 1157–1174 (2004).
23. Joung, I. S. & Cheatham, T. E. Molecular Dynamics Simulations of the Dynamic and Energetic Properties of Alkali and Halide Ions Using Water-Model-Specific Ion Parameters. *J. Phys. Chem. B* **113,** 13279–13290 (2009).
24. Bayly, C. I., Cieplak, P., Cornell, W. & Kollman, P. A. A well-behaved electrostatic potential based method using charge restraints for deriving atomic charges: the RESP model. *J. Phys. Chem.* **97,** 10269–10280 (1993).
25. Jorgensen, W. L., Chandrasekhar, J., Madura, J. D., Impey, R. W. & Klein, M. L. Comparison of simple potential functions for simulating liquid water. *J. Chem. Phys.* **79,** (1983).
26. Alvarez-Garcia, D. & Barril, X. Relationship between Protein Flexibility and Binding: Lessons for Structure-Based Drug Design. *J. Chem. Theory Comput.* **10,** 2608–2614 (2014).
27. Fox, T. & Kollman, P. A. Application of the RESP Methodology in the Parametrization of Organic Solvents. *J. Phys. Chem. B* **102,** 8070–8079 (1998).
28. Price, D. J. & Brooks, C. L. A modified TIP3P water potential for simulation with Ewald summation. *J. Chem. Phys.* **121,** (2004).
29. Miyamoto, S. & Kollman, P. A. Settle: An analytical version of the SHAKE and RATTLE algorithm for rigid water models. *J. Comput. Chem.* **13,** 952–962 (1992).
30. Maier, J. A. *et al.* ff14SB: Improving the Accuracy of Protein Side Chain and Backbone Parameters from ff99SB. *J. Chem. Theory Comput.* **11,** 3696–3713 (2015).
31. Joung, I. S. & Cheatham, T. E. Determination of Alkali and Halide Monovalent Ion Parameters for Use in Explicitly Solvated Biomolecular Simulations. *J. Phys. Chem. B* **112,** 9020–9041 (2008).

4 Results and Discussion

4.1 Nanostructures based on globins: apoMb and Hyp

4.1.1 General photo-physical properties of Hyp

Hyp is one of the most powerful naturally occurring PS, its structure presents an hydrophobic core with several polar groups on the periphery. Solubility is a critical issue for the photo-physical properties of Hyp. The molecule aggregates in physiological buffers and in aqueous solutions at pH close to neutrality. In the aggregated form Hyp presents broadened and poorly defined absorption bands, while non-radiative de-activation processes prevail leading to a barely detectable fluorescence emission and negligible photosensitization ability. The molecule is readily soluble in polar organic solvents, like acetone, ethanol (EtOH), methanol or dimethyl sulfoxide (DMSO), that are less polar than water, or in phospholipid membranes. When solubilized, Hyp is photo-physically active: it presents structured and defined absorption bands, a relatively high fluorescence emission in the 600-700 nm region of the spectrum and a good ability of photo-generating $^1O_2$. [1] [2] [3]

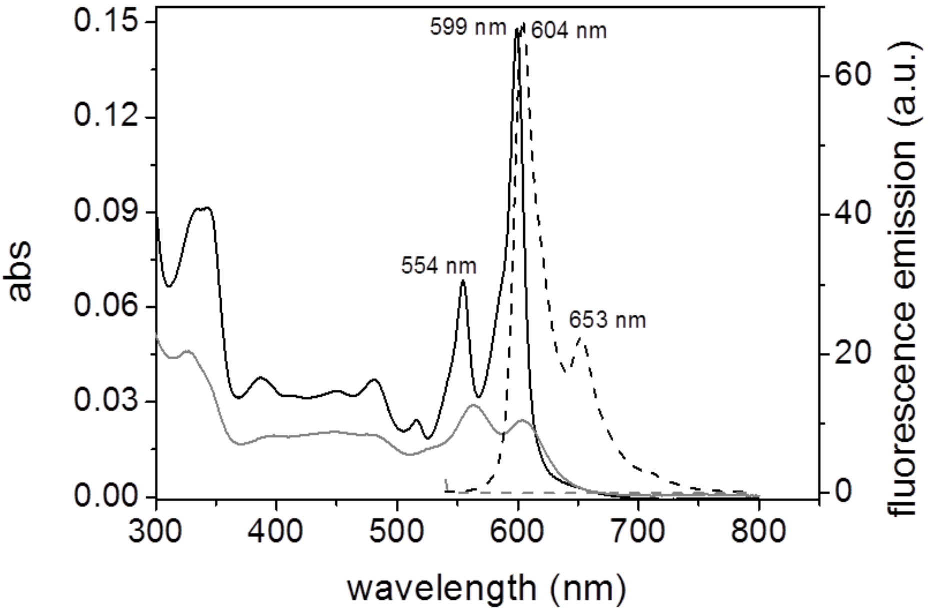

Fig. 4-1 *Absorption (solid) and fluorescence emission (dotted) spectra of Hyp solutions (7 µM) in DMSO (black) in PBS (grey). Wavelengths corresponding to the maxima of absorption and emission bands are indicated for Hyp dissolved in DMSO.*

In this work, Hyp was often dissolved or pre-dissolved in DMSO. DMSO is a convenient solvent for the purposes of this work: it dissolves Hyp up to high concentrations (> mM); it is fully miscible with water; unlike other solvents, it does not experience a fast evaporation; and it is relatively well tolerated by some proteins and biosystems. The main drawback of DMSO is that it is a bad solvent for an accurate determination of the values of Φ_Δ, since it constitutes a $^1O_2$ quencher. An estimation of the Φ_Δ for Hyp dissolved in DMSO (air-equilibrated) has been obtained by comparison with several reference PSs, according to a previously described method (see 3.7). Since there is no well-established reference PS in DMSO, we hypothesized that the Φ_Δ values in water would hold in DMSO. This seems to be the case for two porphyrins, namely TMPyP and TPPS, which yielded a similar Φ_Δ value for Hyp in DMSO (Φ_Δ=0.28 ± 0.05 taking $\Phi_{\Delta ref}$ =0.74 for TMPyP and TPPS in aqueous solvents [4]). The Φ_Δ found is in good agreement with a previous value determined by laser-induced optoacoustic spectroscopy [5]. The value found using another common reference PS, namely Rose Bengal (RB), as reference was disregarded as unrealistically high (Φ_Δ=0.43 ± 0.05 taking $\Phi_{\Delta ref}$=0.75 for RB in aqueous solvents) since using this reference, it would be inferred that the Φ_Δ values of the porphyrins would be 1.15, which goes above the upper limit of 1. A summary of the photo-physical properties obtained for Hyp dissolved in DMSO is reported in Tab. 4-1.

4.1.2 ApoMb-Hyp: a stable nanostructure

A simple protein-based nanostructure was obtained through the binding of Hyp into the main hydrophobic cavity of apoMb. The nanostructure self-assembles in aqueous solution taking advantage of the hydrophobic interaction. The change in the photo-physical properties of Hyp, particularly fluorescence emission, constitutes a precise tool to monitor the occurring of the binding and the affinity of the two species in a PBS buffered solution. Indeed, when Hyp is placed in the aqueous solution in the presence of apoMb, it recovers a structured and well defined absorption spectrum and a fluorescence emission spectrum that closely resemble those of Hyp dissolved in polar organic solvents (Fig. 4-2 A). This indicates that a large fraction of Hyp molecules is not aggregated, rather it behaves as a monomeric species and is well solubilized by the interaction with apoMb, where the PS senses a local environment with characteristic of polarity similar to those experienced in EtOH or DMSO.

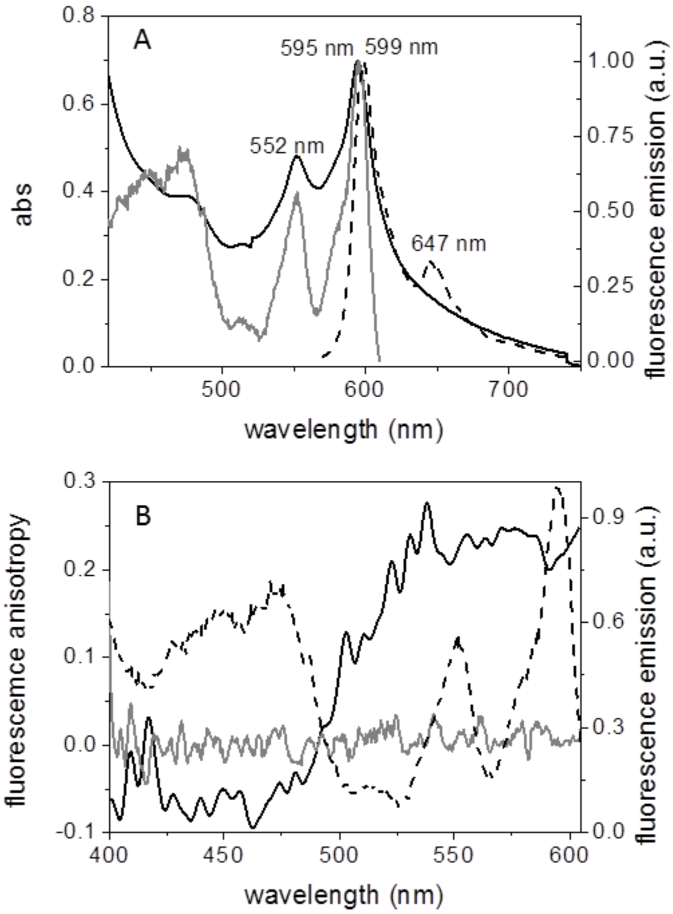

Fig. 4-2 A: Absorption (black solid), fluorescence emission (black dashed, λ_{ex} = 550 nm), fluorescence excitation (grey solid, λ_{em} = 620 nm) spectra of apoMb-Hyp in PBS solution. Wavelengths corresponding to the maxima of absorption and emission bands are indicated for apoMb-Hyp. B: Fluorescence excitation anisotropy spectra of apoMb-Hyp in PBS solution (black solid, λ_{em} = 620 nm) and of Hyp in DMSO (gray solid, λ_{em} = 620 nm). The fluorescence excitation

spectrum of apoMb-Hyp in PBS solution (black dotted, λ_{em} = 620 nm) is reported for reference. T = 25°C. Where present, apoMb is in excess with respect to Hyp (5:1).

An important proof for the existence of an interaction between Hyp and apoMb, leading to the formation of a stable nanostructure, is provided by steady-state fluorescence anisotropy. This entity is related to the rotational diffusion of the fluorophore during its fluorescence emission lifetime [6]. As can be observed in Fig. 4-2 B, Hyp dissolved in DMSO shows zero anisotropy as a consequence of the rapid rotation of the molecule in solution which removes the initial orientation of the excited states dipole moment. Conversely, in the presence of apoMb, the anisotropy is non-zero meaning that Hyp rotation is much slower and the molecule holds a preferential orientation within its lifetime of fluorescence emission. This is a consequence of the interaction of Hyp with the cavity of apoMb, that induces constraints limiting the rotational diffusion of the molecule within its emission lifetime. The fluorescence auto-correlation curves measured with the FCS equipment, gave an additional proof for the formation of a stable complex between Hyp and apoMb (Fig. 4-3). Concentrations were set to ~10 nM Hyp and ~30 μM apoMb, so that the large excess of protein ensures that the binding of Hyp to apoMb is preserved when single molecule conditions are achieved for the fluorophore. The signal is conveniently described by a model comprising one diffusing species also undergoing population of a dark state (triplet state). The retrieved diffusion coefficient is D = 120 $\mu m^2 s^{-1}$ that is attributed to Hyp bound to apoMb, since the value is close to the one obtained for proteins with similar molecular mass as apoMb.

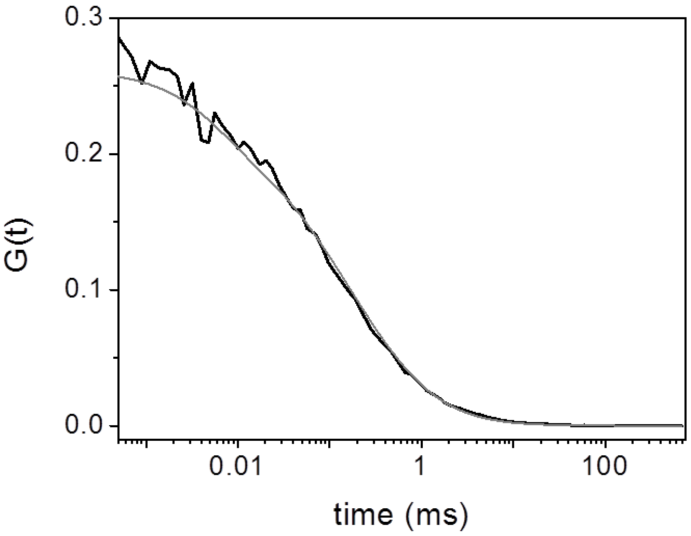

Fig. 4-3 *Auto-correlation curve measured for the apoMb-Hyp complex (black) and curve resulting from the best fitting with a model comprising one diffusive species and the formation of a dark state (grey).*

The value of the equilibrium constant for the formation of the apoMb-Hyp complex was obtained by monitoring the fluorescence emission of Hyp at increasing concentration of the protein in a PBS buffered solution. Since the emission arising from unbound aggregated Hyp is negligibly weak, the fluorescence is emitted only by the bound species so that the integrated fluorescence emission reflects the concentration of apoMb-Hyp at increasing protein concentration (Fig. 4-4). The value for binding equilibrium constants are retrieved according to the model outlined in Section 3.14 and correspond to $K_a = (2.4 \pm 0.5) \cdot 10^5\ M^{-1}$ and $K_d = (4.2 \pm 0.8)\ \mu M$.

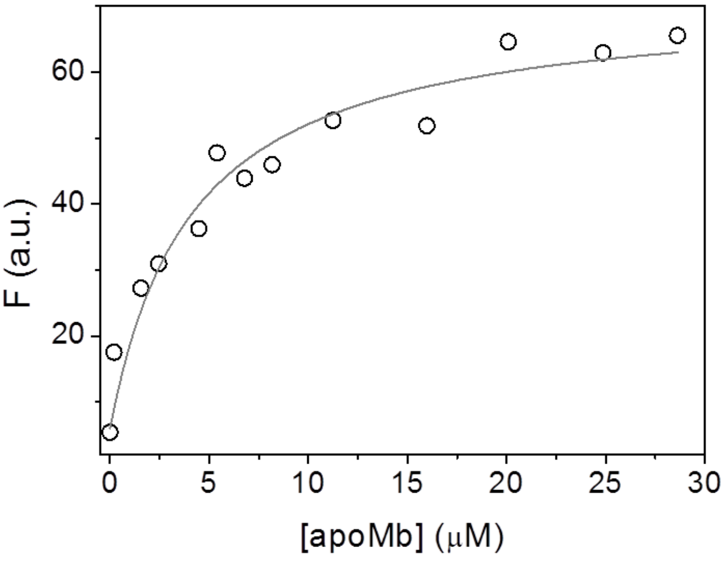

Fig. 4-4 *Integrated fluorescence emission (F) as a function of total protein concentration. The grey solid line is the result of a fit to the observed emission using a model derived from the binding equilibrium (see 3.14).*

Finally, docking simulation confirmed that the binding of Hyp occurs at the main hydrophobic cavity of apoMb, that accommodate the heme cofactor in the native holo-protein (Fig. 4-5). This is not surprising given the similarities in size, molecular symmetry and hydrophobicity of the two ligands. As expected from spectroscopic results, the interaction is mainly driven by hydrophobic effect and occurs with an estimated free energy of binding of -9.89 kcal mol^{-1}. [7]

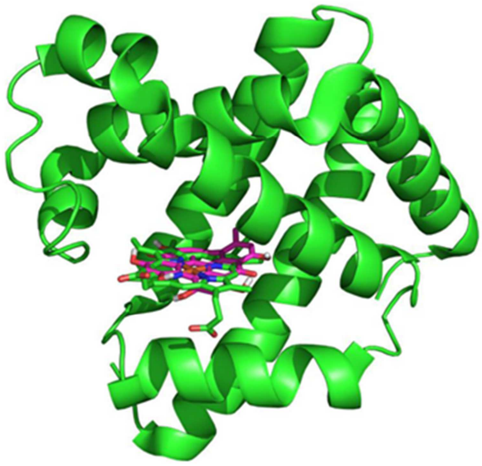

Fig. 4-5 *Crystal structure of horse Mb (PDB 1WLA, the protein is shown as green cartoon, the heme in green sticks) showing also the representative docking of Hyp (magenta sticks) into the apoMb structure, obtained using the Lamarckian algorithm. Adapted from* [7].

4.1.3 ApoMb-Hyp: a photo-functional theranostic system

The formation of a stable protein-based nanostructure apoMb-Hyp is a particularly relevant finding in the perspective of its application as a drug delivery system for the photo-physically active molecule Hyp.

4.1.3.1 Photosensitizing action

Since Hyp mainly finds application as photosensitizing agent, it is particularly important to assess that the molecule is able to reach the excited triplet state and sensitize $^1O_2$ to a significant extent, when it is bound in the cavity of apoMb. The presence and the lifetime of the transient triplet state of Hyp were determined with a laser flash photolysis (LFP) setup by monitoring directly the transient T-T absorption of this state at 515-520 nm, after ns laser excitation at 532 nm. Additional indirect evaluations of the triplet state lifetime of Hyp embedded in the protein were obtained from the time-resolved NIR phosphorescence signal of $^1O_2$ or were retrieved by the fitting of auto-correlation curves obtained with FCS. Values are summarized in Tab. 4-1 where it appears clear that the triplet state is formed in consequence of a photo-excitation of apoMb-Hyp, and it is characterized by a lifetime (τ_T) of ~10 μs, that is substantially longer than what is usually expected for PSs dissolved in air-equilibrated solutions [8 9]. Since the value of τ_T is essentially determined by the bi-molecular quenching induced by O_2, a reduced accessibility of O_2 to the cavity of apoMb (where Hyp binds), appears to be the more likely explanation for the longer τ_T observed for apoMb-

Hyp with respect to other PSs dissolved in aqueous solutions. The ability of apoMb-Hyp to photosensitize the production of $^1O_2$ was determined directly by the measurement of the time-resolved phosphorescence emitted by this species at 1270 nm. The measured signal shows the typical rise and decay trend that is well fitted with a bi-exponential model characterized by the two lifetimes τ_T and τ_Δ. The comparison of the signals obtained for an air-equilibrated and a O_2-saturated solution allowed assignment to the triplet state of the lifetime that reduces from (11.1 ± 0.4) μs to (5.0 ± 0.4) μs upon saturation with O_2. The lifetime that is not significantly affected by the change of O_2 concentration in solution is attributed to the $^1O_2$ species and correspond to τ_Δ = (2.5 ± 0.4) μs, that is consistent with the expected value of τ_Δ in water [8]. The determination of Φ_Δ for apoMb-Hyp in PBS buffer, that is of particular importance for potential applications, was obtained by comparison of the $^1O_2$ phosphorescence signal produced by the complex with the one of other PSs, namely RB and TMPyP, of known Φ_Δ that were used as reference. This procedure yielded a respectable value of (0.14 ± 0.03) for the air-equilibrated solution and (0.19 ± 0.03), slightly higher but still consistent, for the O_2-saturated solution, indicating that the shielding of Hyp from the solvent, due to the protein scaffold, does not preclude the formation of $^1O_2$. This characterization demonstrates the potential of the protein-based nanostructure apoMb-Hyp as water soluble and bio-compatible therapeutic agent for photosensitization-based applications.

	Φ_F	τ_F(ns)	τ_T(μs)	Φ_Δ	τ_Δ(μs)
Hyp DMSO	0.35±0.02 [10]	5.5±0.1 (100%) [1]	1.6±0.1* 1.5±0.1§ 1.9±0.1*	0.28±0.05§ 0.33 [5]	5.5±0.1§
apoMb-Hyp [7]	0.14±0.02	0.01±0.01 (7%) 4.0±0.1 (25%) 6.4±0.1 (68%)	11.6±0.1* 10.4±0.4§ 10±1#	0.14±0.03§	2.4±0.4§

Tab. 4-1 *Photo-physical Parameters determined for Hyp dissolved in DMSO and for apoMb-Hyp in PBS buffer. *: LFP; §: NIR phosphorescence, #: FCS.*

4.1.3.2 A fluorescent reporter for microscopy based on stimulated emission

The possibility of localizing a photosensitizing agent in a biosystem is an important requirement for modern applications and, in most cases, fluorescence emission is exploited for this purpose. Given the extremely limited distance of diffusion of $^1O_2$ in a cellular environment, roughly 150 nm from the site of photosensitization (see 1.2.3), an accurate localization of the photosensitizing agent at the cellular level is extremely important for studying the effect of the photo-oxidation, since it reveals where the damage will be first induced. Fluorescence microscopy is the easiest and more direct technique to image the distribution of a PS in a cell, but its resolution is limited by the diffraction of light to a few hundred of nanometers. This resolution is inadequate for an accurate localization in relation to sub-cellular components, particularly for bacterial cells whose size is close to ~1 μm. A subdiffraction resolution, attainable with techniques of so-called super-resolution microscopy, is thus preferable. These techniques require that the fluorescent probes possess additional properties than the simple emission of fluorescence, e.g. the presence of a photo-switching between two a dark and a bright state or the possibility to efficiently induce stimulated emission without an excessive bleaching [11]. In this work we explored the possibility of exploiting Hyp, bound to the protein-based carrier, for an additional purpose besides its established role as a photosensitizing agent, and use it as a fluorescent probe for super-resolution Stimulated Emission Depletion (STED) microscopy. This technique is essentially based on the possibility of inducing a spatially-confined depletion of the fluorophore's excited state (and thus of the fluorescence emission) by inducing a stimulated emission immediately after the photo-excitation. Hyp is a good candidate as fluorescent reporter for STED. Indeed, its excited singlet state is sufficiently long-lived (~5 ns) for inducing the stimulated emission, and some works reported the observation of a stimulated emission for this molecule [12], that is potentially induced by red light. However, one of the crucial conditions for the achievement of super-resolution with STED microscopy is that the fluorophore does not exhibit excited state absorption bands in the spectral region of the depletion photon inducing the stimulated emission. Therefore, ultra-fast transient absorption experiments, with femtosecond laser excitation, were performed to assess the possibility of inducing stimulated emission from Hyp excited state. Experiments were performed on both Hyp dissolved in DMSO and the apoMb-Hyp nanostructure dissolved in PBS buffer.

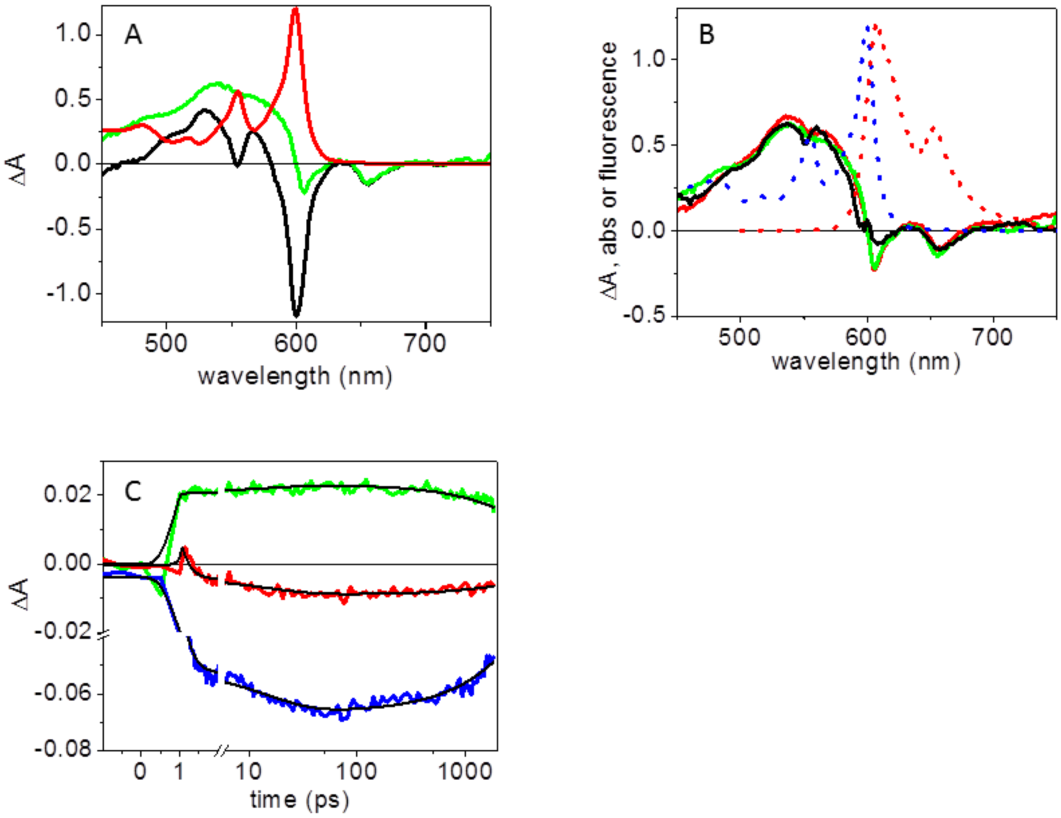

Fig. 4-6 *A: The steady state absorption spectrum (red solid line) is used to remove the ground state bleaching from the raw transient absorption spectra (black line). This allows to retrieve corrected transient absorption spectra (green line). The example corresponds to the transient spectrum at 100 ps delay for 120 μM Hyp in DMSO after a femtosecond excitation at 400 nm. B: Corrected transient absorption spectra for Hyp (120 μM) in DMSO at 3 ps (black), 10 ps (red), and 100 ps (green). The dotted lines correspond to steady state absorption (blue) and fluorescence emission (red). C: Absorption changes after 400 nm excitation of Hyp (120 μ M) in DMSO at selected wavelengths, reflecting excited state absorption (521 nm, green), ground state bleaching (592 nm, blue), and stimulated emission (647 nm, red). Black solid lines are the result of a global analysis performed on the single traces using a sum of three exponential decay functions.*

Fig. 4-6 A reports the results of transient absorption spectroscopy for Hyp dissolved in DMSO, collected at 100 ps delay from the photo-excitation. The ground state spectrum is reported in red, while the transient absorption spectrum is reported in black. It is possible to appreciate the prominent ground state bleaching appearing as a negative band at ~600 nm in the transient spectrum, i.e. where the ground state has its maximum absorption. Subtracting the ground state absorption from the transient absorption, a corrected differential spectrum is obtained (reported in green), where the contribution of the ground state bleaching is removed and thus the transient absorption from the excited states of the molecule can be observed. Other transient absorption spectra corrected from ground state bleaching are reported in Fig. 4-6 B (solid) corresponding to 3 ps (black), 10 ps (red) and 100 ps (green) after the photo-excitation. The features of these spectra are similar, showing a marked excited state absorption in the 500-600 nm region, with two bands at ~531 nm and ~567 nm. The negative bands (increased transmitted light) observed at 606 nm and 656 nm are attributed to stimulated emission induced by the probe beam. Indeed, the position of these bands nicely correspond to those observed in the steady state fluorescence emission spectrum at 607 nm and 654 nm, that is showed in dotted red. The different ratio of intensity of these two bands in the steady state and corrected transient absorption spectra is likely due to a self-absorption at ~600 nm occurring in the transient spectra, due to the high concentration of Hyp. It is important to point out that there is no evidence for significant Hyp excited state absorption above 600 nm, so that an excitation in this spectral region appears suitable for inducing the stimulated emission without the occurring of unwanted transitions. A kinetic analysis is displayed in Fig. 4-6 C, where the time-resolved transient absorption is reported at three selected wavelengths corresponding to the excited state absorption (521 nm, green), the ground state bleaching (592 nm, blue) and the stimulated emission (647 nm, red). Because of the self-absorption effects occurring at ~600 nm, we have chosen to monitor the stimulated emission of the second band at 647 nm. A global analysis of these signals affords a bi-phasic kinetic with two lifetimes corresponding to ~10 ps and ~6 ns. The faster transient is attributed to an intra-molecular proton transfer process occurring from the excited state [12] [10] [13], whereas the slower transient corresponds to the singlet excited state decay, and is consistent with the measured fluorescence lifetime.

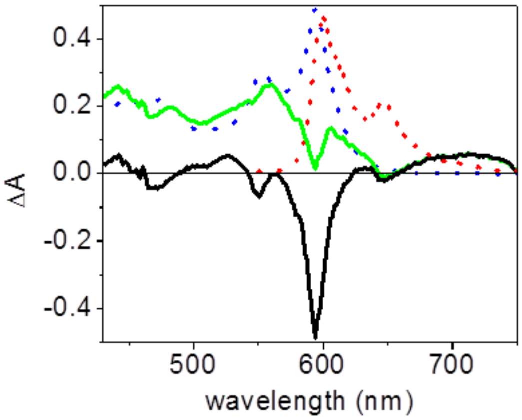

Fig. 4-7 The steady state absorption spectrum (blue dotted line) is used to remove from the raw transient absorption spectra (black line) the ground state bleaching. This allows to retrieve corrected transient absorption spectra (green line). The sample curves corresponds to a 1000 ps delay after a femtosecond excitation at 400 nm. The dotted red line corresponds to steady state fluorescence emission. Spectra are collected on a sample of apoMb-Hyp (120 μM Hyp, 530 μM apoMb) in PBS buffer.

Similar results were obtained for the sample of apoMb-Hyp in PBS buffer, although with a lower signal-to-noise ratio due to the lower concentration of Hyp. The presence of a stimulated emission at 594 nm and 650 nm can be recognized in the transient absorption spectra of Fig. 4-7. While the excited state absorption (green curve) appears broadened and weaker than for Hyp in DMSO, extending to the near infra-red region. The global analysis of the transient absorption kinetics, shows that apoMb-Hyp preserves the same features evidenced for Hyp in DMSO, namely bi-phasic kinetics characterized with two lifetimes of ~7 ps and ~3 ns. This suggests that, unlike other cases [14], the presence of the protein matrix, does not appear to interfere with the faster transient, relative to the intra-molecular proton transfer process.

Since transient absorption spectroscopy evidenced a good potential for Hyp to be employed as a fluorescent probe for STED microscopy, the possibility of inducing a depletion of the Hyp excited state by stimulated emission was tested directly on the STED microscope. The resulting depletion curves are shown in Fig. 4-8 for Hyp in DMSO (blue), apoMb-Hyp in PBS buffer (purple), and Hyp embedded in DLPC liposomes (orange), which constitutes a model system for the cellular membranes.

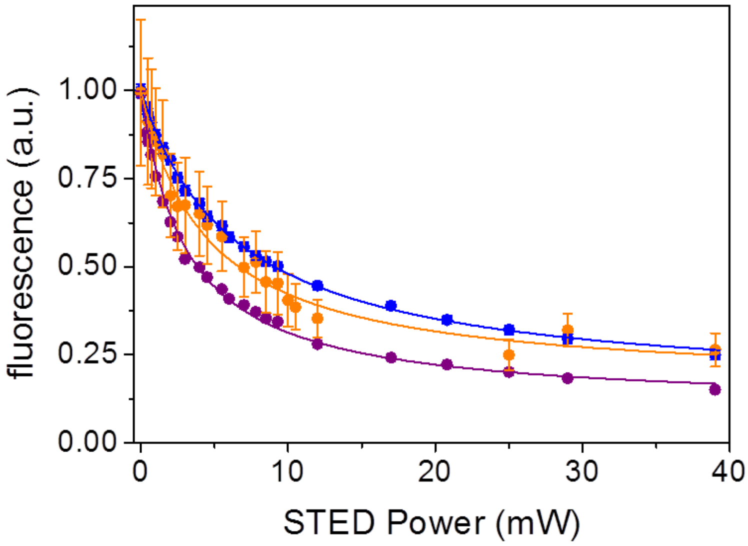

Fig. 4-8 *Fluorescence depletion curves for Hyp in DMSO (10μM, purple circles), apoMb-Hyp in PBS (10 μM Hyp, 30 μM apoMb, blue circles), and Hyp in the presence of DLPC liposomes (10 μM Hyp, 390 μM DLPC, orange circles) collected under excitation at 570 nm and detection at 605-670 nm. The STED beam was at 715 nm. Solid lines are the best fit to depletion functions (see 3.11).*

In these measurements, Hyp is excited at 566 nm with a pulsed excitation, and the emission is collected between 605 and 670 nm at increasing power of the STED beam at 715 nm that induces the stimulated emission in resonance with a vibrionic transition of the emission spectrum. For all samples, the emission of fluorescence is significantly reduced (more than 50% of the initial value) for the higher powers of the STED beam, that is enough to overcome the diffraction-limited resolution. However, the saturation power is lower for Hyp in DMSO than for apoMb-Hyp or Hyp embedded in liposomes (Tab. 4-2), which showed a similar trend. In all cases, it is not possible to reach a full depletion of the Hyp excited state and an additive constant must be introduced to describe the depletion curves, which may be taken as indication for a fraction of non-saturable fluorescence emission (Tab. 4-2). The presence of a weak excited state absorption in the spectral region of the STED beam for apoMb-Hyp, that was showed by transient absorption experiments (Fig. 4-7), is probably one of the reasons for the larger non-saturable fraction of fluorophores and the higher saturation power observed for apoMb-Hyp with respect to Hyp dissolved in DMSO.

	Is (mW)	**α**
Hyp in DMSO	3.1 ± 0.1	0.10 ± 0.01
apoMb-Hyp	6.5 ± 0.1	0.14 ± 0.01
Hyp liposomes	4.5 ± 0.5	0.16 ± 0.02

Tab. 4-2 *Parameters retrieved from the fitting with model for fluorescence depletion curves . Is: intensity of the STED beam at which the rate of the stimulated emission equals the spontaneous decay; α: additive constant proportional to the level of non saturable fluorescence (see 3.11).*

4.1.4 ApoMb-Hyp and bacterial cells in suspension

4.1.4.1 Imaging Hyp in bacteria with subdiffraction resolution

The applicability of the apoMb-Hyp nanostructure for super-resolution fluorescence imaging was tested on the Gram-positive bacteria *Bacillus subtilis* and *Staphylococcus aureus*, and on Gram-negative bacteria *Escherichia coli*, using a STED microscope. In Fig. 4-9 a comparison is made between images of *B. subtilis* incubated with apoMb-Hyp obtained with confocal (Fig. 4-9 A) and STED (Fig. 4-9 B) microscopy.

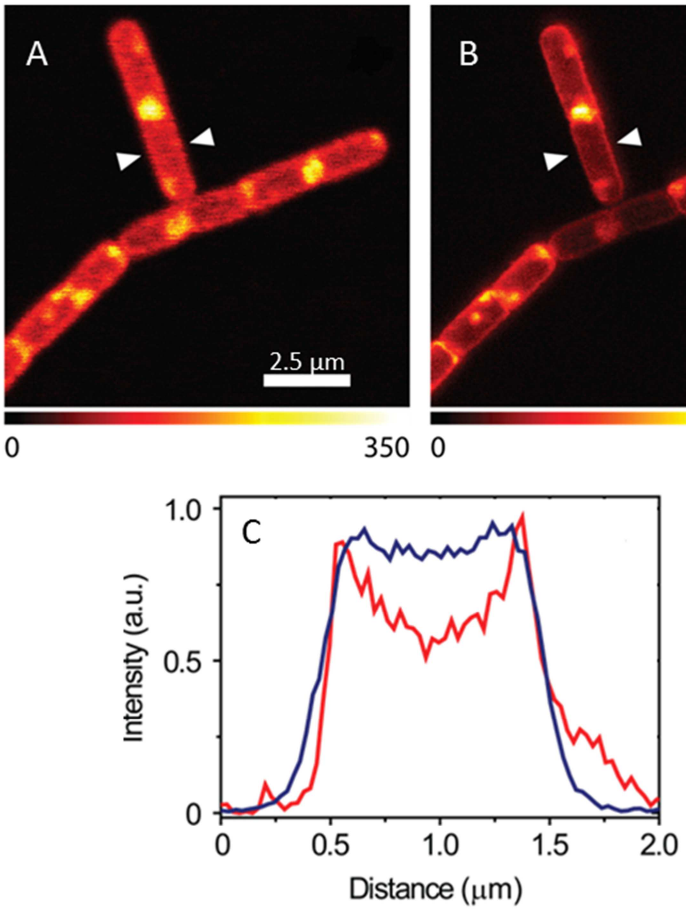

***Fig. 4-9** Comparison between B. subtilis images collected with confocal microscopy (A) and with STED nanoscopy (STED power 30 mW, pixel dwell time 0.1 ms) (B) after incubation with apoMb-Hyp. The blue and the red intensity profiles (C) were measured along the segment connecting the arrows in A and B respectively. Images are collected under excitation at 566 nm and detection at 605-670 nm, with STED beam at 715 nm.*

Both images show that the cells become fluorescent after the incubation period and thus that the protein-based carrier (apoMb) delivered Hyp to the cells, preventing its aggregation. However, the image undergoes a remarkable improvement in resolution when the STED beam is turned on (Fig. 4-9 B), comparable with the one observed for different dyes on the same bacterial cells [15], that allows to determine with higher precision the distribution of the PS at cellular level. The improved quality of the images can be better appreciated by inspection of the fluorescence emission profile along the cross section of a cell, as indicated in Fig. 4-9 C. This reveals the accumulation of Hyp on an outer component of the cell, having a width in the order of 90 nm, that can be identified with the cell wall of the Gram-positive bacteria, formed by an outer peptidoglycan layer and an inner cell membrane (see 1.3.1).

The improved resolution of the STED reveals details that cannot be appreciated in the confocal images. A good example is reported in Fig. 4-10 for small and spherical *S. aureus* cells incubated with apoMb-Hyp. The STED image (Fig. 4-10 B) shows that some cells are undergoing division, with a septum that separates two hemispheres in the original cell, clearly visible from the emission profile in Fig. 4-10 C, which cannot be recognized in the blurred confocal images (Fig. 4-10 B).

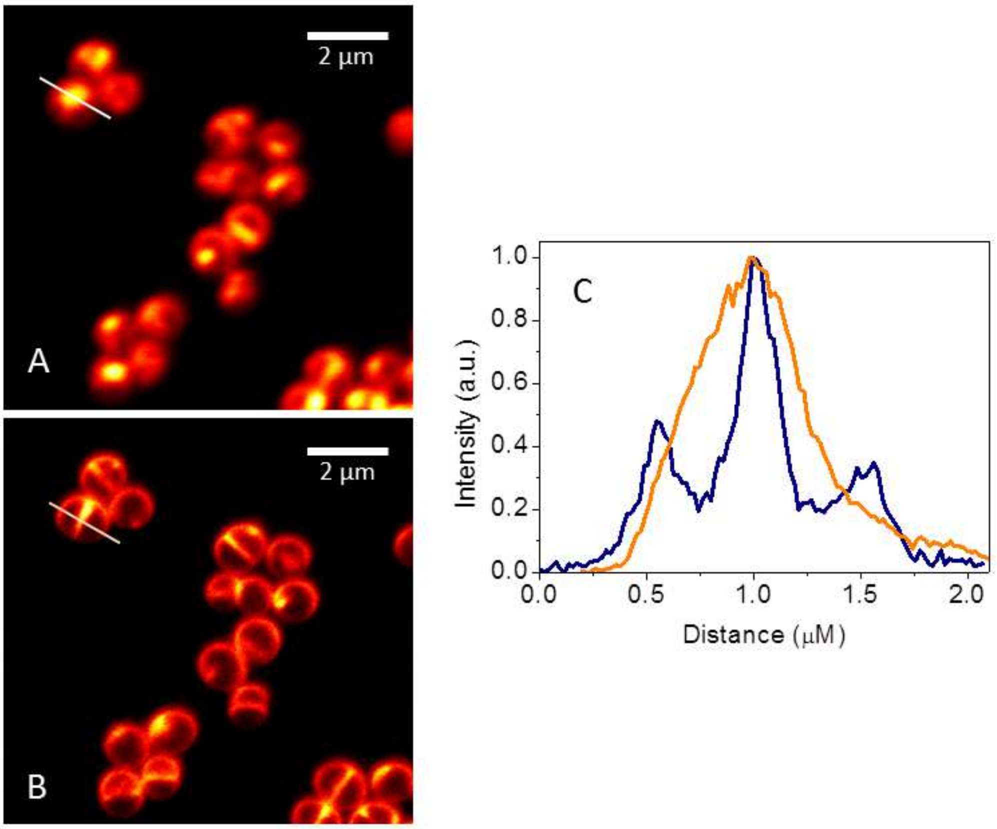

Fig. 4-10 *Comparison between S. aureus images collected with confocal microscopy (A) and with STED nanoscopy (STED power 23.6 mW, pixel dwell time 0.1 ms) (B) after incubation with apoMb-Hyp. The orange and the blue intensity profiles (C) were measured along the white segment in A and B respectively. Images are collected under excitation at 566 nm and detection at 605-670 nm, with STED beam at 715 nm.*

A similar distribution is of Hyp on the bacterial cell wall is observed after the incubation of apoMb-Hyp with the Gram-positive bacteria *S. aureus* (Fig. 4-11 E and F), and with the Gram-negative *E. coli* (Fig. 4-11 C and D) and *B. subtilis* (Fig. 4-11 A and B), whose structure of the bacterial cell wall is more complex and less permeable (see 1.3.1). The current STED resolution indisputably allows to identify a preferential accumulation of Hyp delivered with apoMb on bacterial cell wall, which does not result so clear at the diffraction-limited resolution obtained with the confocal microscope. However, the improved resolution is not sufficient to determine the finer distribution of the PS on the components that constitute the cell wall, like the peptidoglycan layer or the membranes.

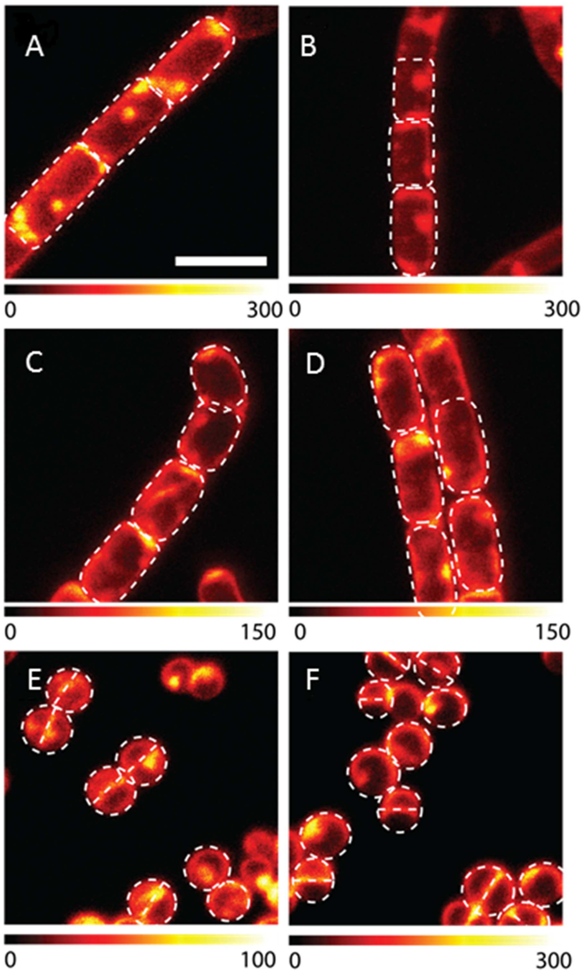

Fig. 4-11 *Selected STED images of B. subtilis (A,B), E. coli (C,D) and S. aureus cells (E,F) incubated with apoMb-Hyp (10 µM Hyp, 30 µM apoMb) collected under excitation at 566 nm and detection at 605-670 nm, with STED beam at 715 nm (power 30 mW and dwell time 0.1 ms (for A–D) and 0.05 ms (for E,F). White dashed lines are intended as visual aid to guide the eye along the bacterial shape.*

Additionally, some specific accumulation points for Hyp, corresponding to more intense fluorescent regions, can be identified for all cell types. The fairly similar topology of the accumulation points (Fig. 4-11) suggests a specific interaction with yet to be identified bacterial components, possibly located inside the areas of MreB-dependent wall growth [16], or cytoskeleton components [17]. Interestingly, the images obtained with STED allow to appreciate details of the process of cells division, and the areas of the Hyp accumulation appear to be connected to these processes of growth and division. The shape of dividing bacteria retrieved by STED imaging is consistent with the established division mechanisms for the three types of bacteria. *B. subtilis* divides by septation without constriction, resulting in squared-off cell poles [16] (Fig. 4-11 A and B). Conversely, the Gram-negative *E. coli* needs a coordinated constriction of both outer and inner membranes and a septum formation, thus leading to round poles in the dividing cells [18] (Fig. 4-11 C and D).

Interestingly, in newborne rod shaped cells like *E.coli* the peptidoglycan synthesis occurs along the sidewall leading to a elongation of the cell to twice its original length. While at the time of the cell division, the synthesis apparatus switch from side-wall peptidoglycan synthesis to division septum synthesis [19]. This switching between these two growth modalities appears consistent with the Hyp accumulation points at the poles or in the central body of the cells. Unlike *B. subtilis* and *E. coli*, *S. aureus* has a spherical shape. Its growth occurs through a FtsZ dependent mechanism and septation separate two hemispheres during the cell division [16]. Areas of more intense fluorescence are observed at the septum region which appears thicker than the cell wall (Fig. 4-11 E and F), in agreement with observations based on electron microscopy [20].

Co-localization experiments where specific cell components are labelled with a suitable fluorescent probe may result helpful for a precise determination of the distribution of the PS on the components of the bacterial wall and to precisely identify the nature of the observed accumulation points.

Interestingly, the images collected for bacteria after the incubation with a small volume of concentrated solution of Hyp in DMSO, show distributions of the fluorophore that are indistinguishable from those obtained for Hyp delivered with apoMb.

4.1.4.2 Bacteria photo-inactivation

In spite of the very similar distribution of Hyp on the three bacterial types, the effect induced by irradiation of the Hyp-loaded cells are remarkably different according to the bacterial cells considered. The results of the photo-inactivation experiments showing the bacterial cell viability after the photo-treatment are summarized in Fig. 4-12 and point out a major difference of efficacy between Gram-positive and Gram-negative bacteria. The lower green light dose used (18 J cm^{-2}) is enough to decrease the number of colony forming units by 5 log units for *S. aureus*. Remarkably, the dark toxicity appears lower for Hyp delivered with apoMb (blue square) than for free Hyp dispensed as a concentrated solution in DMSO (red square). Conversely, no sizeable effects are observed on the Gram-negative *E. coli* (red and blue circles). The case of the Gram-positive *B. subtilis* appears intermediate, with an effect of light exposure inducing a ~2 orders of magnitude decrease in the number of bacterial colony forming units for both Hyp delivered with apoMb-Hyp and free Hyp (blue and red triangles respectively). The presence of a clearly detectable $^1O_2$ phosphorescence for apoMb-Hyp incubated with bacteria (data not shown) demonstrated that the photo-sensitizing ability of the nanostructure is not precluded in the presence of cells. Indeed, the different response of Gram-positive and Gram-negative bacteria to photosensitization-based treatment was reported in literature for other PS molecules and has been correlated to the different structure of bacterial cell wall (see 1.3.1), that is less permeable in the case of Gram-negative bacteria [21]. This is consistent with our STED images that revealed a preferential distribution of Hyp on the bacterial cell wall. Further studies will be necessary to elucidate the considerably different response of the two Gram-negative bacteria *S. aureus* and *B. subtilis* to the photo-treatment. A possible explanation can be related to the ability of *B. subtilis* to generate bacterial spores under certain stress conditions [22], that may occur during the irradiation. This was qualitatively indicated by malachite green essays performed on cells incubated with apoMb-Hyp and grown under illumination and by a similarity of the structural features of the cells with the one reported for cells where spore formation is induced [23]. However a detailed justification of this observed different response would require a more accurate investigation, that falls outside the scope of this work.

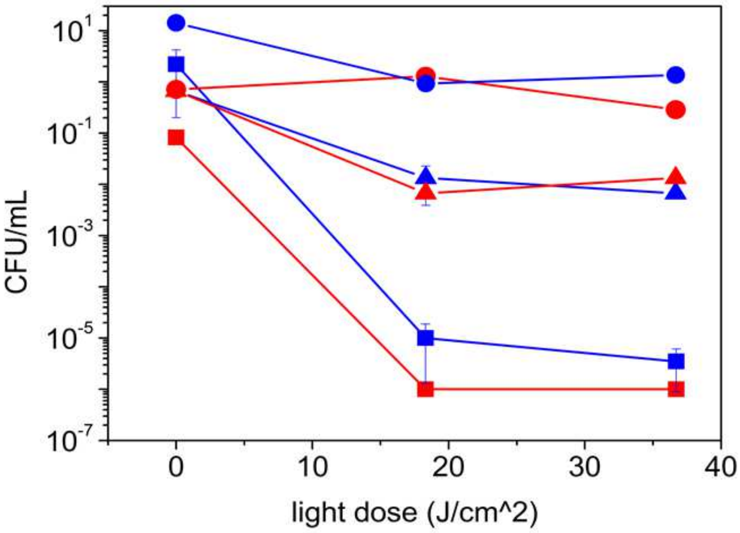

Fig. 4-12 *Light dose effects on S. aureus (squares), B. subtilis (triangles), and E. coli (circles) photo-inactivation after incubation with Hyp (red) and apoMb-Hyp (blue). [Hyp] = 10 µM, [apoMb] = 30 µM, where present.*

4.1.5 Apo-Hyp in the presence of liposomes: a model system

DLPC liposomes were used as simplified model for investigating the behavior of apoMb-Hyp in the presence of a phospholipidic bilayer. The data collected in the presence of liposomes constitute a useful reference for the study of the nanostructure on eukaryotic cells, where the phospholipidic bilayer of the plasma membrane is one of the major structural components. Hyp readily dissolves in liposomes where it shows similar properties as in organic solvents (Fig. 4-13 A). As can be observed in Tab. 4-3, we determined a value of Φ_Δ corresponding to (0.29 ± 0.05) for Hyp embedded in DLPC liposomes that is fairly consistent with a previously reported one [24], and similar to the one determined for Hyp in DMSO. A problem concerning the use of liposomes as solubilizing agent for Hyp is constituted by the fact that the photo-physical properties are dependent on the concentration of Hyp. Indeed, Hyp tends to aggregate into the phospholipidic bilayer at increasing concentration [25]. We thus performed the experiments under fixed experimental conditions, in order to have comparable results. A comparison of the values obtained for the τ_T of Hyp, indicates a considerably faster triplet state decay for Hyp embedded in liposomes (~ 2 μs), when compared with Hyp bound to apoMb (~10 μs), where the relatively longer lifetime was attributed to a partial shielding from the solvent due to the protein matrix (see above). When the complex apoMb-Hyp is placed in a solution with liposomes, the observed τ_T does not undergo relevant variations and yields a long value of ~10 μs, supporting the idea that the main fraction of Hyp molecules is still bound to the protein's cavity where is partially protected from the solvent.

	Φ_F	τ_F (ns)	τ_T (μs)	Φ_Δ	τ_Δ (μs)
Hyp DMSO	0.35±0.02	5.5±0.1 (100%)	1.6±0.1* 1.5±0.1§	0.28§ 0.33	5.5±0.1§
apoMb-Hyp	0.14±0.02	0.01±0.01 (7%) 4.0±0.1 (25%) 6.4±0.1 (68%)	11.6±0.1* 10.4±0.4§ 10±1$^{\#}$	0.14±0.03§	2.4±0.4§
apoMb-Hyp liposomes	-	1.4 ns (17%) 7.1 ns (83%)	10±1$^{\#}$	-	-
Hyp liposomes	0.19±0.01	2.3 ±0.1 (18%) 6.8±0.1 (82%)	2.5* 1.5$^{\#}$	0.35±0.02 [24] 0.29±0.05§	2.95±0.04§

Tab. 4-3 *Photo-physical parameters determined for Hyp dissolved in DMSO, apoMb-Hyp in PBS buffer and in the presence of liposomes, and for Hyp embedded in liposomes. *: LFP;* §*: NIR phosphorescence,* $^{\#}$*: FCS.*

As previously reported, when Hyp is bound to apoMb, its fluorescence anisotropy becomes substantial due to loss of rotational degrees of freedom (Fig. 4-2 B). The measured anisotropy excitation spectrum resembles closely that reported for Hyp glasses at 77 K [26]. A similar behavior is observed when Hyp embedded in liposomes (Fig. 4-13 B), with an anisotropy value which is a bit smaller than the one observed for apoMb-Hyp and with more structured, although noisy, bands. When the anisotropy excitation spectrum is measured for apoMb-Hyp in the presence of liposomes (Fig. 4-13 D), its shape appears different from that reported in Fig. 4-13 B, with values which are intermediate between the case of apoMb-Hyp and Hyp embedded in liposomes. This suggest that the interaction between Hyp and apoMb is affected by the presence of liposomes, but Hyp is probably still mostly bound to apoMb.

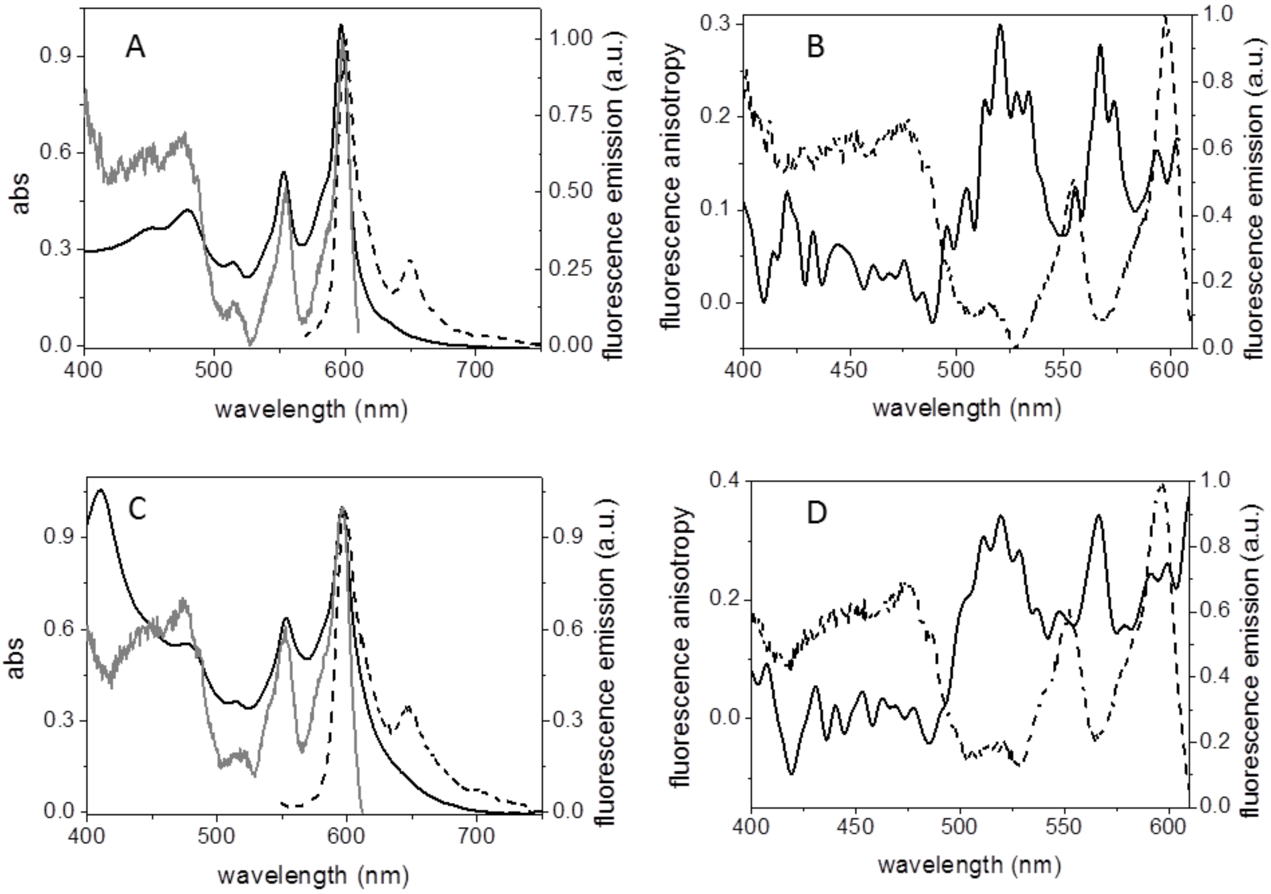

Fig. 4-13 *A: Absorption (solid black), fluorescence emission (dotted black,* λ_{ex} *= 550 nm), fluorescence excitation (solid grey,* λ_{ex} *= 620 nm) spectra of Hyp-liposomes in PBS solution. B: Fluorescence excitation anisotropy (solid black,* λ_{em} *= 620 nm) and fluorescence excitation (dotted black) spectra of Hyp-liposomes in PBS solution. C: Absorption (solid black), fluorescence emission (dotted black,* λ_{ex} *= 550 nm), fluorescence excitation (solid grey,* λ_{ex} *= 620 nm) spectra of apoMb-Hyp with liposomes in PBS solution. D: Fluorescence excitation anisotropy (solid black,* λ_{em} *= 620 nm) and fluorescence excitation (dotted black) spectra of apoMb-Hyp with liposomes in PBS solution. T=25°C.*

A comparison of the auto-correlation curves obtained with FCS is offered in Fig. 4-14 for three different solutions: apoMb-Hyp in PBS buffer (blue), Hyp embedded in DLPC liposomes (purple) and for apoMb-Hyp in presence of the liposomes (dark green). As previously mentioned, the fitting of the curve relative to apoMb-Hyp in buffer yields values that are consistent with the properties expected for this complex: a diffusion coefficient D = 120 $\mu m^2\ s^{-1}$ for the diffusing species, that is responsible for the decay of fluorescence auto-correlation on longer time-scale (between 0.01 and 100 ms); and a decrease of the auto-correlation occurring in the 1-10 μs range, owed to the formation of a dark state that is attributable to the triplet, from which a τ_T of (10 ± 1) μs is retrieved, consistently with the one directly determined by LFP (Tab. 4-3). The fluorescence decay of this sample occurs with lifetimes τ_1 = 1.6 ns (30%) and τ_2 = 6.1 ns (70%), a bit shorter than the data retrieved for a bulk sample (Tab. 4-3). For Hyp embedded in liposomes, the auto-correlation function is characterized by a considerably slower diffusion phase, which is approximated by a diffusion coefficient $D \approx 10\ \mu m^2\ s^{-1}$. Fitting is not perfect presumably due to some polydispersity of the liposomes. Triplet state formation is evident from the curve in the short microseconds, although with a much shorter lifetime ($\tau_T \approx 1.5\ \mu s$) than for protein bound Hyp, consistently with the values retrieved with LFP measurements. When liposomes are added to a apoMb-Hyp solution, the resulting auto-correlation curve appears only slightly different from the case of Hyp embedded in liposomes (Fig. 4-14). The diffusing species has a diffusion constant $D \approx 10\ \mu m^2\ s^{-1}$. A triplet decay is also evident, with lifetime $\tau_T \approx 10\ \mu s$. This suggests that the triplet state is much more protected from the environment than when Hyp is simply embedded in the liposome, and offers an argument in favor of preservation of the complex between Hyp and apoMb which may stick to liposomes as a whole. The fluorescence decay of this sample occurs with lifetimes $\tau_1 = 1.4$ ns (17%) and $\tau_2 = 7.1$ ns (83%).

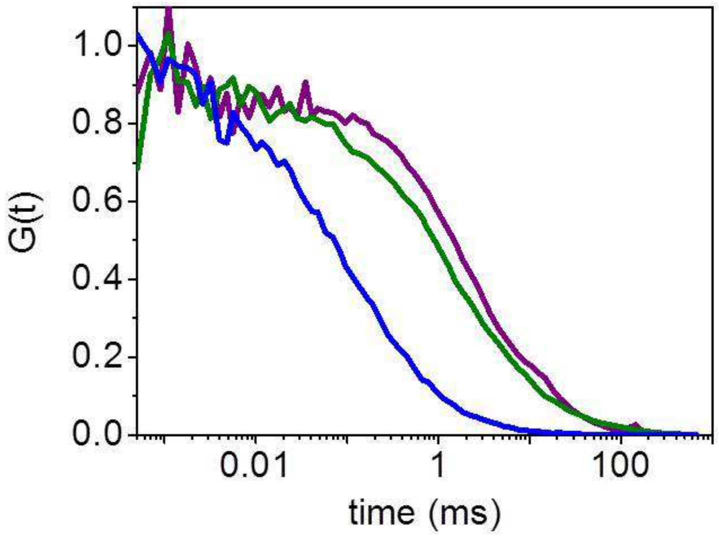

Fig. 4-14 *Comparison between auto-correlation curves collected for the apoMb-Hyp complex (blue), Hyp embedded in DLPC liposomes (purple), and for apoMb-Hyp placed ina solution containing DLPC liposomes (green).*

Based on the fluorescence decay, it is not possible to clearly establish the partition of Hyp between the phospholipidic environment of the liposomes and the protein cavity, given the very similar lifetimes for apoMb-Hyp and Hyp bound to liposomes. While the analysis of Hyp τ_F (Tab. 4-3) is extremely uncertain, some arguments based on the comparison of fluorescence anisotropy spectra, fluorescence auto-correlation curves and measured values of the τ_T of Hyp suggest that most Hyp molecules remain bound to the protein's structure. Thus the apoMb-Hyp complex would stick to the

DLPC liposomes as a whole. A direct assessment of the Hyp distribution between protein and phospholipidic phase would be possible by co-localization experiments simultaneously showing the position of Hyp and apoMb. However this is not a trivial issue given the difficulty to label apoMb with a suitable fluorescent reporter, e.g. through the realization of a chimeric protein of apoMb fused to a GFP.

4.1.6 Apo-Hyp and tumor cells in suspension

The photosensitizing agent apoMb-Hyp was studied also for the photo-induced inactivation of eukaryotic tumor cells in suspension, of the cell lines HeLa and PC3. The possibility of attaining STED images with subdiffraction resolution, exploiting Hyp as fluorescent reporter, allows to precisely determine the distribution of the PS on the cell components and correlate this parameter to the efficiency of the photo-treatment. In particular, it was possible to directly monitor the uptake process and the effect of photo-damage on the cells during time.

4.1.6.1 Imaging Hyp on tumor cells with subdiffraction resolution

Sharp images were obtained for both Hyp delivered with a apoMb or with a concentrated DMSO solution to the cells. The STED images collected for apoMb-Hyp in the presence of cells few minutes after the administration of the photosensitizing agent show a preferential accumulation of the PS on the cell membrane of both HeLa and PC3. Far less fluorescence appears in the cytoplasm and no fluorescence can be detected in the nucleus (Fig. 4-15). It is likely that the plasma membrane of the cells showed is already photo-damaged by the intense irradiation of the STED microscope, particularly for PC3 cells (Fig. 4-15 B), that are incubated with a higher amount of PS. Indeed the profile of the fluorescence emission from the membranes are quite irregular and some vesicles are starting to appear from the membrane. The emission of fluorescence from the cytoplasmic region in the cells is possibly due (at least partially) to the increased permeability of the membrane that starts to suffer from the damage induced by the photosensitization. Despite interesting possibility to collect imaging of the PS distribution in cells with subdiffraction resolution, the high power of the STED beam unavoidably appears to perturb the system under study (under the condition used), inducing a significant photo-damage from the very first time of acquisition of the images. In order to get a more reliable idea of the spatial and temporal distribution of the PS in the presence of these tumor cells, the system has been studied with a STED and with a spinning disk microscope.

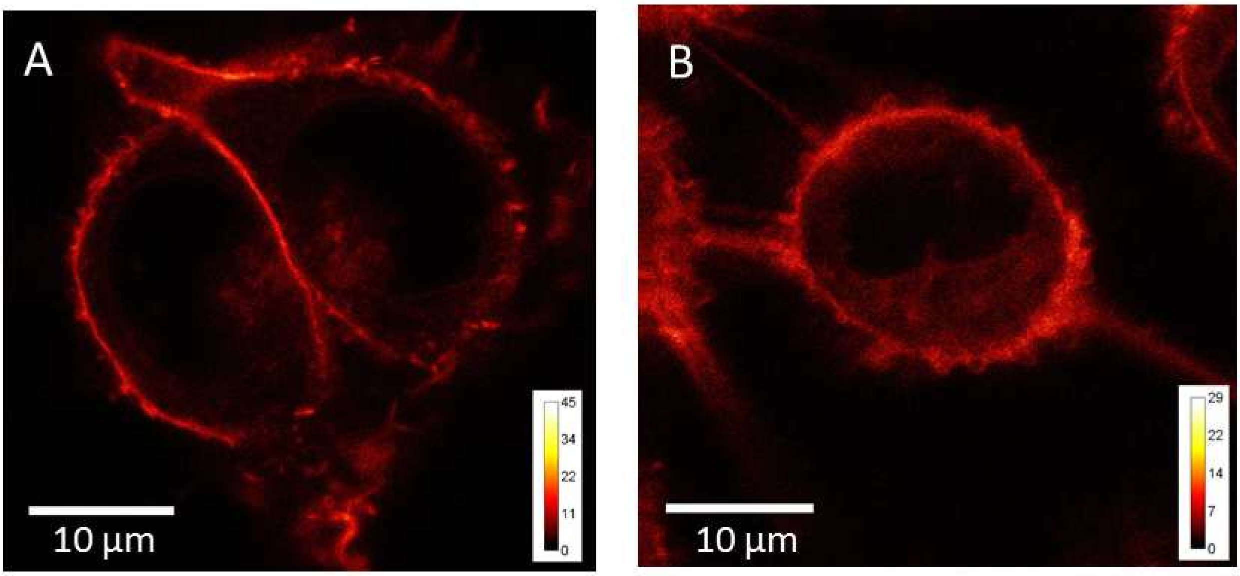

Fig. 4-15 *STED images of HeLa (A) and PC3 (B) cells collected just after administration of apoMb-Hyp. Concentrations: [Hyp] = 500 nM, [apoMb] = 1.5 µM for HeLa cells; [Hyp] = 1000 nM, [apoMb] = 3 µM for PC3. STED images were collected under excitation at 566 nm and detection at 605-670 nm with the STED beam at 715 nm.*

While STED microscopy allows to obtain sharp images with high spatial resolution but with an high impact on the integrity of the sample, the spinning disk is less invasive and allows to obtain information on the variation of the PS distribution in time, particularly in the first minutes after the administration to the cells, where the effects of the photo-damage are limited.

4.1.6.2 Protein-based carrier affects the initial distribution of the PS

4.1.6.2.1 HeLa

A spinning disk microscope has been used to image the initial distribution of the PS on the cells, and the process of cellular uptake. Despite the spatial resolution of the spinning disk images is diffraction-limited, this instrument allows to keep the cells under controlled conditions and to avoid the exposure to the extremely high power density necessary for the STED microscope. The spinning disk microscope is equipped with an incubation chamber that is used to keep the cells under optimal conditions of temperature, humidity and CO_2 pressure during the experiment. After the administration of apoMb-Hyp or Hyp pre-dissolved in DMSO, images are collected every 2 min, allowing a careful monitoring of the PS distribution in time. The incubation chamber ensures that good conditions for cell viability are maintained, so that the observed cell damaging only occurs as a consequence of the photosensitization, induced by the excitation light of the microscope. The spinning disk images are collected between 0 and 40 min from the administration of the photosensitizing agent. Only the images acquired within the first 10 minutes are reported since the cells appear heavily damaged on longer observation times. A careful inspection of these images reveals some remarkable differences in the cellular uptake of the PS, depending on whether Hyp (500 nM) is delivered with apoMb (Fig. 4-16 A-F) or is added as a concentrated solution in DMSO (Fig. 4-16 G-N).

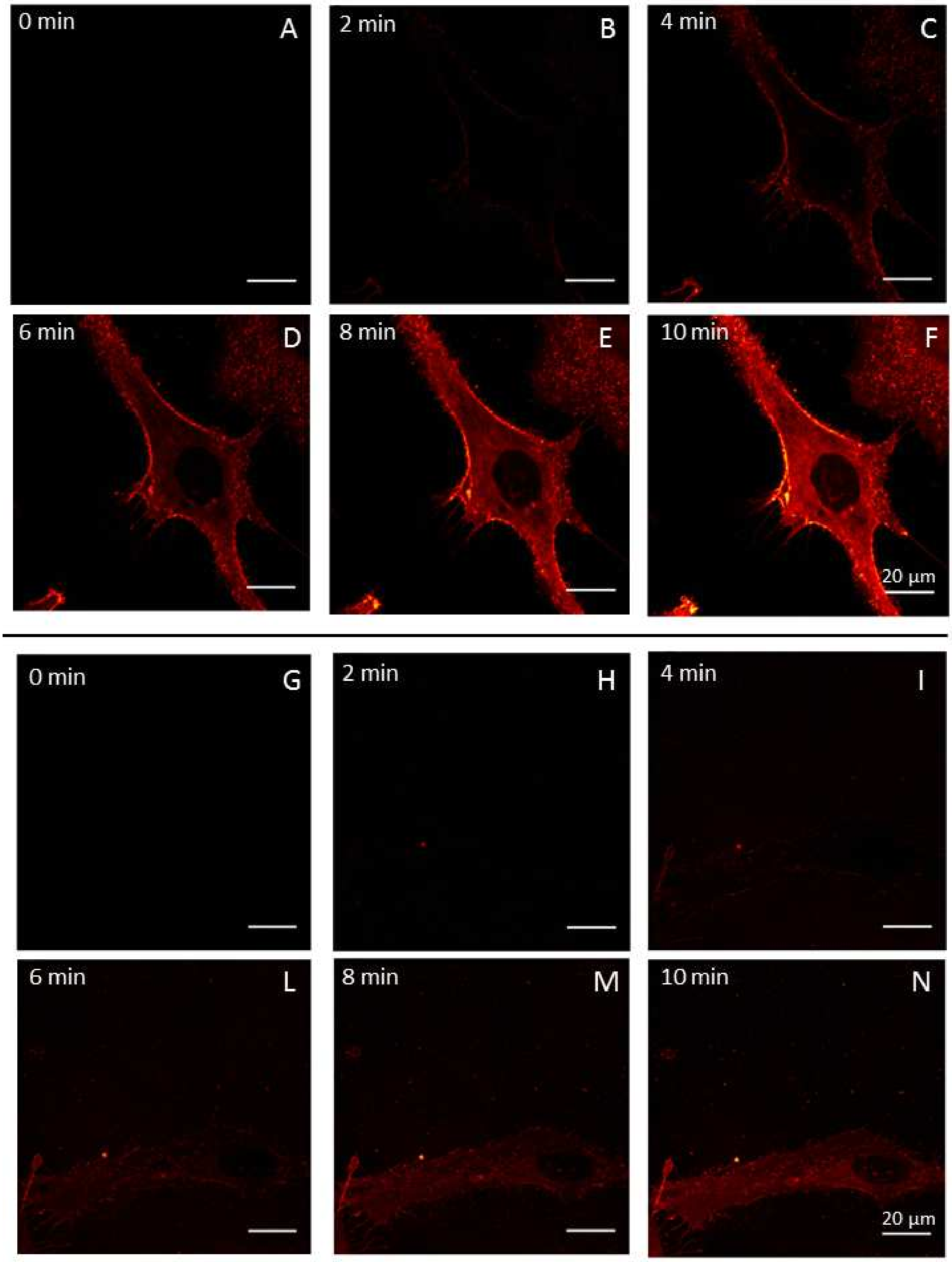

Fig. 4-16 *Comparison of spinning disk images of HeLa cells incubated with apoMb-Hyp 500nM (A-F) or Hyp 500nM (G-N). Images are collected from 0 to 10 min after the administration of the photosensitizing agent.* λ_{exc} *= 561 nm;* λ_{det} *= 590-650 nm; contrast is fixed within the same measurement.*

Spinning disk images of Fig. 4-16 A-F confirm that Hyp (500 nM) delivered with apoMb very quickly accumulates on the plasma membrane of HeLa cells. A detectable fluorescence emission can be appreciated after 2 min from the administration of apoMb-Hyp (Fig. 4-16 B), indicating that the membrane is rapidly loaded with the PS, while no fluorescence is detectable from other regions of the cell. The concentration of the PS on the membrane is better appreciated after 4 min from the administration, when also a weak fluorescence appears from the cytoplasmic region (Fig. 4-16 C), possibly favored by an increased permeability of the membrane due to the photo-damaging. Fig. 4-17 offers a detailed comparison of the (normalized) fluorescence intensity detected in a region of the cell membrane and in an internal region of the same cell. After the administration of apoMb-Hyp, the initial increase of the fluorescence intensity is faster for the membrane region (black) than for the internal (red) region for both the 500 nM (Fig. 4-17 B) and 1000 nM (Fig. 4-17 D) of PS. This indicates that Hyp delivered with apoMb accumulates faster on the membrane, which is likely to be the first component suffering from the photo-damage. At 1000 nM Hyp concentration (Fig. 4-17 D) the intensity occurring from the membrane region appears to reach a saturation after ~15 min, suggesting that the membrane is fully loaded, but only after ~25 min the two signals become identical, likely indicating a condition where the membrane is completely permeable and the PS equally distributes between the two regions. Conversely, at 500 nM Hyp (Fig. 4-17 B), it is not possible to identify a saturation: for all the observed times, the intensity from the membrane region (black) is higher than the one from the internal region (red), suggesting that, under these conditions, a preferential affinity of the membrane holds even when the cell is completely damaged, i.e. at longer times.

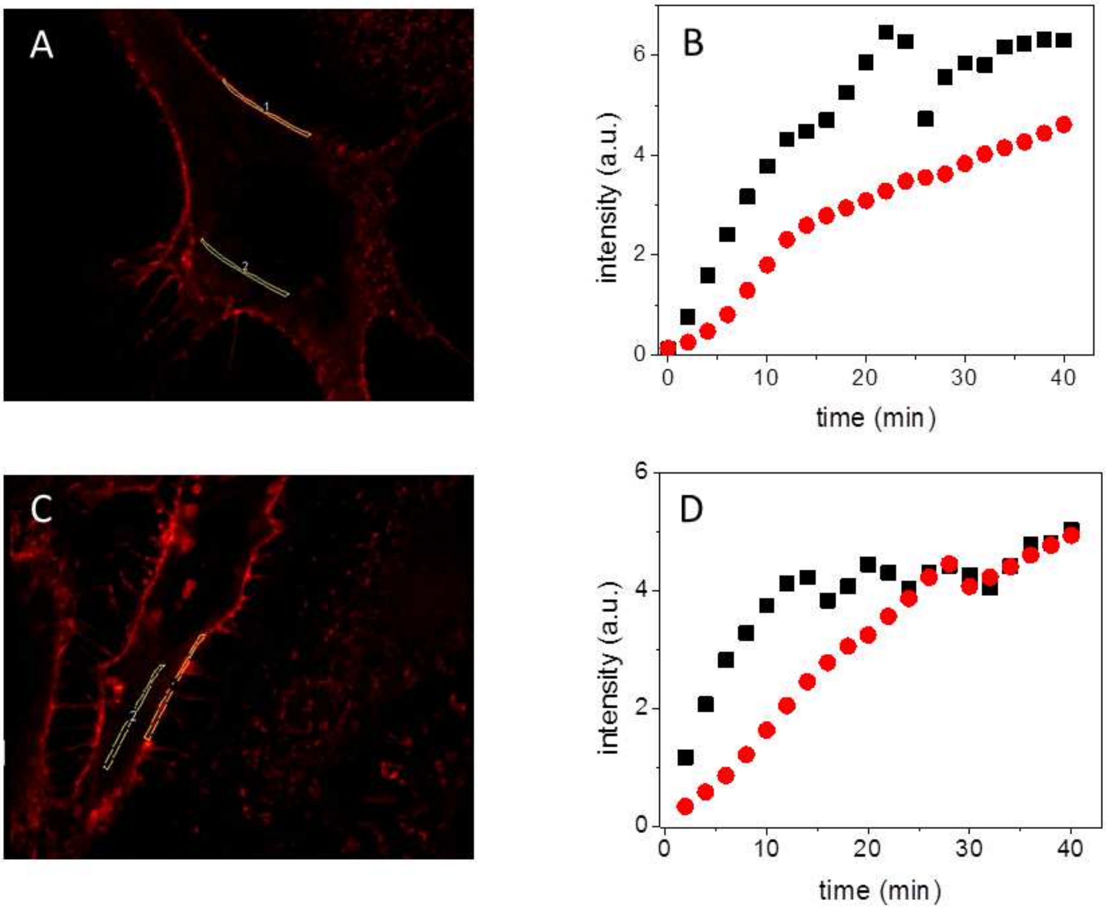

Fig. 4-17 *Analysis of the spinning disk images collected on HeLa cells incubated with apoMb-Hyp at 500 nM (A and B) or 1000 nM (C and D). B and D report the values of the fluorescence intensity integrated within a cell membrane region (black squares) and an internal region (red circles) for images collected at different times from the administration of the photosensitizing agent, from 0 to 40 min. The values of the fluorescence intensity are normalized for the area of the integration regions, which are outlined in A and C.*

A necrotic cell death is induced in consequence of the photo-damage of the cell membrane, likely occurring after few minutes (< 10 min) of observation. The effects of the necrotic damage are evident on longer observation times (> 10 min), where the structure of the cells is progressively compromised and blebbing occurs both on external and internal membranes (data not shown).

Spinning disk images of Fig. 4-16 G-N are obtained in a similar experiment where the Hyp (500 nM) is delivered to the HeLa cells as a concentrated DMSO solution, without the protein-based carrier. The emission of fluorescence is appreciable after 4 min from the administration (Fig. 4-16 I). This occurs from the internal region of the cells, where some cellular components likely corresponding to endoplasmic reticulum or mitochondria are progressively marked (Fig. 4-16 M-N), while there is no evidence for a preferential accumulation of the PS on the plasma membrane. This can be better appreciated in Fig. 4-18, where the (normalized) fluorescence intensities occurring from a membrane region (black) and from an internal region (red) appear to increase with a nearly undistinguishable trend for the first 20 min, without displaying the differences observed for Hyp delivered with apoMb (Fig. 4-17). While the signals collected for 500 nM Hyp (Fig. 4-18 B) are nearly indistinguishable for all the observation times, those collected at 1000 nM Hyp (Fig. 4-18 D) show a higher intensity from the internal region than from the membrane region for times exceeding 20 min from administration. This may be related to the accumulation of the PS on internal cellular components, once that the photo-damage allows an increased possibility of diffusion into the cell.

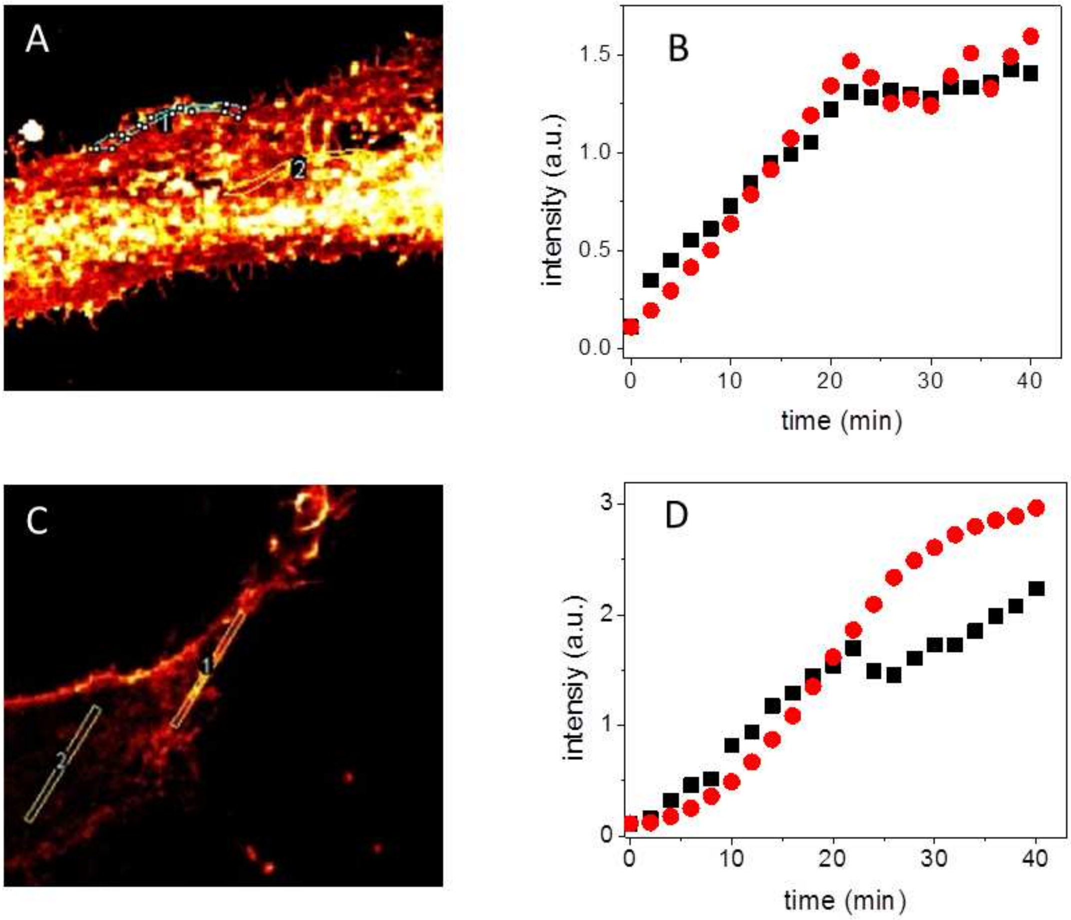

Fig. 4-18 *Analysis of the spinning disk images collected on HeLa cells incubated with Hyp at 500 nM (A and B) or 1000 nM (C and D). B and D report the values of the fluorescence intensity integrated within a cell membrane region (black squares) and an internal region (red circles) for images collected at different times from the administration of the photosensitizing agent, from 0 to 40 min. The values of the fluorescence intensity are normalized for the area of the integration regions, which are outlined in A and C.*

In summary, from the previously reported analysis Hyp appears to more rapidly interact with the HeLa cells when delivered with the apoMb carrier, since fluorescence emission can be appreciated just after 2 min from administration (Fig. 4-16 B). This is likely a consequence of the higher bio-availability of the Hyp delivered with the carrier, which limit the hydrophobic aggregation of the PS. A remarkable difference due to the presence of the protein-based carrier for Hyp with respect to the unbound PS is related to the initial distribution at the cellular level: under the conditions tested, the apoMb carrier clearly promotes the initial concentration of Hyp on the plasma membrane of HeLa cells, which is the first component subject to the photo-damage. Hyp delivered in absence of carrier appears to easily penetrate the cell membrane and accumulates in the cytoplasm, and particularly in a region likely corresponding to the endoplasmic reticulum or mitochondria (Fig. 4-16).

The above findings are consistent with previous studies dealing with Hyp showing that, when delivered at low concentration (0.5 μM in absence of a carrier), the PS associates dominantly with the endoplasmic reticulum membranes [27], where the photosensitization leads to disruption of Ca^{2+} homeostasis and rapid apoptotic cell death mediated by BAX and BAK proteins at the mitochondria [27]. That mitochondria are major targets in Hyp-based photo-treatment was also suggested by the marked and irreversible decrease in the total cellular ATP levels and in the mitochondrial respiratory function [28]. For cells photosensitized by low (≈100 nM) Hyp concentrations, apoptosis was shown to be the main death pathway, whereas at higher concentrations (≈1 μM) necrosis prevails due to the excessive photodamage. Thus, depending on the concentration of the PS, photoactivated Hyp is expected to induce either apoptosis or necrosis in HeLa cells [29]. Our results show that the delivery of Hyp with the protein-based carrier apoMb promotes an accumulation of the PS on the plasma membrane, occurring at relatively low concentration (500 nM), which is shown to induce a necrotic cell death. This is an interesting result since the inflammatory and immune-responses induced by the necrosis are often important for a complete eradication of the tumor.

Spinning disk images collected after 40 min of dark incubation of apoMb-Hyp (Fig. 4-19 A-F) or Hyp (Fig. 4-19 G-N) with HeLa cells show a rather similar distribution of the PS for the two samples. In these conditions the presence of the protein-based carrier poorly affects the initial distribution of Hyp on the cells. In both cases, the rather long incubation time allows the PS to penetrate into the cell and extensively mark internal structures, except the nucleus. Thus, the concentration of the PS into the cell is so high that the irradiation necessary for the acquisition of the first few frames already induces an extensive photo-damage to the cells leading to necrosis.

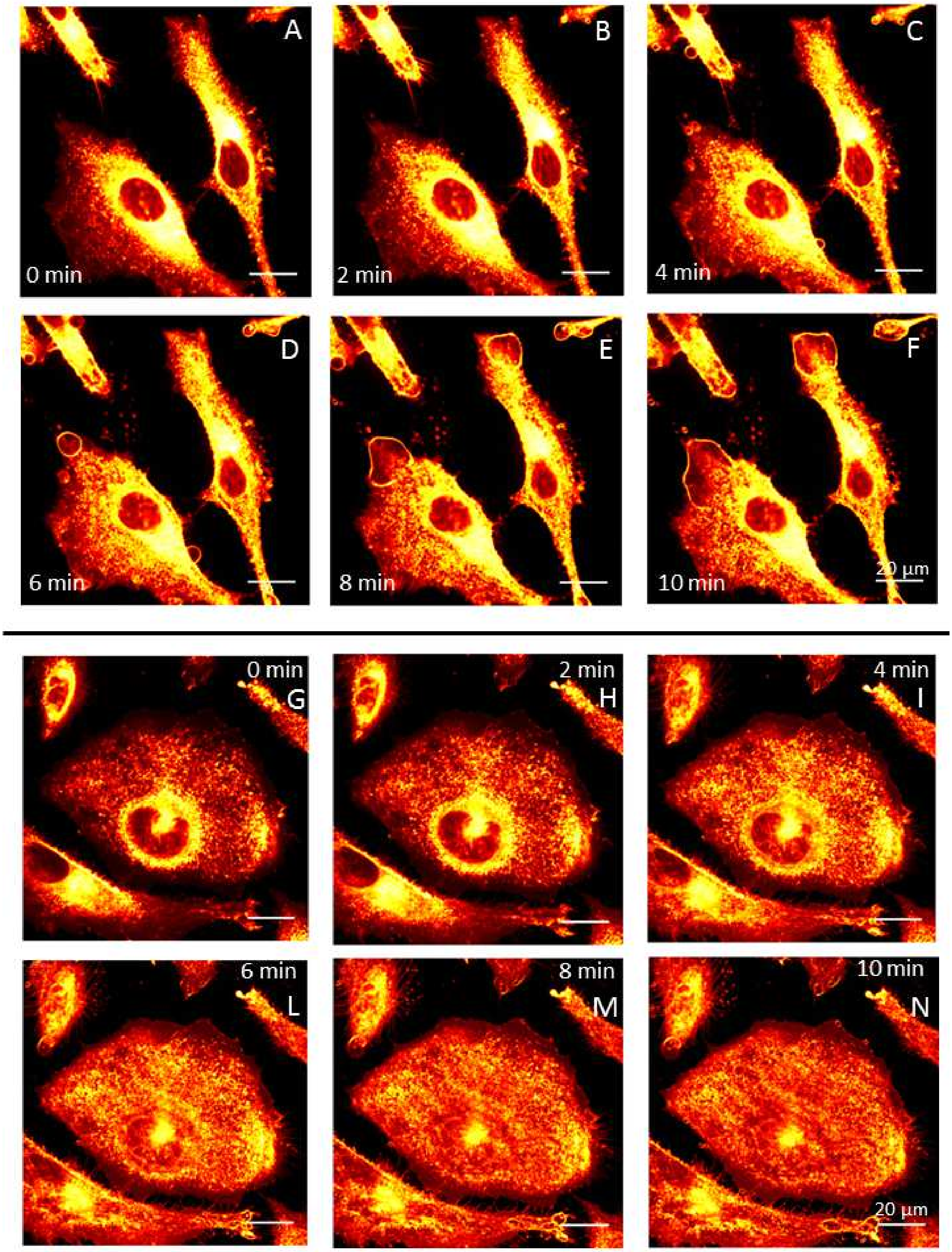

Fig. 4-19 *Comparison of spinning disk images of HeLa cells incubated with apoMb-Hyp 500 nM (A-F) or Hyp 500 nM (G-N). Images are collected from 0 to 10 min after an dark incubation period of 40 min with the photosensitizing agent.* λ_{exc} *= 561 nm;* λ_{det} *= 590-650 nm; contrast is fixed within the same measurement.*

4.1.6.2.2 PC3

The same experiment are repeated on PC3 cell line. The results are fairly similar to those of HeLa, even if the shape of the selected PC3 cells appear to be more rapidly perturbed by the photo-induced damage, than HeLa. The analysis are thus affected by a higher uncertainty, even though some main conclusions can be drawn.

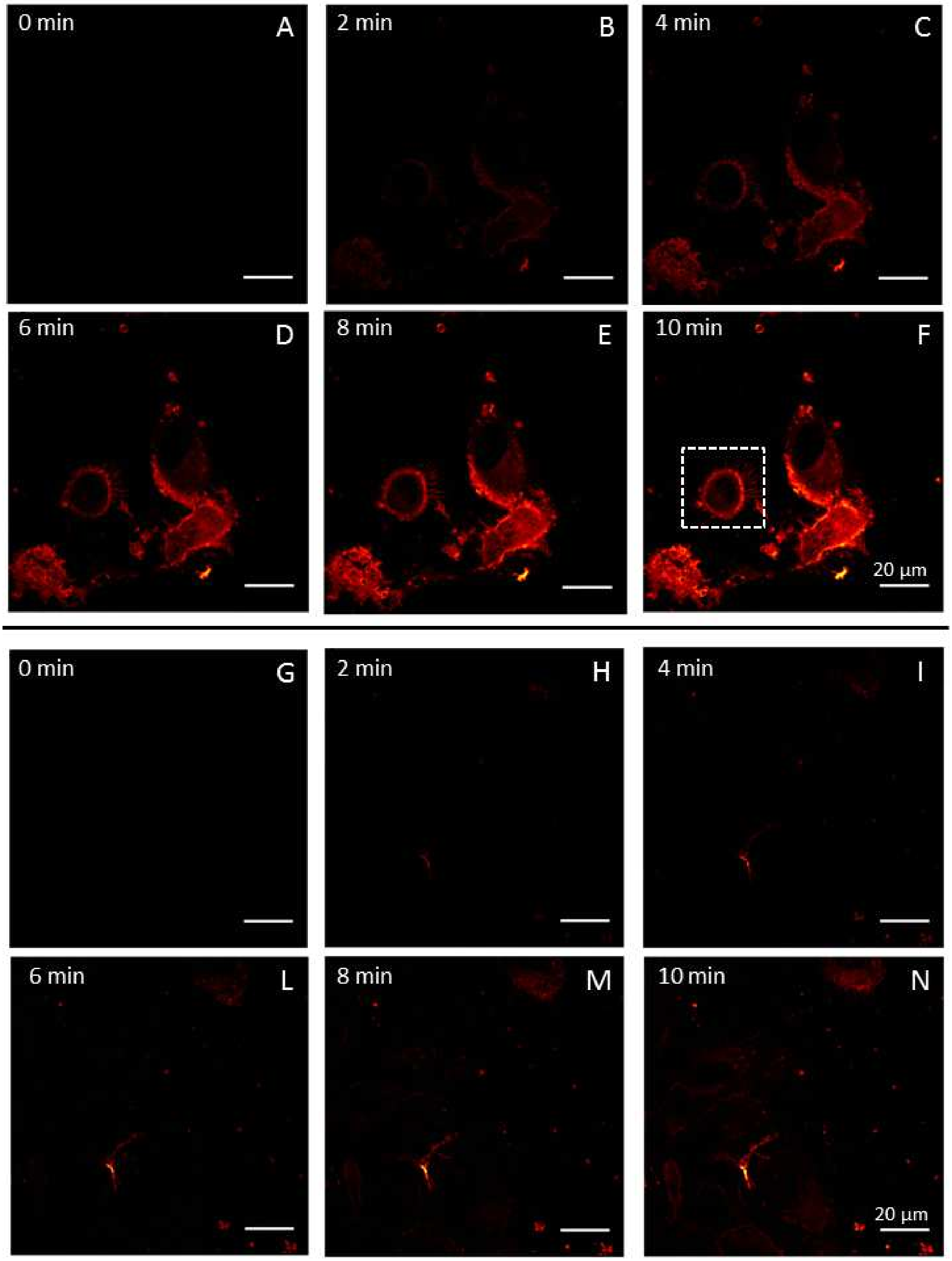

Fig. 4-20 *Comparison of spinning disk images of PC3 cells incubated with apoMb-Hyp 500nM (A-F) or Hyp 500nM (G-N). Images are collected from 0 to 10 min after the administration of the photosensitizing agent.* λ_{exc} *= 561 nm ;* λ_{det} *= 590-650 nm; contrast is fixed within the same measurement. The dashed box in F outline the healthy cell considered for discussion.*

Fig. 4-20 compares the spinning disk images collected within 10 min after the administration of apoMb-Hyp 500nM (Fig. 4-20 A-F) and Hyp 500 nM (Fig. 4-20 G-N) to PC3 cells. Some of the cells displayed in Fig. 4-20 A-F appear already damaged from the very first observation times, showing bubble formation and poorly defined components. The cell that is outlined in Fig. 4-20 F appears healthy and with a well-defined structure. It does not appear to undergo an extensive photo-damage after the very first observations, and so is conveniently taken as reference for the discussion. As observed for HeLa cells, after 2 min from the administration of apoMb-Hyp 500 nM, fluorescence mainly occurs from the region corresponding to the plasma membrane of the cells, with negligible fluorescence from the internal part (Fig. 4-20 B). The fluorescence emission from the membrane gets progressively more intense and a careful inspection allows to identify the formation of bubble-like structures, which are the typical consequences of the photo-damage (Fig. 4-20 E-F). The permeability of the cell membrane increases rapidly, allowing the penetration of the PS in the internal region, from which a fluorescence is detectable after ~6 min (Fig. 4-20 D).

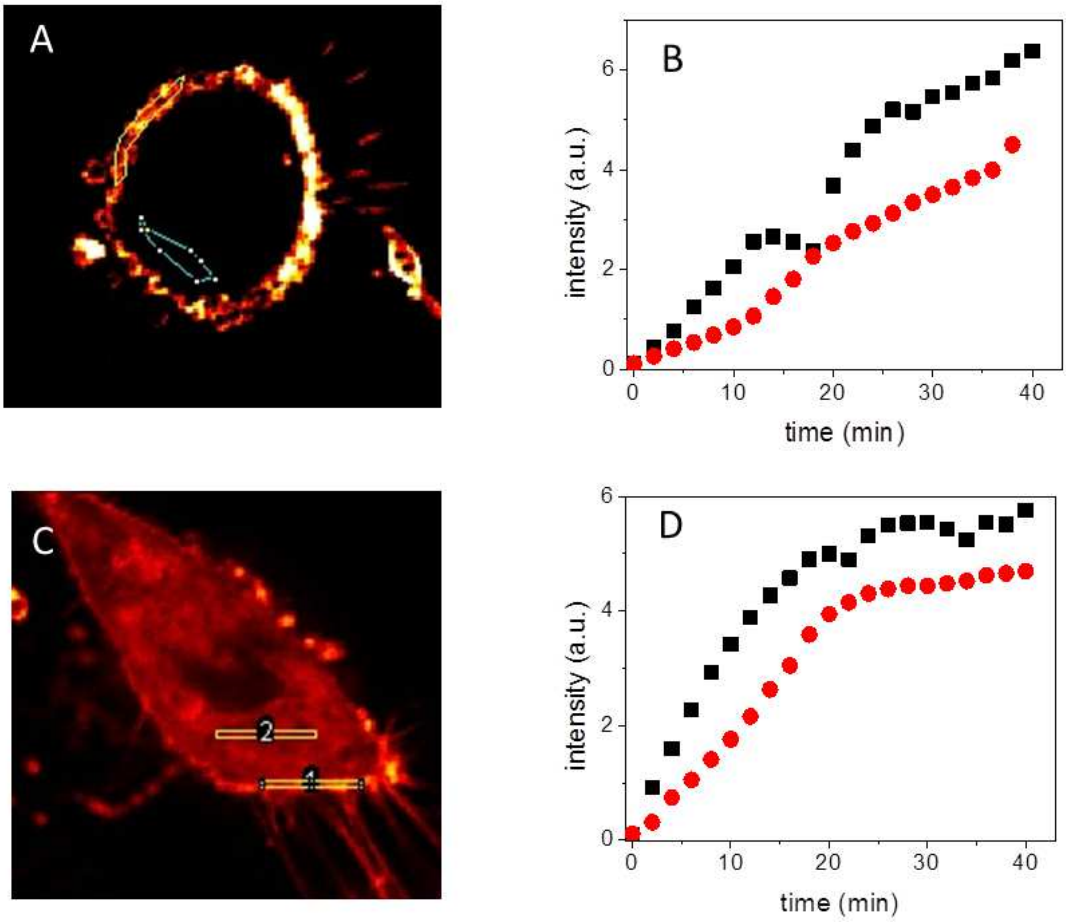

***Fig. 4-21** Analysis of the spinning disk images collected on PC3 cells incubated with apoMb-Hyp at 500 nM (A and B) or 1000 nM (C and D). B and D report the values of the fluorescence intensity integrated within a cell membrane region (black squares) and an internal region (red circles) for images collected at different times from the*

administration of the photosensitizing agent, from 0 to 40 min. The values of the fluorescence intensity are normalized for the area of the integration regions, which are outlined in A and C.

Fig. 4-21 proposes the comparison of the (normalized) fluorescence intensity integrated within an area of the plasma membrane and of the internal cell region, monitored from 0 to 40 min from the administration of the apoMb-Hyp. The data allow to appreciate that the cell membrane is the component that is more rapidly loaded with the PS, as previously observed for HeLa cells. In both Fig. 4-21 B, relative to apoMb-Hyp 500 nM, and Fig. 4-21 D, relative to apoMb-Hyp 1000 nM, the fluorescence intensity increases more rapidly for the membrane region (black) than for the internal region (red). A saturation of the intensity can be observed only for the higher concentration of Hyp and after ~25 min from the administration (Fig. 4-21 D). However, the extent of the intensity is constantly higher from the membrane region than from the internal one.

The spinning disk images collected for the PC3 cells incubated with Hyp delivered as concentrated solution, in absence of protein-based carrier (Fig. 4-20 G-N), appear more confused. Just after 2 min from the administration of the PS, a rather intense fluorescence can be noticed only from a small region, corresponding to a not well identified component (Fig. 4-20 H). However, there is no evidence for a preferential accumulation of the fluorescence on the whole plasma membrane within the first 10 min. As observed for HeLa cells, the fluorescence is slower to appear than for the case of Hyp delivered with apoMb. Only after 8 – 10 min from the administration, an emission is identifiable occurring from the cytoplasmic region (Fig. 4-20 M-N). This conclusion is better supported by the results reported in Fig. 4-22, when the (normalized) integrated fluorescence intensities within two regions located on the plasma membrane (black) and on the internal part of the cell (red) are compared. The two signals obtained for the sample with 500 nM Hyp are very similar, and nearly undistinguishable in the first 20 min of observation (Fig. 4-22 B). From the comparison of signal obtained for 1000 nM Hyp (Fig. 4-22 D) a slightly faster increase of intensity from the membrane region is possibly observed, even though the trend of the two curves is very similar. The results are less clear than those obtained on HeLa cells, probably because of the faster damaging experienced by the cells, which affects the integrity of the cellular components.

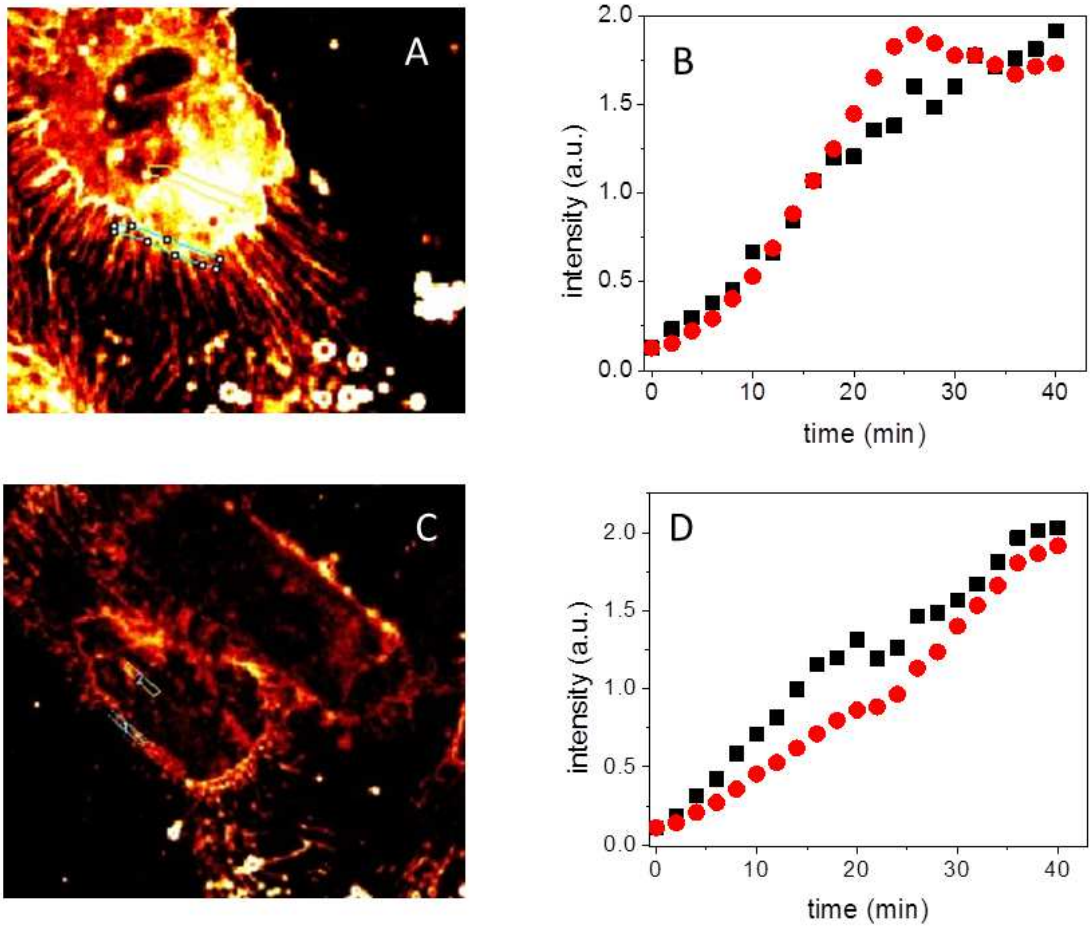

Fig. 4-22 *Analysis of the spinning disk images collected on PC3 cells incubated with Hyp at 500 nM (A and B) or 1000 nM (C and D). B and D report the values of the fluorescence intensity integrated within a cell membrane region (black squares) and an internal region (red circles) for images collected at different times from the administration of the photosensitizing agent, from 0 to 40 min. The values of the fluorescence intensity are normalized for the area of the integration regions, which are outlined in A and C.*

Despite more confused, the results obtained on PC3 cells can be considered comparable to those previously reported for HeLa cells. In particular, the delivery of Hyp with apoMb appears to increase the bio-availability of the PS and to promote its initial accumulation on the plasma membrane. When Hyp is administered in absence of the carrier, it tends to penetrate the membrane and locate in the cytoplasmic region. The extensive bubbling occurring at longer observation times (data not shown) do not allow to precisely identify the internal component where Hyp accumulates. Similarly to the case of HeLa cells, it can be speculated that these correspond to the endoplasmic reticulum or mitochondria.

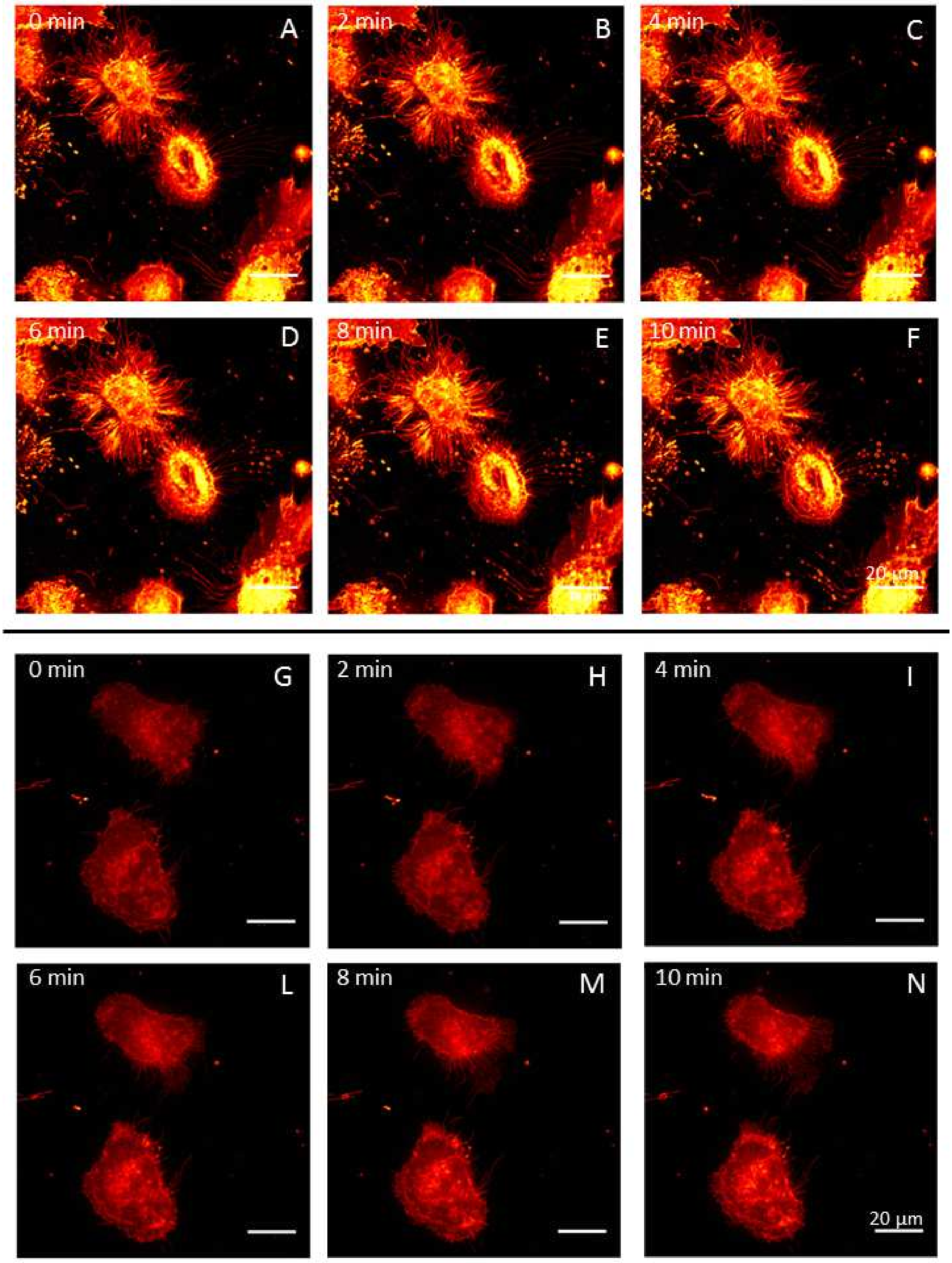

Fig. 4-23 *Comparison of spinning disk images of PC3 cells incubated with apoMb-Hyp 500nM (A-F) or Hyp 500nM (G-N). Images are collected from 0 to 10 min after an dark incubation period of 40 min with the photosensitizing agent.* λ_{exc} *= 561 nm;* λ_{det} *= 590-650 nm; contrast is fixed within the same measurement.*

Spinning disk images collected after 40 min of dark incubation of apoMb-Hyp or Hyp with PC3 cells (Fig. 4-23) show a rather similar distribution of the PS for the two samples. Under these conditions the presence of the protein-based carrier poorly affects the distribution of Hyp on the cells after incubation. In both cases, the rather long incubation time allows the PS to penetrate into the cell and extensively mark internal membranes. The concentration of the PS into the cell is so high that the irradiation necessary for the acquisition of the first frame already induces an extensive photo-damage to the cells leading to necrosis.

4.1.6.3 Tumor cells photo-inactivation

Cell viability of HeLa and PC3 cells in the presence of Hyp or apoMb-Hyp was determined as a function of PS concentration and light dose. A clear concentration-dependent cytotoxic effect can be observed at all irradiation times (2, 5 and 15 minutes, corresponding respectively to a light dose of 3.6, 9.2 and 27.6 J cm^{-2}) both for HeLa and PC3 cells. Increasing exposure times induced a higher cytotoxicity of both Hyp and apoMb-Hyp. The value for LC_{50} for Hyp, i.e. the lethal dose which causes 50% decrease in cell viability, decreased from 1255 nM to 127 nM (10-fold) when treatment was increased from 2 to 15 minutes on PC3 cells. A similar effect can be observed on Hela cells where LC_{50} decreased from 1335 nM to 233 nM (6-fold). Complexation of Hyp with apoMb significantly increased the phototoxic effect of Hyp, reducing the LC_{50} from 667 to 224 nM and from 664 to 149 nM for PC3 and HeLa cells, respectively (Tab. 4-4).

		PC3		HeLa	
Exposure time (min)	**Light dose (J cm^{-2})**	**Hyp**	**apoMb-Hyp**	**Hyp**	**apoMb-Hyp**
0	**0**	nc	nc	nc	nc
2	**3.6**	1255	212	1335	234
5	**9.2**	667	224	664	149
15	**27.6**	127	51	233	85

Tab. 4-4 *LC_{50} (nM) of Hyp and apoMb-Hyp on PC3 and HeLa cells when exposed to light. The concentration of apoMb is always kept in excess with respect to Hyp (3:1), in order to ensure the formation of the apoMb-Hyp complex, that is then administrated to the cells.*

This effect can be clearly appreciated in Fig. 4-24 by comparing dotted lines with continuous lines. These data unequivocally show that, under the employed conditions, apoMb-Hyp is an effective PS for in vitro photosensitization-based tumor cells inactivation and outperforms Hyp.

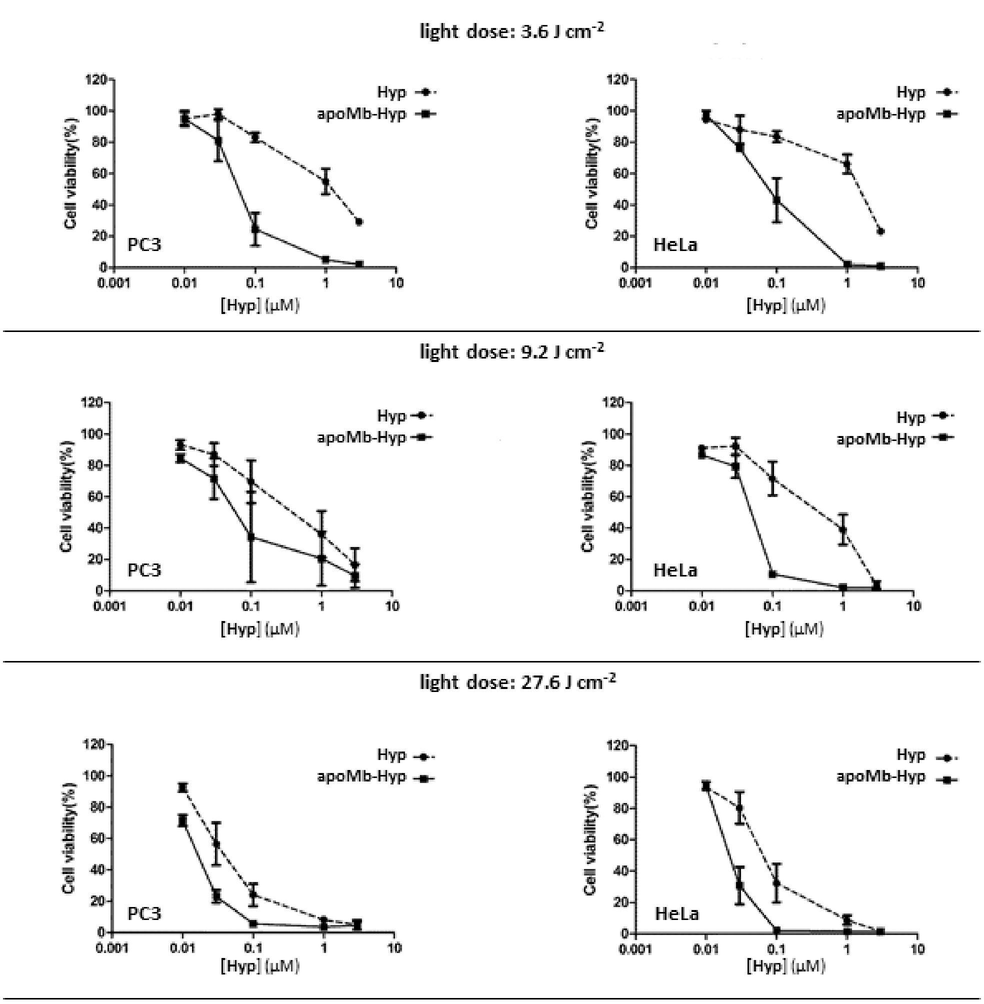

Fig. 4-24 *Dose dependent effect on HeLa (left) and PC3 (right) cells incubated with Hyp or apoMb-Hyp (0.03 – 3 µM) and exposed to blue light doses corresponding to 3.6 (top), 9.2 (middle) and 27.6 (bottom) J cm^{-2}. The concentration of apoMb is always kept in excess with respect to Hyp (3:1), in order to ensure the formation of the apoMb-Hyp complex, that is then administrated to the cells.*

The higher efficiency of apoMb-Hyp over Hyp in leading to cell death may be associated with an improved binding of the PS with the investigated tumor cells owed to the presence of the protein-based carrier. Interestingly, such possibility was investigated for Hyp associated with HSA, and was concluded that, besides acting as a passive carrier for Hyp, HSA may also actively contribute to the selective localization of the compound [30]. The above-reported results obtained with spinning disk and STED imaging techniques unequivocally show that the uptake process leading to the accumulation of Hyp on the cell membrane is favored by the apoMb carrier. This suggests that the protein-based carrier may have an active role in the preferential interaction of the PS on these cells. However, we cannot exclude that the improved photo-toxicity observed in the presence of the protein-based carrier arises from simpler passive effects like, for example, a higher amount of bio-available Hyp due to the less extended aggregation of the PS.

The high resolution attainable through the apoMb-Hyp fluorescence emission, along with the photosensitizing properties of the compound, opens interesting new therapeutic possibilities.
Indeed, the diagnostic capability of Hyp (through fluorescence imaging) and its therapeutic action based on photosensitization were reported to allow a selective visualization of malignant gliomas [31]. A recent study compared the phototoxic effects of Hyp on medulloblastoma cells in vitro, with those of the 5-aminolevulinic acid-derived protoporphyrin IX (5-ALA-derived PP IX) [32]. Hyp fluorescence was easily distinguishable from cell autofluorescence and showed higher photocytotoxicity compared to 5-ALA-derived PP IX. It was concluded that Hyp may be considered as a contrast photoactive agent for intraoperative visualization and photodynamic treatment of medulloblastomas.

4.1.7 Chapter bibliography

1. Yamazaki, T., Ohta, N., Yamazaki, I. & Song, P. S. Excited-state properties of hypericin: electronic spectra and fluorescence decay kinetics. *J. Phys. Chem.* **97,** 7870–7875 (1993).
2. Wynn, J. L. & Cotton, T. M. Spectroscopic Properties of Hypericin in Solution and at Surfaces. *J. Phys. Chem.* **99,** 4317–4323 (1995).
3. Weitman, H. *et al.* Solvatochromic Effects in the Electronic Absorption and Nuclear Magnetic Resonance Spectra of Hypericin in Organic Solvents and in Lipid Bilayers. *Photochem. Photobiol.* **73,** 110–118 (2001).
4. Redmond, R. W. & Gamlin, J. N. A Compilation of Singlet Oxygen Yields from Biologically Relevant Molecules. *Photochem. Photobiol.* **70,** 391–475 (1999).
5. Losi, A. Fluorescence and Time-Resolved Photoacoustics of Hypericin Inserted in Liposomes: Dependence on Pigment Concentration and Bilayer Phase. *Photochem. Photobiol.* **65,** 791–801 (1997).
6. Crutzen, M., Ameloot, M., Boens, N., Negri, R. M. & De Schryver, F. C. Global analysis of unmatched polarized fluorescence decay curves. *J. Phys. Chem.* **97,** 8133–8145 (1993).
7. Comas-Barceló, J. *et al.* A self-assembled nanostructured material with photosensitising properties. *RSC Adv.* **3,** 17874 (2013).
8. Baier, J., Maier, M., Engl, R., Landthaler, M. & Bäumler, W. Time-Resolved Investigations of Singlet Oxygen Luminescence in Water, in Phosphatidylcholine, and in Aqueous Suspensions of Phosphatidylcholine or HT29 Cells. *J. Phys. Chem. B* **109,** 3041–3046 (2005).
9. Nonell, S. & Braslavsky, S. E. in *Singlet Oxygen, UV-A, and Ozone* (ed. Lester Packer, H. S. B. T.-M. in E.) **Volume 319,** 37–49 (Academic Press, 2000).
10. English, D. S. *et al.* Hypericin, Hypocrellin, and Model Compounds: Primary Photoprocesses of Light-Induced Antiviral Agents. *J. Phys. Chem. A* **101,** 3235–3240 (1997).
11. Hell, S. W. Far-Field Optical Nanoscopy. *Science (80-.).* **316,** 1153–1158 (2007).
12. Gai, F., Fehr, M. J. & Petrich, J. W. Role of Solvent in Excited-State Proton Transfer in Hypericin. *J. Phys. Chem.* **98,** 8352–8358 (1994).
13. Das, K., Smirnov, A. V, Snyder, M. D. & Petrich, J. W. Picosecond Linear Dichroism and Absorption Anisotropy of Hypocrellin: Toward a Unified Picture of the Photophysics of Hypericin and Hypocrellin. *J. Phys. Chem. B* **102,** 6098–6106 (1998).
14. Das, K., Smirnov, A. V, Wen, J., Miskovsky, P. & Petrich, J. W. Photophysics of Hypericin and Hypocrellin A in Complex with Subcellular Components: Interactions with Human Serum Albumin. *Photochem. Photobiol.* **69,** 633–645 (1999).
15. Klar, T. A., Jakobs, S., Dyba, M., Egner, A. & Hell, S. W. Fluorescence microscopy with diffraction resolution barrier broken by stimulated emission. *Proc. Natl. Acad. Sci. U. S. A.* **97,** 8206–8210 (2000).
16. Margolin, W. Sculpting the Bacterial Cell. *Curr. Biol.* **19,** R812–R822 (2015).
17. Osborn, M. J. & Rothfield, L. Cell shape determination in Escherichia coli. *Curr. Opin. Microbiol.* **10,** 606–610 (2007).
18. Gerding, M. A., Ogata, Y., Pecora, N. D., Niki, H. & De Boer, P. A. J. The trans-envelope Tol–Pal complex is part of the cell division machinery and required for proper outer-membrane invagination during cell constriction in E. coli. *Mol. Microbiol.* **63,** 1008–1025 (2007).
19. Lleo, M. M., Canepari, P. & Satta, G. Bacterial cell shape regulation: testing of additional predictions unique to

the two-competing-sites model for peptidoglycan assembly and isolation of conditional rod-shaped mutants from some wild-type cocci. *J. Bacteriol.* **172,** 3758–3771 (1990).

20. Vollmer, W. & Seligman, S. J. Architecture of peptidoglycan: more data and more models. *Trends Microbiol.* **18,** 59–66 (2010).
21. Sperandio, F. F., Huang, Y.-Y. & Hamblin, M. R. Antimicrobial Photodynamic Therapy to Kill Gram-negative Bacteria. *Recent Pat Antiinfect Drug Discov* **8,** 1–23 (2013).
22. Demidova, T. N. & Hamblin, M. R. Photodynamic Inactivation of Bacillus Spores, Mediated by Phenothiazinium Dyes. *Appl. Environ. Microbiol.* **71,** 6918–6925 (2005).
23. Doan, T., Marquis, K. A. & Rudner, D. Z. Subcellular localization of a sporulation membrane protein is achieved through a network of interactions along and across the septum. *Mol. Microbiol.* **55,** 1767–1781 (2005).
24. Roslaniec, M., Weitman, H., Freeman, D., Mazur, Y. & Ehrenberg, B. Liposome binding constants and singlet oxygen quantum yields of hypericin, tetrahydroxy helianthrone and their derivatives: studies in organic solutions and in liposomes. *J. Photochem. Photobiol. B Biol.* **57,** 149–158 (2000).
25. Lenci, F. *et al.* Spectroscopic and photoacoustic studies of Hypericin embedded in liposomes as a photoreceptor model. *Photochem. Photobiol.* **62,** 199–204 (1995).
26. Das, K. *et al.* Hypericin, Hypocrellin, and Model Compounds: Steady-State and Time-Resolved Fluorescence Anisotropies. *J. Phys. Chem. B* **102,** 1479–1484 (1998).
27. Buytaert, E. *et al.* Role of endoplasmic reticulum depletion and multidomain proapoptotic BAX and BAK proteins in shaping cell death after hypericin-mediated photodynamic therapy. *FASEB J.* **20,** 756–758 (2006).
28. Johnson, S. A. S., Dalton, A. E. & Pardini, R. S. Time-Course of Hypericin Phototoxicity and Effect on Mitochondrial Energies in EMT6 Mouse Mammary Carcinoma Cells. *Free Radic. Biol. Med.* **25,** 144–152 (1998).
29. Vantieghem, A. *et al.* Hypericin-induced photosensitization of HeLa cells leads to apoptosis or necrosis. *FEBS Lett.* **440,** 19–24 (1998).
30. Roelants, M., Van Cleynenbreugel, B., Lerut, E., Van Poppel, H. & de Witte, P. A. M. Human serum albumin as key mediator of the differential accumulation of hypericin in normal urothelial cell spheroids versusurothelial cell carcinoma spheroids. *Photochem. Photobiol. Sci.* **10,** 151–159 (2011).
31. Ritz, R. *et al.* Hypericin for visualization of high grade gliomas: First clinical experience. *Eur. J. Surg. Oncol.* **38,** 352–360 (2012).
32. Ritz, R. *et al.* In Vitro comparison of Hypericin and 5-Aminolevulinic Acid-Derived Protoporphyrin IX for Photodynamic Inactivation of Medulloblastoma Cells. *PLoS One* **7,** e51974 (2012).

4.2 Nanostructures based on globins: Zn-substituted myoglobin

Zn-substituted myoglobin (ZnMb) can be considered an example of a protein-based nanostructure where the globin structure of apoMb is able to bind covalently and carry a photo-physically active PS molecule (Zn-PP IX). Unlike the previously described globin-based nanostructure of apoMb-Hyp, where the interaction between the photo-physically active molecule of Hyp and the protein-based carrier occurred essentially by hydrophobic effect, in ZnMb the active Zn-PP IX molecule is more strongly bound to the globin structure of apoMb, thanks to a direct covalent bond. The active PS molecule Zn-PP IX is identical to the natural cofactor found in Mb, i.e. the heme group (Fe-PP IX), except for the presence of a Zn(II) ion, heavier than the iron ion found in the heme, coordinated at the center of the tetrapyrrole ring of PP IX (Fig. 4-25).

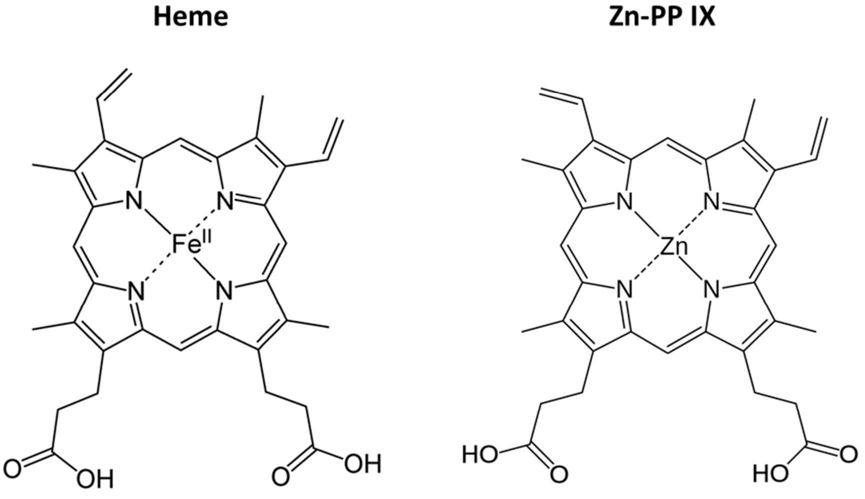

Fig. 4-25 *Comparison of the chemical structure of heme and Zn-PP IX.*

Beside the hydrophobic effect, a coordination bond is therefore occurring between Zn and the proximal Histidine amino acid, placed in the main hydrophobic cavity of apoMb. Thus, a Mb molecule is reconstituted where the iron ion is replaced by a Zn(II) ion at the center of the prosthetic group (ZnMb).

Given the strength of the coordination bond occurring between the PS and the protein-based carrier, much more intense than the interaction between apoMb and Hyp, ZnMb can be considered as a whole for the purpose of this work. Indeed the dissociation of Zn-PP IX from the protein, while possible, is unlikely to occur and there is no sign of such dissociation from the spectral properties of the complex, that appears stable under the used experimental conditions. This is a remarkable difference with the apoMb-Hyp nanostructure, for which the micro-molar K_d of the complex [1] may allow partial translocation of Hyp to other structures present in many biological environments, like for example serum proteins [2].

Additionally, the spontaneous formation of ZnMb has been observed during the maturation of not cooked hams that are not treated with additives (see 4.2.3), so that ZnMb can be effectively considered a real naturally occurring and bio-compatible protein-based PS. This is particularly relevant since few cases are reported of this kind of PS, where the ROS are produced inside the structure of a protein. Variants of the Green Fluorescent Protein (GFP) family [3] [4], the protein “killer-RED” [5] [6] and the flavoprotein “mini Singlet Oxygen Generator” (mini-SOG) [7] [8] are relevant examples of genetically-encoded protein-based PS, but characterized by a very low quantum yield of $^1O_2$ production, e.g. $\Phi_\Delta = (0.004 \pm 0.001)$ for Enhanced-GFP and (0.03 ± 0.01) for mini-SOG. Conversely, ZnMb is an extremely efficient PS, able to photosensitize $^1O_2$ with a quantum yield close to unity [9].

4.2.1 Photo-physical properties of ZnMb

Fig. 4-26 shows the absorption and fluorescence emission spectra measured for ZnMb in a PBS buffered solution, that closely match those reported in literature [9]. The typical features of the porphyrin-based cromophores can be recognized in the absorption spectrum, which is characterized by an intense Soret band centered at 428 nm and two Q-bands, about 16 times weaker, centered at 554 and 595 nm. The fluorescence emission spectrum shows an intense narrow band with a maximum at 597 nm, and broader, less intense emission band at ~650 nm.

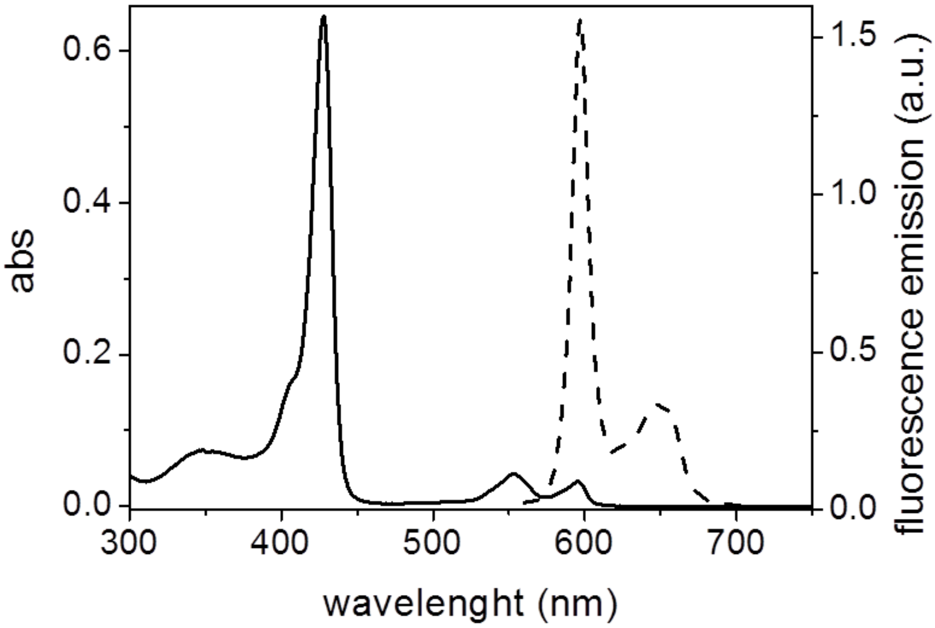

Fig. 4-26 *Absorption (solid) and fluorescence emission (dashed) spectra of ZnMb 4 μM in PBS buffer, T = 20°C.*

The fluorescence decay of ZnMb in PBS buffer is well described by a mono-exponential model yielding a lifetime τ_F = (2.0 ± 0.1) ns (Tab. 4-5). Monitoring of the transient T-T absorption of ZnMb at ~465 nm after a ns laser excitation at 532 nm, allowed to determine the value for τ_T. As can be observed in Tab. 4-5, the value ranges from (26 ± 0.1) µs in air-equilibrated PBS to (13 ± 1) ms in deaerated solution, with a response to the presence of dissolved O_2 which is consistent with what is expected for a triplet state and in agreement with previous determination [9] [10]. The value retrieved for τ_T in an air-equilibrated solution is substantially larger when compared to the typical τ_T of organic PSs in air-saturated aqueous solutions (2-3 µs) [11]. As for the Hyp bound to the cavity of apoMb, the long value of τ_T indicates that the PS is effectively shielded from the O_2 present in the solvent, in agreement with the localization of the Zn-PP IX within the cavity of the protein structure. The values of τ_T determined indirectly by the monitoring of time-resolved NIR phosphorescence produced by $^1O_2$ are in agreement with the one directly determined by transient absorption, with differences due to minor changes in the experimental conditions (Tab. 4-5). In turn, the values measured for the $^1O_2$ lifetimes are nicely consistent with literature values for similar systems [1] [12]. The spectroscopic properties determined for ZnMb in PBS buffer are consistent with those reported by Lepeshkevich et al. for ZnMb in a 50 mM citrate-phosphate buffer, pH = 7.4 [9]. It is thus possible to conclude that a successful reproduction of spectroscopically stable ZnMb was obtained, for which the reported value for the $^1O_2$ generation is Φ_Δ = (0.9 ± 0.1).

Sample	**τ_F (ns)**	**D ($\mu m^2 s^{-1}$)**	**τ_T (µs) air-equilibrated**	**τ_T (ms) nitrogen-saturated**	**τ_Δ (µs)**
ZnMb	$2.0\pm0.1^{\$}$		$26\pm1^{*}$ $19\pm2^{\pounds}$	$13\pm1^{*}$	$2.6\pm0.3^{\pounds}$
ZnMb with *E. coli*	$2.1\pm0.1^{\$}$	$0.12\pm0.02^{\$}$	$29\pm3^{*}$ $20\pm2^{\pounds}$	$11\pm1^{*}$	$2.6\pm0.3^{\pounds}$
ZnMb with *S. aureus*	$2.1\pm0.1^{\$}$	$0.31\pm0.05^{\$}$	$34\pm3^{*}$ $22\pm2^{\pounds}$	$13\pm1^{*}$	$2.6\pm0.3^{\pounds}$

Tab. 4-5 *Photo-physical parameters for ZnMb in PBS buffer and ZnMb incubated with E. coli and S. aureus cells.*$^{\$}$*: FCS / TCSPC* λ_{exc} *= 475 nm,* λ_{det} *= 650-700 nm, [ZnMb] ≈ 1 µM ;*: LFP, [ZnMb] = 2 or 5 µM ;* $^{\pounds}$*: time-resolved phosphorescence (TRP)* λ_{exc} *= 532 nm,* λ_{det} *= 1275 nm, 1 kHz, [ZnMb] = 10 µM; deoxygenation: 1 hour flux pure nitrogen.*

4.2.2 ZnMb and bacterial cells

Given the spontaneous presence of ZnMb in additive-free dry cured hams, the behavior of ZnMb was firstly studied on bacterial cells, which may constitute an interesting target for ZnMb induced photosensitization, with potential applications for the decontamination of these foods. Indeed, the particularly efficient $^1O_2$ photosensitizing ability of ZnMb suggests that this PS could be fruitfully employed as antimicrobial agent. Since the results obtained with the globin-based nanostructure of apoMb-Hyp pointed out fundamental differences between Gram-positive and Gram-negative bacteria in response to photosensitization [13], we focused our attention on representatives of the two types, namely *S. aureus* and *E. coli*.

4.2.2.1 Loading of ZnMb on bacteria

The presence of an interaction between ZnMb and bacterial cells is directly demonstrated exploiting the fluorescence emission of the PS to collect images with a confocal microscope. Both *S. aureus* and *E. coli* suspensions were incubated with ~1 μM ZnMb for 10 min before taking images. The resolution of confocal images is quite poor because of the faint fluorescence emission and the rapid photo-bleaching experienced by the compound. However, a clear accumulation of the fluorescent ZnMb on bacterial cells is evident by comparing the confocal images with those obtained in transmitted light mode, for both *S. aureus* (Fig. 4-27 A-C) and *E. coli* (Fig. 4-28 A-C). Washed samples obtained by mild centrifugation and removal of the supernatant show a substantial reduction of the ZnMb fluorescence from both *S. aureus* (Fig. 4-27 D-F) and *E. coli* (Fig. 4-28 D-F), which becomes barely distinguishable from the background. This result indicates that the interaction between the protein and the bacterial cell wall is rather weak and that the ZnMb is negligibly internalized by the cells. Attempts to reach an improved subdiffraction resolution using a STED microscope and exploiting the fluorescence emission of the ZnMb failed, possibly because of the low quantum yield of fluorescence emission and the transient absorption properties of the ZnMb, which precluded the depletion of the excited state. Thus, it was not possible to obtain a more detailed imaging of the distribution of the PS on specific components of the bacterial cell.

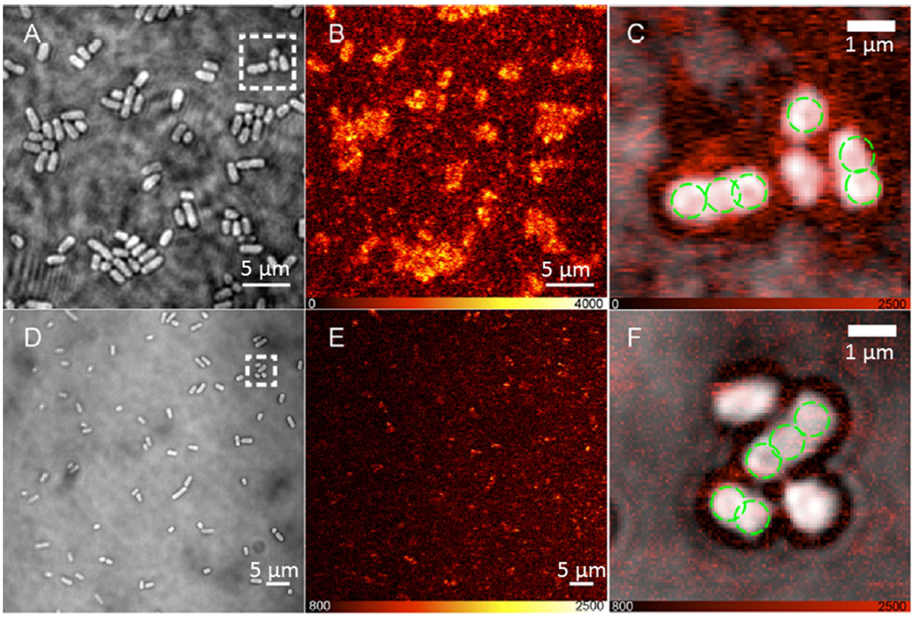

Fig. 4-27 *Comparison of selected images of S. aureus incubated with 1 µM ZnMb (A-C) and S. aureus incubated 1 µM ZnMb and washed by means of centrifugation. Images acquired with a confocal microscope using transmitted light (A and D) and confocal fluorescence (B and E) exploiting the emission of ZnMb (λ_{exc} = 561 nm, λ_{det} = 600−670 nm). Transmitted light and fluorescence overlay (C and F) of the portions marked in panels A and D. Cell contours are marked with a dashed line. Pixel size 62 × 62 nm; pixel dwell time 42 µs.*

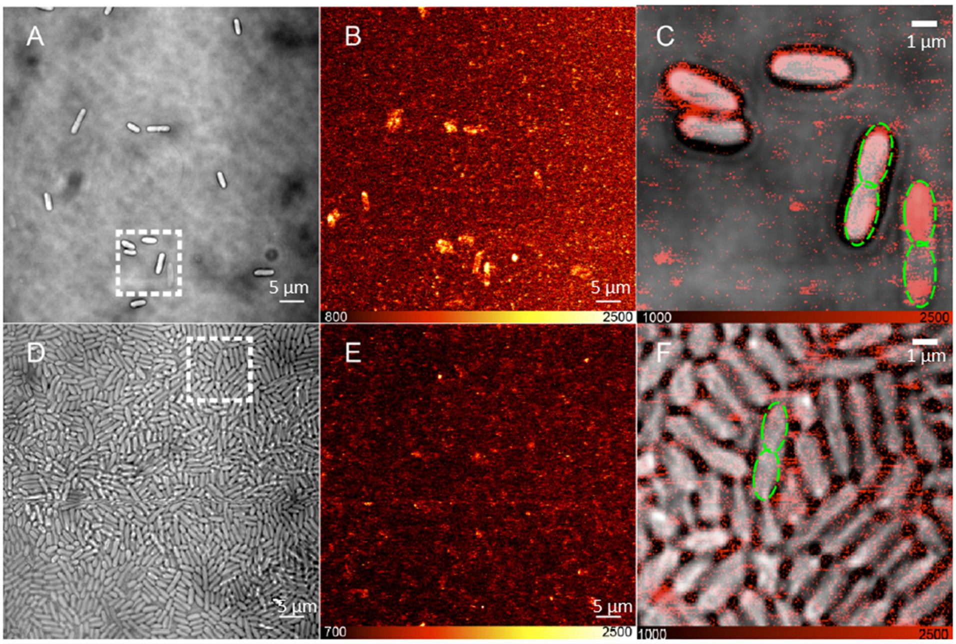

Fig. 4-28 *Comparison of selected images of E. coli incubated with 1 µM ZnMb (A-C) and E. coli incubated 1 µM ZnMb and washed by means of centrifugation. Images acquired with a confocal microscope using transmitted light (A and D) and confocal fluorescence (B and E) exploiting the emission of ZnMb (λ_{exc} = 561 nm, λ_{det} = 600−670 nm). Transmitted light and fluorescence overlay (C and F) of the portions marked in panels A and D. Cell contours are marked with a dashed line. Pixel size 62 × 62 nm; pixel dwell time 42 µs.*

FCS measurements provided further evidence for the spontaneous loading of ZnMb on bacterial cells. The fluorescence intensity time-traces measured for *E. coli* and *S. aureus* suspensions incubated with ZnMb (~1 μM) are characterized by several spikes, corresponding to low concentration (~nM), very slow diffusing species, that are reasonably identified with the bacteria decorated with several ZnMb proteins. An analysis of the fluorescence auto-correlation curves calculated from the time-trace where the spikes occurred, afforded an estimate of the diffusion coefficient of these species, that is D = (0.12 ± 0.02) $\mu m^2 s^{-1}$ for *E. coli* and D = (0.31 ± 0.05) $\mu m^2 s^{-1}$ for *S. aureus* suspensions (Tab. 4-5). The radius of the diffusing species is estimated from these values using the Stokes-Einstein equation for spherical particles that yielded a radius of ~2 μm and ~0.7 μm for *E. coli* and *S. aureus* respectively, roughly in agreement with the expected size of these cells . This must be considered as a rough estimate, particularly for *E. coli* cells, whose shape is rod-like and not spherical. The photo-physical parameters of ZnMb reported in Tab. 4-5 show that no relevant changes occur upon incubation with the cells, suggesting that the micro-environment of the photo-physically active molecule (Zn-PP IX) is substantially unaltered by the presence of the cells. Only a slight increase in the value of the triplet state lifetime τ_T is observed in the presence of *S. aureus*, from (26 ± 1) to (34 ± 3) μs. The larger value measured for τ_T may result from a reduced accessibility of O_2 to the protein cavity, possibly due to an interaction with the cell wall. The value of τ_T retrieved for ZnMb incubated with *E. coli* is (29 ± 3) μs, larger but still consistent with the one obtained in the absence of bacteria. The assignment of these transients to the ZnMb triplet state was confirmed by the increase of its lifetime upon removal of O_2 from samples (Tab. 4-5). It should be pointed out that a related porphyrin-based PS, Photofrin, was reported to show a considerably shorter triplet state lifetime (6 μs) when bound to *S. aureus*, which suggests that the Zn-PP IX remains bound to the protein structure in the presence of cells.

Fluorescence emission spectra and $^1O_2$ phosphorescence kinetics are reported in Fig. 4-29 for ZnMb in PBS solution and in incubated with *E. coli* and *S. aureus*. The results are similar for *S. aureus* (Fig. 4-29 A-B) and *E. coli* (Fig. 4-29 C-D) and show that both the ZnMb fluorescence emission spectra and the $^1O_2$ phosphorescence kinetics are substantially unaltered upon incubation with the cells (blue curves), with respect to the PBS solution (black curves). Thus, the ability of ZnMb to photosensitize $^1O_2$ appears to be unaltered by the presence of the cells. As for the measurements performed on the confocal microscope, additional experiments were carried out in which, after the incubation period with ZnMb, the samples are washed by mean of a mild centrifugation, removal of the supernatant and re-suspension of the pellet in an equal volume of fresh PBS buffer. No sizeable ZnMb fluorescence or $^1O_2$ phosphorescence emission can be detected for the washed samples (Fig. 4-29, red curves). This result confirms the conclusions derived from the images data, i.e. that the interaction between the protein-based PS and the bacterial cells is rather weak, so that the two species can be easily separated by centrifugation. Accordingly, the ZnMb fluorescence emission spectrum collected from the supernatant after the washing procedure, is almost indistinguishable from the one observed before centrifugation (Fig. 4-29 A, green curve), an indication that ZnMb dissociates from bacterial wall after the centrifugation.

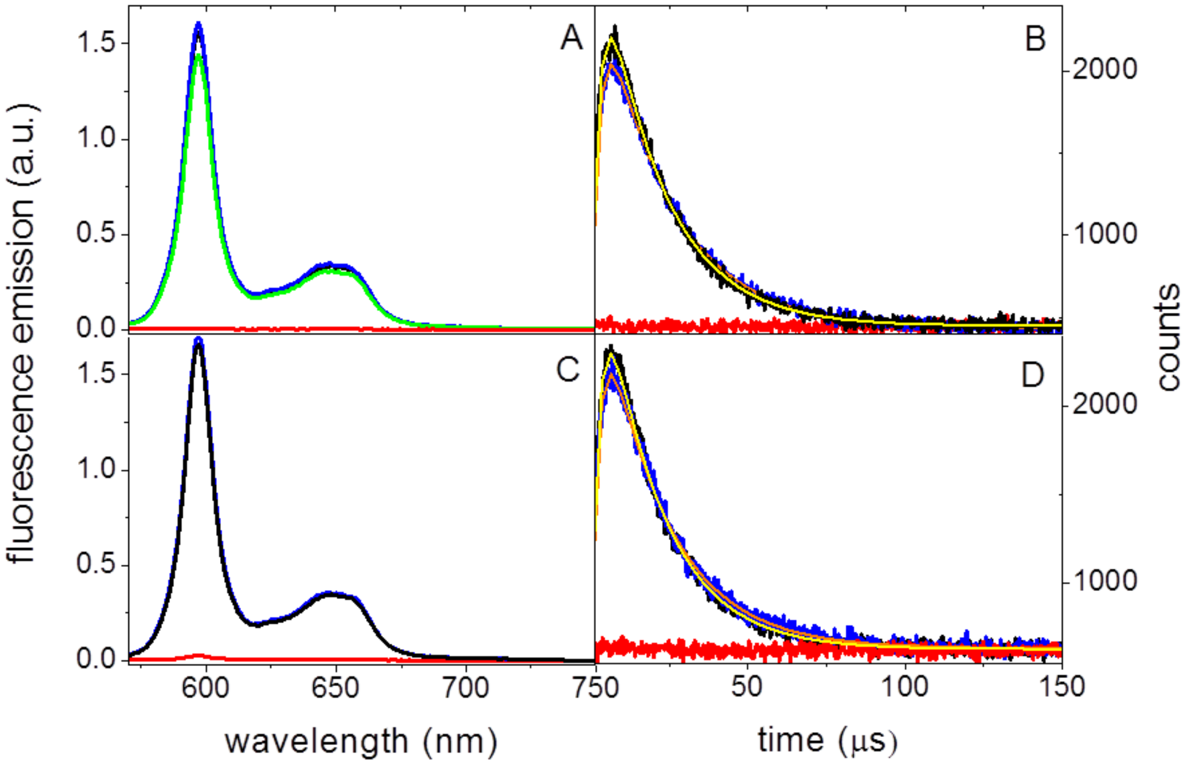

Fig. 4-29 *Comparison of fluorescence emission spectra (A and C) and time-resolved* $^1O_2$ *phosphorescence traces (B and D) for ZnMb in PBS buffer (black), ZnMb incubated with S. aureus (A and B, blue) or E. coli (C and D, blue) and ZnMb incubated with bacteria and washed (red). A fluorescence spectrum for the supernatant is reported in green in panel A. Fit curves for phosphorescence kinetics are reported for ZnMb in PBS (yellow) and ZnMb incubated with bacteria (orange). All samples are air-equilibrated at room temperature with [ZnMb] = 10 μM. Fluorescence spectra are collected with* λ_{exc} *= 552 nm. Phosphorescence kinetics are collected with* λ_{exc} *= 532 nm,* λ_{det} *= 1270 nm, resolution 256 ns, repetition rate 1 kHz for 10 min acquisition.*

4.2.2.2 Bacteria photo-inactivation

Photo-inactivation effect due to ZnMb were studied on *S. aureus* and *E. coli* at different doses of green light and for different concentrations of PS. The results are summarized in Fig. 4-30 where a substantial difference in the effects of the photo-treatment between the two bacterial types can be immediately recognized. *S. aureus* (Fig. 4-30 A-B) is efficiently photo-inactivated upon irradiation, that induces a reduction of the bacterial colony forming units up to 6 logarithmic units with respect to the dark value. Conversely, *E. coli* is not appreciably affected by the photosensitization treatment

(Fig. 4-30 C-D). As previously discussed for the apoMb-Hyp nanostructure, the different response of the two bacteria is attributable to the structure of their cell wall. The thicker and less permeable wall of the Gram-negative *E. coli* is likely able to protect the bacterium from a lethal photo-oxidative damage of $^1O_2$ that is generated on the surface of the cell, where ZnMb localizes. Thus, despite the comparable accumulation of ZnMb on both cell types, only the Gram-positive *S. aureus* are substantially killed in the photosensitization-based treatment, in agreement with the results obtained with apoMb-Hyp and with the reported observation that Gram-negative bacteria are much better inactivated by small cationic PSs, able to localize on the sensitive inner cell membrane [14]. Thus, ZnMb shows a good potential as protein-based PS only for the inactivation of Gram-positive bacteria. An effective photo-killing of *S. aureus* in suspension is indeed observed for 3 µM ZnMb at a light dose of 18 J cm^{-2}, that is already enough for inducing a 3 logarithmic units decrease in the number of colony forming units. As can be appreciated in Fig. 4-30 B, the most efficient condition for the bacterial photo-killing are achieved for 20 µM ZnMb with a light dose of 37 J cm^{-2}, which reduced the population of colony forming units by 6 logs, without appreciable dark toxicity. If the ZnMb concentration is increased to 50 µM, some dark toxicity is induced and a less efficient photo-inactivation of the bacteria is observed, particularly for the lower light dose of 18 J cm^{-2} (Fig. 4-30 A). This effect is attributed to a screening (inner filter) effect due to the intense absorption from the PS in solution, as already reported for other systems with high PS concentrations [15]. Additionally, it should be pointed out that the green light that is used for the photo-inactivation is not optimally absorbed by the ZnMb. A higher efficiency can possibly occur for a photo-excitation on the main absorption bands of the PS.

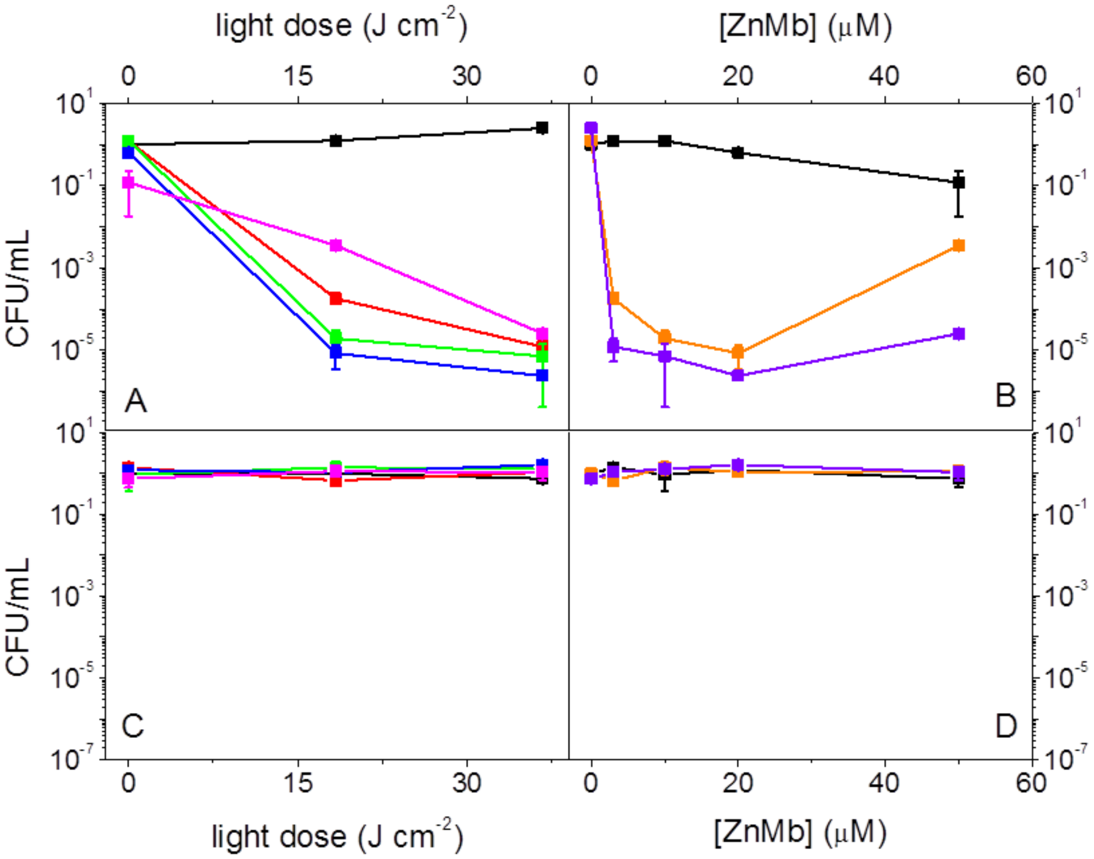

Fig. 4-30 *Light (18 and 37 J cm*$^{-2}$*, at 520 nm) effect on S. aureus (A) and E. coli (C) photo-inactivation by ZnMb 3 µM (red), 10 µM (green), 20 µM (blue), 50 µM (magenta). Control experiments were performed without ZnMb (black). ZnMb concentration effect on S. aureus (B) and E. coli (D) is shown at 18 J cm*$^{-2}$ *(orange) and 37 J cm*$^{-2}$ *(violet) light doses (at 520 nm). Control experiments are performed in the dark (black).*

4.2.3 Perspective of application for food decontamination

From the point of view of applications, it is particularly interesting that ZnMb spontaneously forms during the maturation of nitrate/nitrite-free dry-cured hams, where its presence is related to the preservation of the red color of the meat [16 17 18 19]. Since these products are not cooked and additive-free they are likely exposed to bacterial contamination. As we demonstrated above, the ZnMb has a potential as built-in PS, that can be exploited as antimicrobial agent for such hams against Gram-positive bacteria, avoiding the introduction of exogenous products. Our results show that a consistent efficacy on *S. aureus* in suspension is already appreciated for the lowest concentration (3 µM) of ZnMb tested (inducing 4 to 5 log units decrease in the number of CFU), that is comparable with the ZnMb content estimated in ham, ranging between 1.6 and 2.8 µM [20]. This is particularly interesting since a minimal effect of the quality of the product is one of the most important requirements for a photosensitization-based food decontamination. Further studies carried out directly on bacteria grown in the ham environment will be necessary to evaluate the real efficiency of ZnMb for these treatments.

4.2.4 Preliminary results on tumor cells

Beside antimicrobial applications, ZnMb has interesting possibility also for tumor cells photosensitization treatments. The above results for the use of a protein-based carrier based on apoMb for the PS Hyp show indeed good results on tumor cells in suspension, suggesting that the protein carrier may promote the efficiency of the photo-treatment. However, a difficult issue to address for the investigation of these systems is to determine whether the PS remains bound to the protein-based carrier in a real biosystem. Indeed, the relatively low affinity of the PS for the protein-based carrier may allow a dispersion of the PS and a loose of selectivity. Thus, the fact that a dissociation of the PS cofactor from the protein-based carrier is unlikely to occur for ZnMb, can be considered an advantage over the apoMb-Hyp nanostructure. Additionally, an enhanced selectivity for some tumor cell types can in principle by achieved by the realization chimeric constructs where the protein-based portion of ZnMb is functionalized with a specific peptide chain specifically recognized by target cells. Some preliminary experiments have been carried out for ZnMb incubated with HeLa and PC3 tumor cells in suspensions, where the distribution of the protein-based PS is revealed by mean of a confocal microscope (Fig. 4-31, 4-33). A concentrated solution of ZnMb is administrated to the cells so that the final concentration is 10 μM, and images are collected in time (every 12 s) allowing to monitor the localization of the PS. Also the effect of the photosensitization on the cell structure are revealed, induced directly by the excitation beam of the microscope, without need for other specific light sources. Given the faint fluorescence and the rapid photo-bleaching of the PS, together with the presence of a rather intense autofluorescence from the cells, an high concentration of ZnMb 10 μM is used in these preliminary experiments.

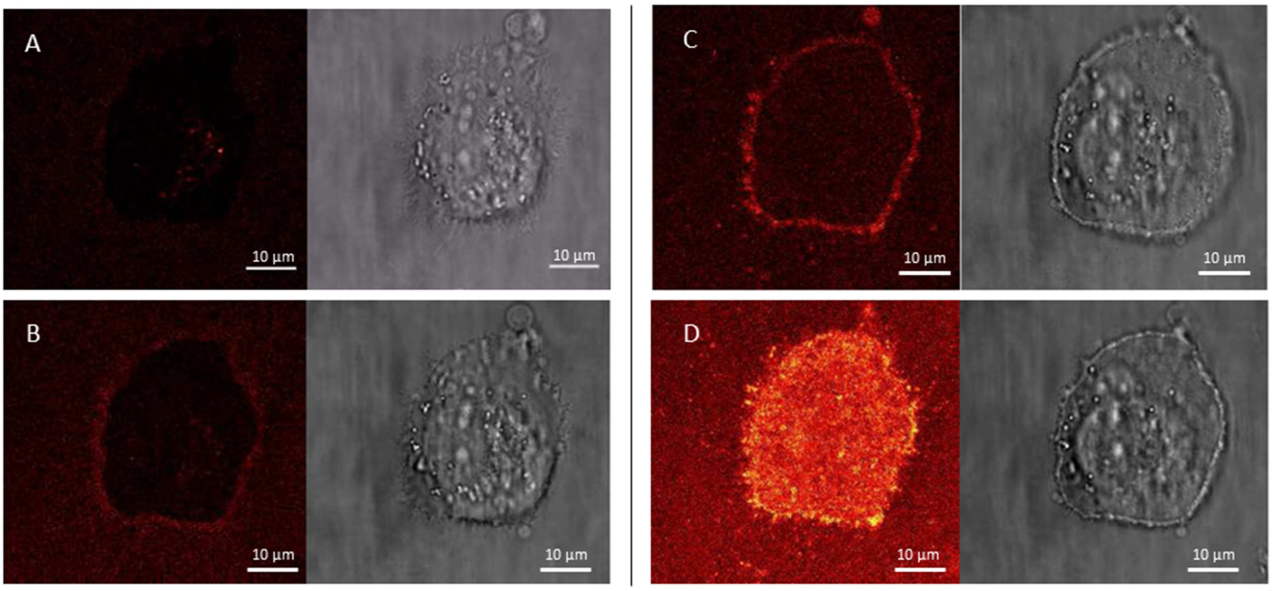

Fig. 4-31 *Selected images acquired with a confocal microscope (on the left panels) and in transmitted light mode (on the right panels) for PC3 cells with 10 µM ZnMb at 0 min (A), 6 min (B), 27 min (C) and 60 min (D) after the administration of the PS.* λ_{exc} *= 561 nm,* λ_{det} *= 570-650 nm, dwell time = 42 µs, contrast is the same for all images.*

Some selected images are reported in Fig. 4-31 for ZnMb incubated with PC3 cells, where it is possible to notice that within few minutes after the administration, the PS is mainly accumulated on the plasma membrane of the cells (Fig. 4-31 B), whose profile showed by the transmitted light image appears rather irregular and may indicate that the cell is suffering from a photo-damage. Nearly no fluorescence emitted from ZnMb can be detected inside the cells for the first minutes, indicating that internalization is negligible. As indicated by comparison with Fig. 4-32, where images are collected in absence of ZnMb, the emission observed inside the cell on the shorter time scale (Fig. 4-31 A and 4-32 A) arise from an autofluorescence of some cellular components. After ~30 min irradiation (Fig. 4-31 C), a fluorescence emission becomes appreciable also from the internal part of the cells, indicating that the membrane permeability is increased allowing ZnMb to penetrate into the cytoplasmic region. As reported in Fig. 4-31 D, after 60 min irradiation, an intense fluorescence is emitted by the whole cell structure, indicating the ZnMb induced an extensive photo-damage of several cellular components resulting in the necrotic death of the cell.

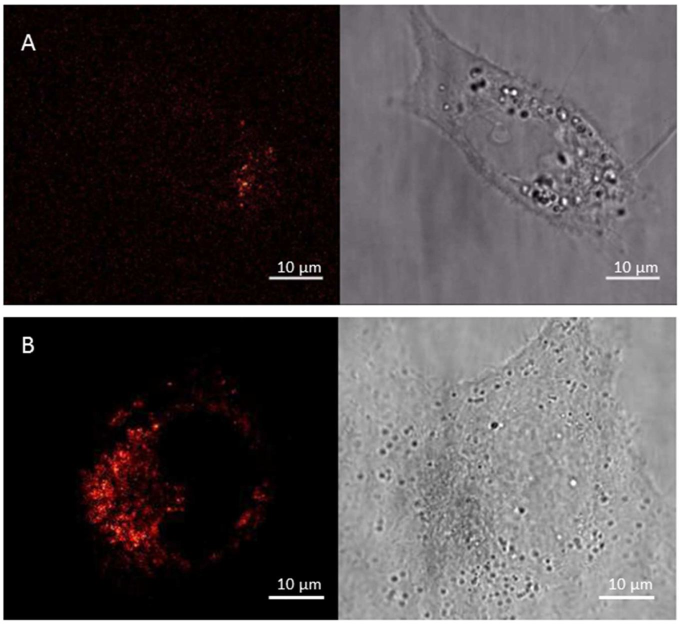

Fig. 4-32 *Control images acquired with a confocal microscope (left panel) and in transmitted light mode (right panel) for PC3 cells without PS at an initial time (A) and after 60 min (B).* λ_{exc} *= 561 nm;* λ_{det}*= 570-650 nm, dwell time= 42 µs.*

Fig. 4-33 reports some images of HeLa cells collected at selected delays after the administration of ZnMb. The profile on these cells appears rather irregular and a rather intense autofluorescence is observed from inside the cell, as showed in Fig. 4-34 where images are reported for HeLa cells in the absence of ZnMb. Within a minute, a slight increase in fluorescence emission appears on the region corresponding to the plasma membrane, likely indicating an accumulation of the PS on the cells. However, the effect does not appear as clear as the one observed for PC3 cells, and the signal arising from the ZnMb interacting with the cell is hardly distinguishable from the autofluorescence. Transmitted light images show that the cell undergoes structural changes that are appreciable after 4 min irradiation (Fig. 4-33 C) indicating the cell is suffering. However, these changes are not clearly correlated with a variation in the localization of the fluorescence emission.

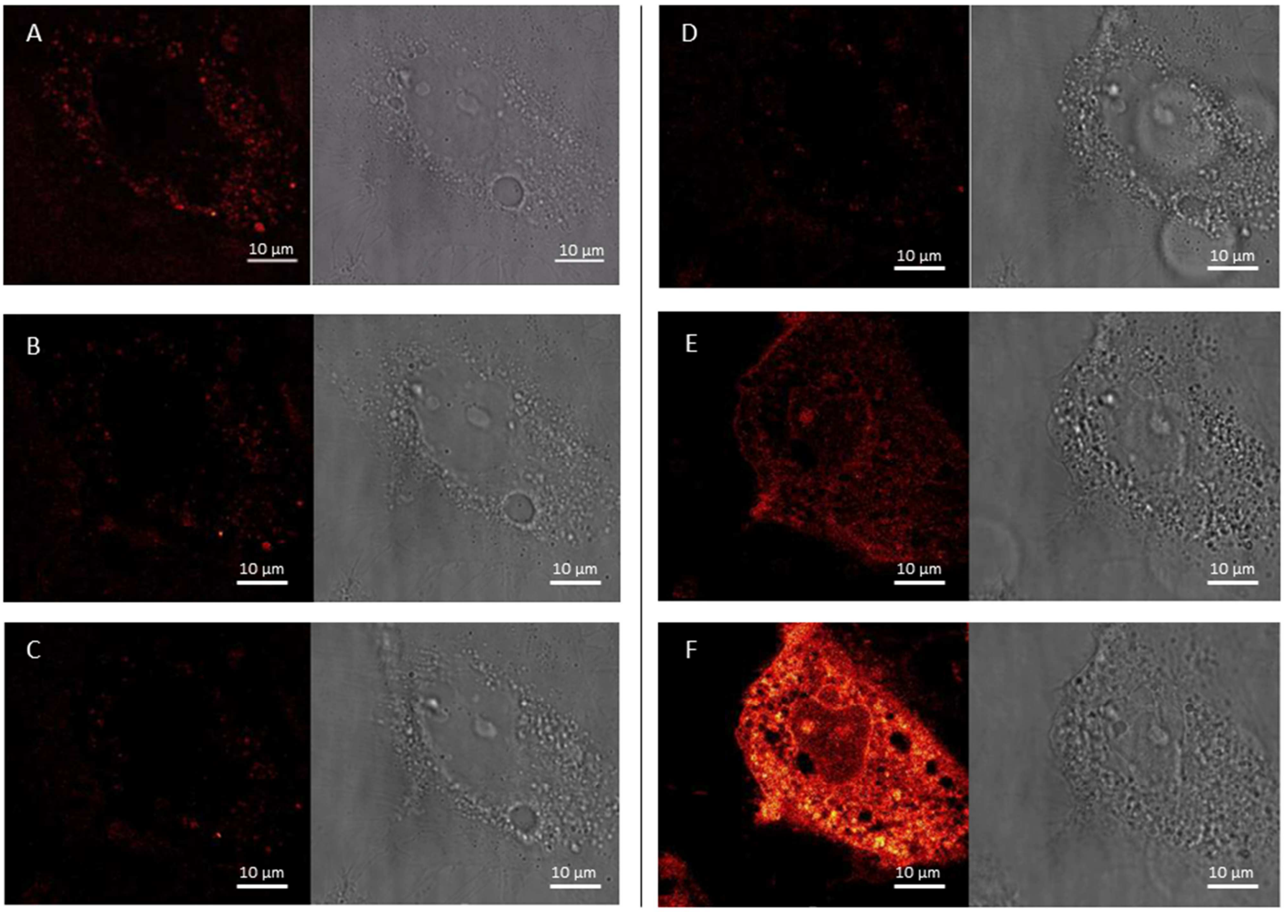

Fig. 4-33 *Selected images acquired with a confocal microscope (on the left panels) and in transmitted light mode (on the right panels) for HeLa cells with 10 µM ZnMb at 0 min (A), 3 min (B), 4 min (C), 8 min (D), 30 min (E) and 60 min (F) after the administration of the PS.* λ_{exc} *= 561 nm,* λ_{det}*= 570-650 nm, dwell time = 42 µs, contrast is the same for all images.*

Only after 30 min irradiation (Fig. 4-33 E) an intense fluorescence appears inside the cell, indicating that the plasma membrane is permeable allowing the ZnMb to accumulate on the internal cellular structures. At the same delay, a damaged cellular structure is evident from the transmitted light images. The fluorescence intensity from ZnMb is even higher in Fig. 4-33 F, where even the internal components appear heavily damaged, clearly indicating a necrosis.

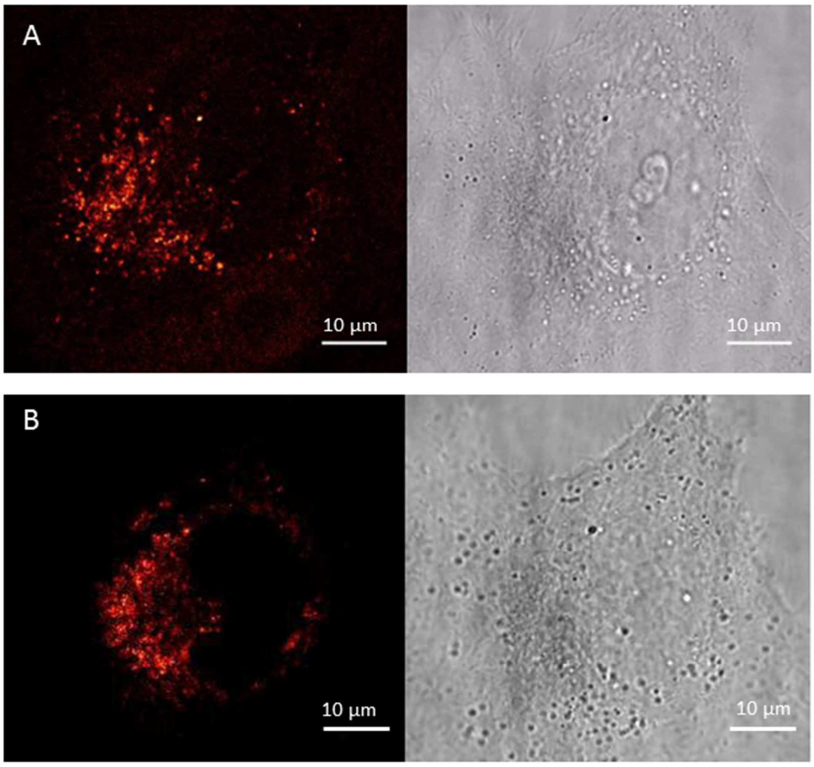

Fig. 4-34 *Control images acquired with a confocal microscope (left panel) and in transmitted light mode (right panel) for HeLa cells without PS at an initial time (A) and after 60 min (B).* λ_{exc} *= 561 nm;* λ_{det} *= 570-650 nm, dwell time = 42 µs.*

Further studies performed with lower concentrations of PS and in more controlled conditions preserving cell viability will elucidate the effects of photo-damage induced by ZnMb on these cells. These preliminary results show an accumulation of the protein-based PS on the plasma membrane that appears to induce a necrotic cell death. Interestingly, ZnMb appears to have a spontaneous faster accumulation on PC3 than on HeLa, possibly due to the presence of specific interactions with some cellular components.

4.2.5 Chapter bibliography

1. Comas-Barceló, J. *et al.* A self-assembled nanostructured material with photosensitising properties. *RSC Adv.* **3,** 17874 (2013).
2. Miškovský, P., Jancura, D., Sánchez-Cortés, S., Kočišová, E. & Chinsky, L. Antiretrovirally Active Drug Hypericin Binds the IIA Subdomain of Human Serum Albumin: Resonance Raman and Surface-Enhanced Raman Spectroscopy Study. *J. Am. Chem. Soc.* **120,** 6374–6379 (1998).
3. Jimenez-Banzo, A. *et al.* Singlet oxygen photosensitisation by GFP mutants: oxygen accessibility to the chromophore. *Photochem. Photobiol. Sci.* **9,** 1336–1341 (2010).
4. Jiménez-Banzo, A., Nonell, S., Hofkens, J. & Flors, C. Singlet Oxygen Photosensitization by EGFP and its Chromophore HBDI. *Biophys. J.* **94,** 168–172 (2008).
5. Bulina, M. E. *et al.* A genetically encoded photosensitizer. *Nat Biotech* **24,** 95–99 (2006).
6. Vegh, R. B. *et al.* Reactive oxygen species in photochemistry of the red fluorescent protein 'Killer Red'. *Chem. Commun.* **47,** 4887–4889 (2011).
7. Ruiz-González, R. *et al.* Singlet Oxygen Generation by the Genetically Encoded Tag miniSOG. *J. Am. Chem. Soc.* **135,** 9564–9567 (2013).
8. Pimenta, F. M., Jensen, R. L., Breitenbach, T., Etzerodt, M. & Ogilby, P. R. Oxygen-Dependent Photochemistry and Photophysics of 'MiniSOG,' a Protein-Encased Flavin. *Photochem. Photobiol.* **89,** 1116–1126 (2013).
9. Lepeshkevich, S. V *et al.* Photosensitized Singlet Oxygen Luminescence from the Protein Matrix of Zn-Substituted Myoglobin. *J. Phys. Chem. A* **118,** 1864–1878 (2014).
10. Zemel, H. & Hoffman, B. M. Long-range triplet-triplet energy transfer within metal-substituted hemoglobins. *J. Am. Chem. Soc.* **103,** 1192–1201 (1981).
11. Nonell, S. & Braslavsky, S. E. in *Singlet Oxygen, UV-A, and Ozone* (ed. Lester Packer, H. S. B. T.-M. in E.) **Volume 319,** 37–49 (Academic Press, 2000).
12. Rodríguez-Amigo, B. *et al.* The complex of hypericin with β-lactoglobulin has antimicrobial activity with potential applications in dairy industry. *J. Dairy Sci.* **98,** 89–94 (2015).
13. Delcanale, P. *et al.* Subdiffraction localization of a nanostructured photosensitizer in bacterial cells. *Sci. Rep.* **5,** 15564 (2015).
14. Sperandio, F. F., Huang, Y.-Y. & Hamblin, M. R. Antimicrobial Photodynamic Therapy to Kill Gram-negative Bacteria. *Recent Pat Antiinfect Drug Discov* **8,** 1–23 (2013).
15. Demidova, T. N. & Hamblin, M. R. Photodynamic Inactivation of Bacillus Spores, Mediated by Phenothiazinium Dyes. *Appl. Environ. Microbiol.* **71,** 6918–6925 (2005).
16. Adamsen, C., Møller, J. S., Hismani, R. & Skibsted, L. Thermal and photochemical degradation of myoglobin pigments in relation to colour stability of sliced dry-cured Parma ham and sliced dry-cured ham produced with nitrite salt. *Eur. Food Res. Technol.* **218,** 403–409 (2004).
17. Adamsen, C. E., Møller, J. K. S., Laursen, K., Olsen, K. & Skibsted, L. H. Zn-porphyrin formation in cured meat products: Effect of added salt and nitrite. *Meat Sci.* **72,** 672–679 (2006).
18. Wakamatsu, J. *et al.* Formation of zinc protoporphyrin IX in Parma-like ham without nitrate or nitrite. *Anim. Sci. J.* **80,** 198–205 (2009).
19. Parolari, G., Benedini, R. & Toscani, T. Color Formation in Nitrite-Free Dried Hams as Related to Zn-

Protoporphyrin IX and Zn-Chelatase Activity. *J. Food Sci.* **74,** C413–C418 (2009).

20. Wakamatsu, J., Odagiri, H., Nishimura, T. & Hattori, A. Quantitative determination of Zn protoporphyrin IX, heme and protoporphyrin IX in Parma ham by HPLC. *Meat Sci.* **82,** 139–142 (2009).

4.3 Nanostructures based on lipocalins: βLG and Hyp

As demonstrated in Section 4.1, protein-based nanostructures for the delivery of Hyp as photo-physically active molecule self-assemble in aqueous solutions taking advantage of simple hydrophobic effect. One nanostructure realized in this work, is based on a protein belonging to the lipocalin family, i.e. βLG, having a completely different fold than the above described globin-based nanostructures. The hydrophobic cavity of the monomeric βLG is able to accommodate linear hydrophobic molecules but it is sterically not suitable for the binding of Hyp. However, βLG spontaneously forms dimers at the concentrations found in its biological environment [1] [2] and the dimeric form of the protein is able to bind Hyp at different binding sites [3]. Unlike apoMb-Hyp, the self-assembly of the βLG-based nanostructure in aqueous solution results from multiple association equilibria governing the protein dimerization and the binding of the Hyp at different binding sites. The interest concerning this system relies on the fact that βLG is the most abundant protein of bovine milk whey [4], and thus the realization of a βLG-based nanostructure for the transport of the PS Hyp potentially constitute a highly bio-compatible system for a sanitizer-free antimicrobial decontamination, exploitable in the dairy industry.

4.3.1 2βLG-Hyp: a stable nanostructure

βLG structure is shaped to accommodate small linear hydrophobic compounds, such as retinol or the hydrophobic chains of fatty acids inside the β-barrel folding typical of the lipocalin family. The monomer's internal cavity is too narrow to accommodate the Hyp molecule. However, βLG undergoes spontaneous dimerization under biologically relevant conditions [1]. The dimerization is associated with the antiparallel alignment of two β-strand (residues 163-167) and with the formation of H-bond between them. The interface between the monomers is also shaped by the AB and CD loops, where residues Arg49 and Arg66 partecipate in a salt bridge. Inspection of the dimeric structure of βLG (2βLG) reveals that the Hyp might bind two hydrophobic clefts formed at the interface between the monomers. A narrow cleft is formed at the bottom of the β-barrel and it extends along the surface of helix 4 (residues 146-156) and β-strand (residues 163-167). The wide cleft is located at the interface of two helices (residues 45-48 and 169-173) and the loops AB and CD, which contains Trp77. Fig. 4-35 reports the best-poses resulting from a docking simulation showing that Hyp binds with a relatively large affinity to the narrow cleft (binding free energy estimated from the simulation: -7.4 kcal mol^{-1}) where the Hyp appears tightly inserted between the walls of the cavity and rather shielded from the solvent. Conversely, the binding at the larger cleft of 2βLG occurs with a lower affinity (binding free energy estimated from the simulation: -4.9 kcal mol^{-1}) and one face of the Hyp molecules appears to remain exposed to the solvent (Fig. 4-35).

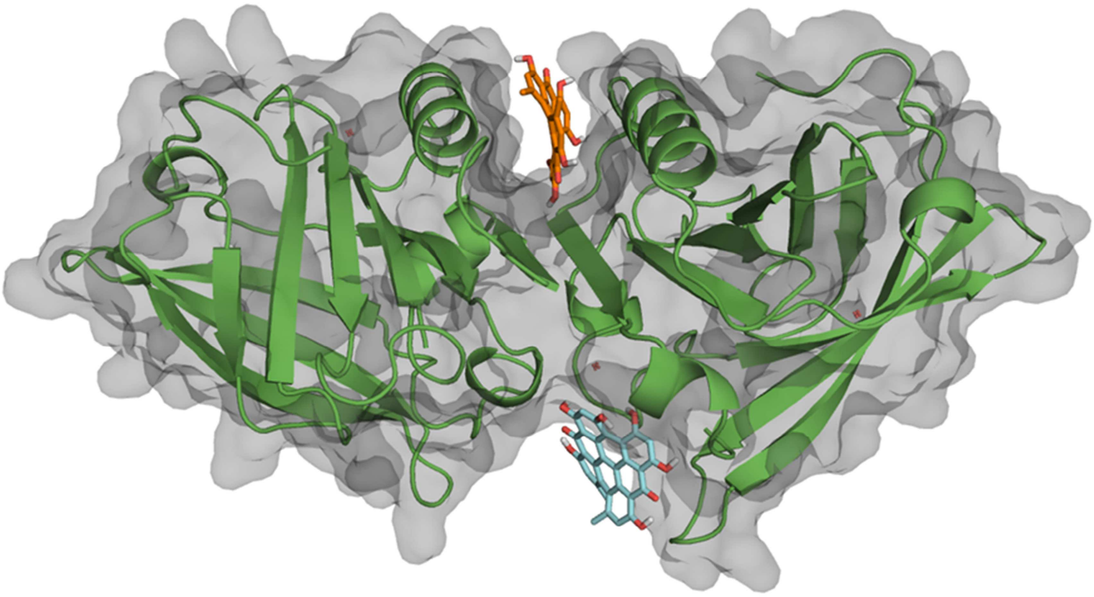

Fig. 4-35 *Best poses of Hyp bound to the narrow and wide clefts obtained from docking calculations. Hyp is shown as sticks (orange and blue in the forms bound to the narrow and wide clefts, respectively). The backbone of the dimeric species of βLG is shown in green, and the grey area displays the surface of the dimer.*

Binding of Hyp to the narrow cleft is also stabilized by hydrogen bonds between the PS's hydroxyl groups and backbone carbonyl groups (Lys157, Leu159 and Met161) and the side chains of Asp153 and Glu159. Additionally, three independent MD simulations (data not shown) were run to examine the structural integrity of Hyp bound to the narrow cleft of 2βLG. In all cases the best docked pose was used as the starting structure. The analysis of the trajectories confirms that Hyp remains bound to this cleft but showing slightly distinct arrangements within the pocket, suggesting the lack of specific, strong interactions with the protein and that hydrophobicity is the main factor in determining the binding to the narrower site.

As previously discussed for the binding of Hyp to apoMb, the occurring of an interaction leading to the formation of a self-assembled nanostructure between 2βLG and Hyp in aqueous PBS buffer can be monitored spectroscopically by following the changes in the photo-physical properties of Hyp. While the aggregation of Hyp in simple PBS buffer produces broad and poorly defined absorption bands and a barely detectable fluorescence emission, when βLG is added Hyp partially recovers spectral features resembling those observed for monomeric Hyp dissolved in DMSO, i.e. sharper absorption bands and a more intense and structured fluorescence emission (Fig. 4-36 A-B). This indicates that a fraction of Hyp is likely monomeric and is embedded in less polar environment than water, that results from the binding of the PS at the hydrophobic cavities of the protein structure.

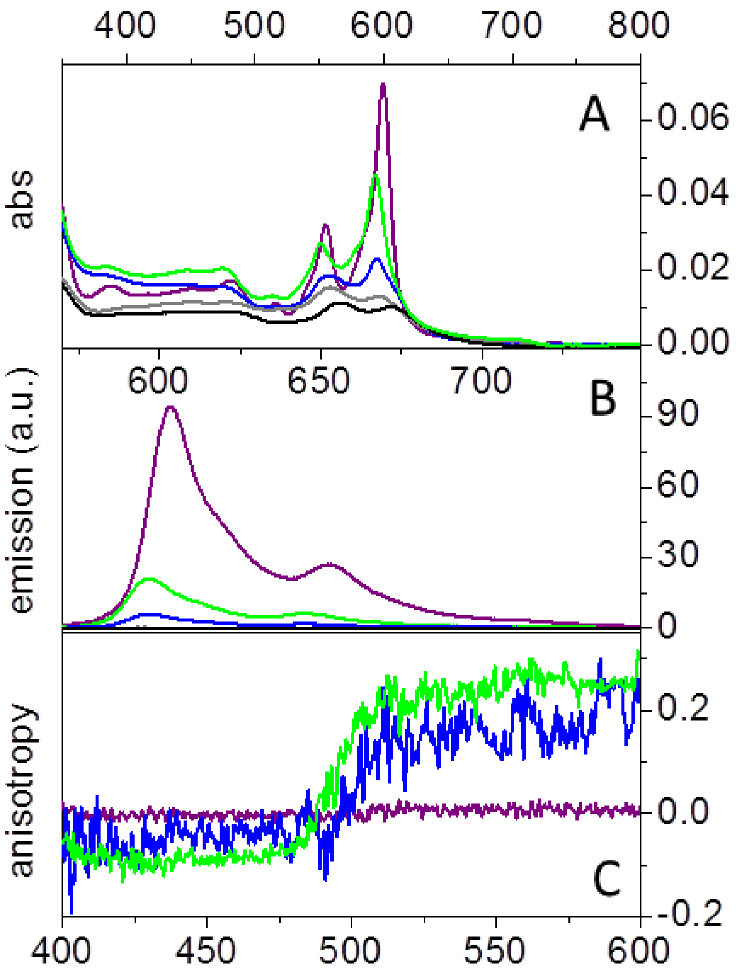

Fig. 4-36 Absorption (A), fluorescence emission (B) and fluorescence anisotropy (C) spectra of Hyp in DMSO (purple), Hyp in PBS (black), Hyp in PBS-DMSO 20% (grey), 2βLG-Hyp in PBS (blue) and 2βLG-Hyp in PBS-DMSO 20% (green). Hyp concentration is 4 μM and βLG, where present, is 200 μM. Emission spectra: λ_{exc} = 554 nm, T = 20°C. Fluorescence anisotropy spectra are obtained from excitation spectra (λ_{em}= 620 nm, T = 20°C).

A proof of the interaction between Hyp and the dimeric protein structure 2βLG is given by fluorescence anisotropy and is reported in Fig. 4-36 C. Non zero anisotropy values are found for 4 μM Hyp placed in a PBS solution with 200 μM βLG, corresponding to a substantial 2βLG concentration of ~86 μM, calculated using the dimerization constant reported by Mercadante at.[1] under similar experimental conditions. This result indicates that the rotational diffusion of the fluorophore is considerably slower with respect to the one of Hyp dissolved in DMSO, that yields zero anisotropy (Fig. 4-36 C, purple curve), consistently with the formation of a complex between 2βLG and Hyp where the rotation of the fluorophore is limited by the presence of the protein matrix. As described for the case of Hyp bound to apoMb, FCS provides additional proof for the formation of a stable nanostructure between 2βLG and Hyp. The fluorescence auto-correlation curve obtained for 1 nM Hyp in the presence of an excess of βLG (30 μM), is well fitted by a model comprising diffusional motion on the 10 μs – 1 ms time scale and the formation of a dark triplet state decaying on the 1 μs – 10 μs time scale (Fig. 4-37 A). The value for the diffusion coefficient retrieved for the dominant diffusing species is D = 70 $\mu m^2 s^{-1}$, that is consistent with the one expected for Hyp bound to 2βLG.

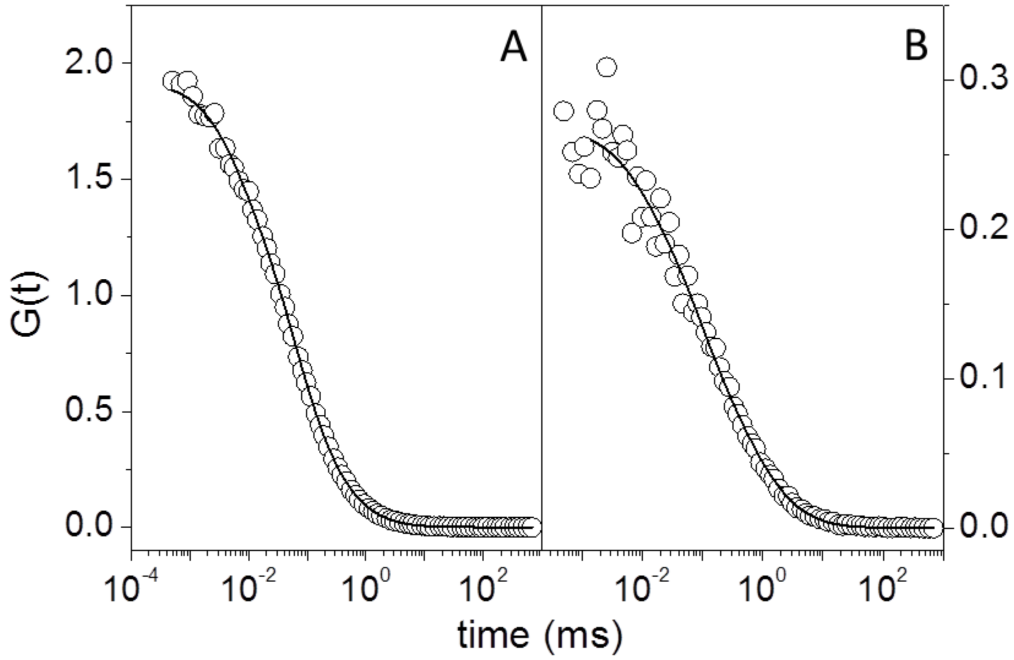

Fig. 4-37 *Fluorescence auto-correlation curves obtained for 1 nM Hyp in PBS buffer in the presence of 30 μM βLG (A – open circles) and 10 nM Hyp in the mixture PBS-DMSO in the presence of 36 μM βLG (B – open circles). The black lines are the results of the fit with a model comprising a triplet state decay and molecular diffusion.* λ_{exc} *= 475 nm,* λ_{det} *= 670 nm.*

The main photo-physical parameters measured for Hyp bound to 2βLG (2βLG-Hyp) are summarized in Tab. 4-6, where it can be appreciated that the value of τ_T is in air-equilibrated PBS buffer solutions is in the order of ~10 μs. As previously discussed for apoMb-Hyp, this value is longer than the one expected for PSs dissolved in air-equilibrated aqueous solutions, indicating a partial shielding of the molecule from the solvent, owed to the interaction with the protein scaffold [5]. Moreover, the analysis of the fluorescence decay for 2βLG-Hyp in PBS solution reports a bi-exponential trend characterized by lifetimes corresponding to 3.9 ns (35%) and 6.7 ns (65%) (Tab. 4-6). This result can be nicely interpreted with the presence of two populations of Hyp, that likely correspond Hyp bound at the two binding sites on 2βLG. The major emission component can be attributed to Hyp bound in the narrow site of 2βLG, where the PS is well shielded from the solvent and embedded in a less polar than water environment, and it is thus characterized by a relatively long emission lifetime of 6.7 ns, even longer than the one observed for Hyp in DMSO (Tab. 4-6).

The minor component can be attributed to Hyp bound at the larger cleft of 2βLG, where the molecule is partially exposed to the solvent and possibly staked to other Hyp, and it is thus characterized by a faster emission lifetime of 3.9 ns (Tab. 4-6).

sample	solvent	τ_F (ns)	Φ_F	τ_T (μs)	Φ_T	τ_Δ (μs)	Φ_Δ
Hyp	DMSO	5.5±0.1 (100%)	0.35±0.02 [6]	1.4±0.1*	0.35 [7]	5.5±0.1	0.28±0.05 [8]
2βLG-Hyp	PBS	3.9 (35%) 6.7 (65%)	0.03±0.01	9.7±2.4* 8.6 [&] 9.6 [£]	0.050±0.002	2.3	0.065±0.010
2βLG-Hyp	PBS-DMSO 20%	0.2 (20%) 5.6 (80%)	0.064±0.008	8.2±0.4* 8.4 [&] 7.5 [£]	0.170±0.002	2.5	0.123

Tab. 4-6 *Photo-physical parameters of Hyp *: LFP; [&]:NIR phosphorescence detection; [£]:FCS.*

Since virtually only bound Hyp molecules are fluorescent, the fluorescence emission intensity is proportional to the fraction of bound molecules, and an estimate of the affinity of Hyp for 2βLG can be obtained by monitoring the fluorescence emission as a function of the Hyp concentration, in the presence of a fixed amount of 2βLG. The obtained isotherm binding curve (Fig. 4-38) is described by a simplified model taking into account only one binding equilibrium: 2βLG + Hyp ⇄ 2βLG-Hyp. The model is similar to the one described for the binding of Hyp to apoMb, with the difference that, in this case, the amount of protein is kept constant while the Hyp concentration changes. This allows a simplified analysis since the equilibrium relative to the protein dimerization can be neglected. The apparent association constant retrieved is $K_a = (1.40 \pm 0.07)\ \mu M^{-1}$, corresponding to a dissociation constant $K_d = (0.71 \pm 0.03)\ \mu M$.

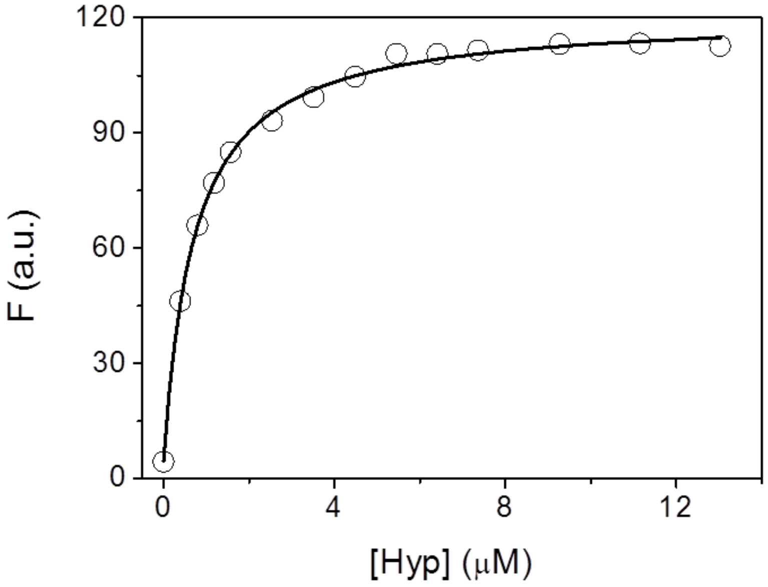

Fig. 4-38 *Integrated fluorescence emission intensity (circles) as a function of Hyp concentration at [βLG] = 100 μM, corresponding to [2βLG] ≈ 40 μM. The black line is the result of the fit with a model considering one binding equilibrium.*

These results demonstrate that a stable and water soluble nanostructure spontaneously forms between Hyp and 2βLG, that actually acts as bio-compatible carrier for the photo-active molecule under biologically relevant conditions.

4.3.2 2βLG-Hyp: a photo-functional system

The potential of the 2βLG-Hyp nanostructure as photosensitizing agent is determined by the ability of the protein-bound PS to be excited to its triplet state and then photosensitize the production of $^1O_2$. The quantum yield for the triplet state formation (Φ_T) of Hyp bound to 2βLG, photo-excited with a 532 nm laser pulse, is estimated with a LFP experiment by comparing the intensity of the 2βLG-Hyp transient absorption signal at 520-515 nm to the one of Hyp in DMSO, that was taken as a reference. The value for the Φ_Δ is estimated by directly monitoring the time-resolved $^1O_2$ phosphorescence emission due to 2βLG-Hyp in comparison with some reference PSs (see 3.7). Interestingly, the values retrieved for 2βLG-Hyp in PBS buffer, Φ_T = (0.050 ± 0.002) and Φ_Δ = (0.065 ± 0.010) (Tab. 4-6), are fairly similar indicating that the energy transfer process between the O_2 and the triplet state of Hyp leading to the photosensitization of $^1O_2$, occurs with a quantum yield close to unity. However, the value obtained for Φ_T, Φ_F and Φ_Δ relative to 2βLG-Hyp in PBS buffer are considerably lower (about one order of magnitude) when compared with the values of Hyp in DMSO [8] or with those of apoMb-Hyp (for which Φ_Δ = (0.14 ± 0.03)) [5]. These relatively low values, which appear modest when compared to similar systems, suggest that the excited state of the Hyp molecules bound to the protein-based structure may be partially quenched. The reduced fraction of active PS might be due to the binding of Hyp at the wider cleft of 2βLG, where the PS possibly remains partially aggregated, and where it is stacked against the residue of Trp77. Additionally, the Hyp bound at the wider cleft are partially exposed to the aqueous solvent, which may have a detrimental effect on the photo-physics of the PS [3].

4.3.3 Tuning the solvation at carrier's surface: improvement of the photo-functional properties

To enhance the photo-physical activity of Hyp bound to 2βLG we have taken advantage of the preferential interaction between the protein and the organic solvent DMSO. The peculiar solvation properties of this protein allow DMSO to coat 2βLG without appreciably affect the protein structure, up to an organic solvent concentration of ~50% [9]. We have thus introduced a small amount of DMSO as co-solvent, in order to provide a better environment to the protein-bound Hyp, thus increasing the fraction of photo-physically active molecules. A DMSO concentration of 20% (V_{DMSO}/V_{PBS}), corresponding to ~17% (V_{DMSO}/V_{TOT}) was selected, well below the value at which protein denaturation occurs. The formation of a stable self-assembled nanostructure between 2βLG and Hyp in the binary mixture of PBS and DMSO is confirmed by steady state fluorescence anisotropy and FCS measurements, which yield similar results to the case of 2βLG-Hyp formed in a pure PBS solution. Indeed, the anisotropy spectrum reported in green in Fig. 4-36 C shows non-zero values, consistent with those observed for the complex in pure PBS buffer (Fig. 4-36 C, blue), with an improved signal-to-noise ratio. The fluorescence auto-correlation curve obtained for 10 nM Hyp and 36 μM βLG in the binary mixture of PBS and DMSO, is well-fitted by a model comprising molecular diffusion and triplet state decay (Fig. 4-37 B). The diffusion coefficient retrieved for the dominant diffusing species is $D = 40\ \mu m^2\ s^{-1}$ and is roughly consistent with the value expected for the 2βLG-Hyp complex under these conditions. The lower value of D obtained in the PBS-DMSO mixture with respect to the one observed in pure PBS buffer indicates a slower diffusion that arises from the higher viscosity of the mixture and from the different hydrodynamic radius of the DMSO-coated protein structure [10] [11].

The presence of DMSO has a major effect on the spectroscopic properties of the 2βLG-Hyp nanostructure. In the PBS-DMSO mixture, the absorption spectrum is more structured than in pure PBS buffer (Fig. 4-36 A, green), with absorption bands more closely resembling those observed in pure DMSO (Fig. 4-26 A, purple). The intensity of the fluorescence emission (Fig. 4-36 B, green) also increases with respect to the one obtained in pure buffer. Moreover, the values for Φ_T, Φ_F and Φ_Δ reported for 2βLG-Hyp in the presence of DMSO are approximatively increased by a factor two when compared to those reported in pure PBS (Tab. 4-6), and become comparable to those measured for apoMb-Hyp [8]. The similar increase of these values indicates the presence of a larger fraction of better solvated Hyp molecules bound to the protein, which leads to an increase of the observed fluorescence emission, triplet state formation rate and photosensitization, with an efficiency of the energy transfer that is close to the unity. This interpretation is consistent with the values obtained from the analysis of the fluorescence decay for 2βLG-Hyp in the mixture PBS-DMSO. The fitting with a bi-exponential model reports a minor component having a sub-resolution lifetime due to scattering and a major component characterized by a lifetime of 5.6 ns, that closely corresponds to the value measured for Hyp dissolved in pure DMSO. This supports the idea that the local environment of the protein-bound fluorophores is likely characterized by the presence of the organic solvent, less polar than water. Importantly, the increment observed for the values of Φ_F, Φ_T and Φ_Δ relative to 2βLG-Hyp in the mixture cannot be attributed to a larger fraction of monomeric unbound Hyp molecules. Indeed the spectra recorded for Hyp alone in the mixed solvent (Fig. 4-36, grey curves) show the typical broadened and weak absorption bands of the aggregates, a barely detectable fluorescence emission ($\Phi_F < 0.001$) and negligible formation of the triplet state. It is therefore possible to conclude that the increased quantum yields observed in the presence of DMSO only arise from a better solvation Hyp molecules that are bound to the protein scaffold.

Additional molecular modeling studies performed in the binary mixture confirm the structural stability of the 2βLG-Hyp nanostructure. Fig. 4-39 reports the last snapshots collected at the end (250 ns) of a molecular dynamics simulation. The results of the simulation indicate that the presence of the DMSO does not alter the interaction of the Hyp molecule to the narrow cleft, nor impedes the binding of Hyp, either as monomer (Fig. 4-39 A) or dimer (Fig. 4-39 B), to the wider cleft, where the molecule is stacked against the indole ring of Trp77 (average distance between Hyp and indole ring 4.8 Å). The present results do not allow to determine the relative affinity of Hyp for the two clefts. However, it is worth to notice the relevant accumulation of DMSO molecules around the bound Hyp (blue contour in Fig. 4-39) in both the narrower and the wider cleft, particularly when Hyp is found as a monomer.

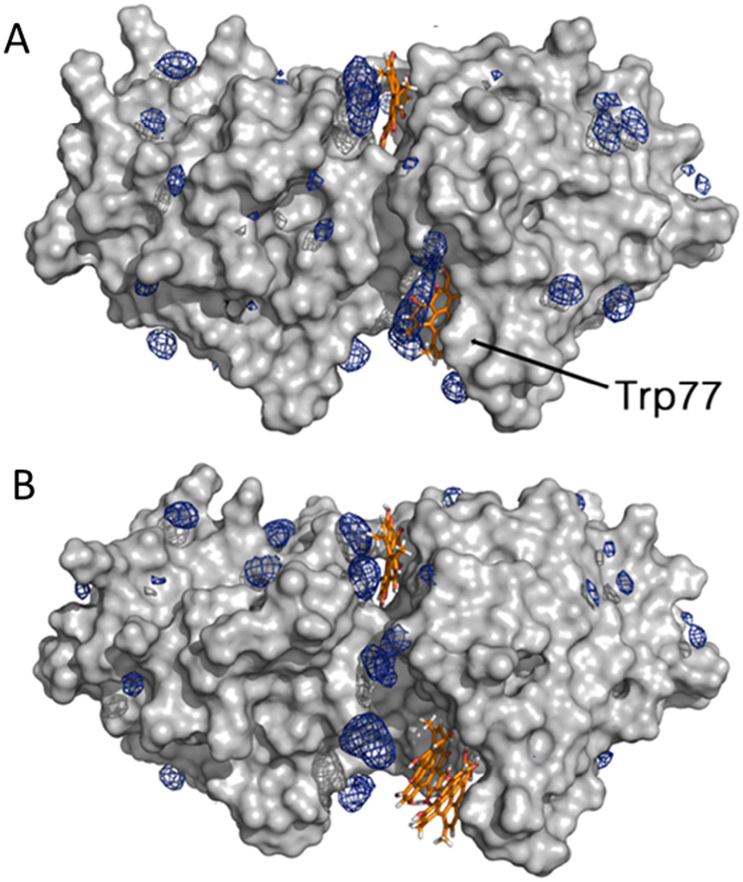

__Fig. 4-39__ Preferential distribution of DMSO molecules around the protein surface of 2βLG bound with Hyp molecules as monomers in the narrow cleft, and either monomer (A) or dimer (B) in the wide cleft. Blue isocontours denote a DMSO density of 0.3 g cm^{-3}*. Hyp molecules are represented with orange sticks.*

The preferential solvation of the protein by DMSO molecules would produce a more effective shielding of bound Hyp from the surrounding water molecules, which would offer a better local environment to the bound monomeric Hyp to preserve its photo-physics. This interpretation is in agreement with the observation, based on THz spectroscopy, that βLG is a rather hydrophobic protein, not displaying an extended long range hydration dynamics [12], as observed for other hydrophilic proteins [13] [14] [15]. An experimental determination of the affinity of Hyp to 2βLG by means of the analysis of a binding isotherm curve (as reported in Fig. 4-38 for the complex in pure buffer), although possible, is difficult. Indeed the intensity of fluorescence emission does not show a clear saturation at increasing concentration of Hyp, indicating the possible presence of additional low-affinity binding sites on the DMSO coated protein (data not shown). The trend of the integrated fluorescence emission collected at low Hyp concentrations in the presence of an excess of protein, do not allow to discriminate whether the presence of DMSO simply induce variations in the local environment of the Hyp molecules, thus favoring the fluorescence emission, or if it also induces an increase in the affinity of the two species.

4.3.4 2βLG-Hyp and bacterial cells in suspension

4.3.4.1 *Bacteria photo-inactivation*

As previously demonstrated, Hyp, either alone or delivered with a protein-based carrier, is able to induce an appreciable photosensitization-based inactivation only for Gram-positive bacteria. We thus focused of the Gram-positive *S. aureus* as a representative species to study the photo-activated antimicrobial properties of 2βLG-Hyp. Particular attention has been paid to the effect induced by the presence of DMSO as co-solvent. In pure PBS buffer, the 2βLG-Hyp nanostructure is an efficient photosensitizing agent for the elimination of *S. aureus* cells in suspension (Fig. 4-40 A). Upon irradiation, 2βLG-Hyp (4 µM Hyp with 200 µM βLG) induces a decrease of ~6 log units in the number of CFU at both 18 J cm^{-2} and 37 J cm^{-2} light doses (Fig. 4-40 A, green), an effect that is comparable to the one observed when the same amount of Hyp is added to the bacterial suspension as a concentrated solution in DMSO (Fig. 4-40 A, red), whose antimicrobial activity against Gram-positive bacteria is well-known [16] [17] [5]. An additional experiment was performed where, after the incubation period with the photosensitizing agent, the suspensions are centrifuged and the pellet is re-suspended in an equal volume of solvent while the supernatant is removed by suction. This washing procedure allows the removal of the species that are not tightly bound to the cells and can be simply separated by centrifugation. The results obtained for the washed suspensions in pure PBS do not significantly change. Free Hyp administrated as a concentrated solution decreased the number of CFU by 6 log units upon irradiation at both the light doses (Fig. 4-40 A, magenta), while 2βLG-Hyp induces a 5 to 6 log units decrease upon irradiation, with a slightly reduced dark toxicity (Fig. 4-40 A, dark green). These results demonstrate that the 2βLG-Hyp nanostructure is an efficient bio-compatible photosensitizing agent with interesting potential for antimicrobial applications against Gram-positive bacteria in the context of dairy industry. Indeed, the PS can be delivered to bacteria with 2βLG, which is present in high amounts in the milk whey, inducing an effective photo-inactivation of cell suspensions at µM concentration.

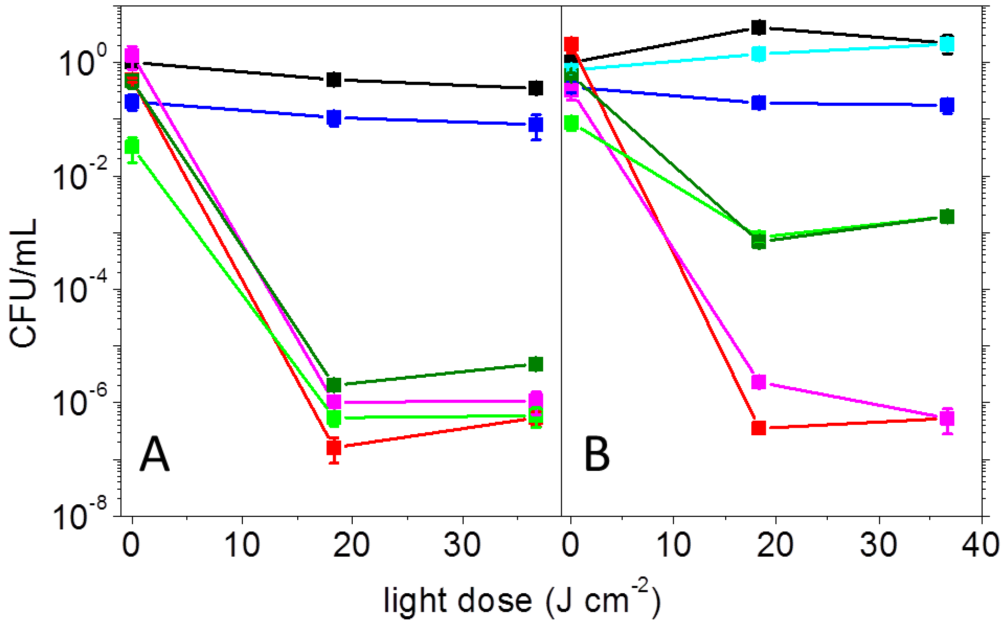

Fig. 4-40 *Photo-inactivation of S. aureus in suspension incubated with: 4 μM Hyp (red), 4 μM Hyp and washed with centrifugation (magenta), Hyp 4 μM complexed with βLG 200 μM (green), Hyp 4 μM complexed with βLG 200 μM and washed with centrifugation (dark green). The same experiments are performed in a PBS buffered solution (A) and in a mixture PBS-DMSO 20% (B). Controls are made for S. aureus suspension in PBS (black) ,in PBS-DMSO 20% (cyan) and in the presence of βLG 200 μM (blue).*

The enhancement of the photo-physical properties in the presence of DMSO, suggests that 2βLG-Hyp may improve its antimicrobial activity in the mixed solvent. This hypothesis is particularly supported by the fact that a larger efficiency of the photosensitization is observed in the presence of DMSO. The photo-inactivation experiments have been then repeated under the same previously-described experimental conditions, except for the use of the PBS-DMSO (DMSO 20%) mixture as solvent. The results are summarized in Fig. 4-40 B. Even though the presence of DMSO at this concentration is reported to affect the growth rate of bacteria [18], control experiments demonstrate that it does not appreciably reduce the number of countable CFU in our experiments (Fig. 4-40 B cyan). As reported in pure PBS buffer, adding free Hyp administered as a concentrated DMSO solution, induces a relevant photo-inactivation of bacteria resulting in a 6 to 7 log reduction in the number of CFU (Fig. 4-40 B, red). No substantial change occurs after the washing with centrifugation (Fig. 4-40 B, magenta). Surprisingly, the photosensitization-based antimicrobial effects of the 2βLG-Hyp complex are substantially reduced in the PBS-DMSO mixture, where the number of CFU decreases of ~3 log units upon irradiation at both the light doses (Fig. 4-40 B, green). This finding is in apparent contradiction with the value measured for the Φ_Δ of the complex, that is nearly twofold higher in the mixed solvent than in pure PBS.

4.3.4.2 Photo-physical properties in the presence of bacteria

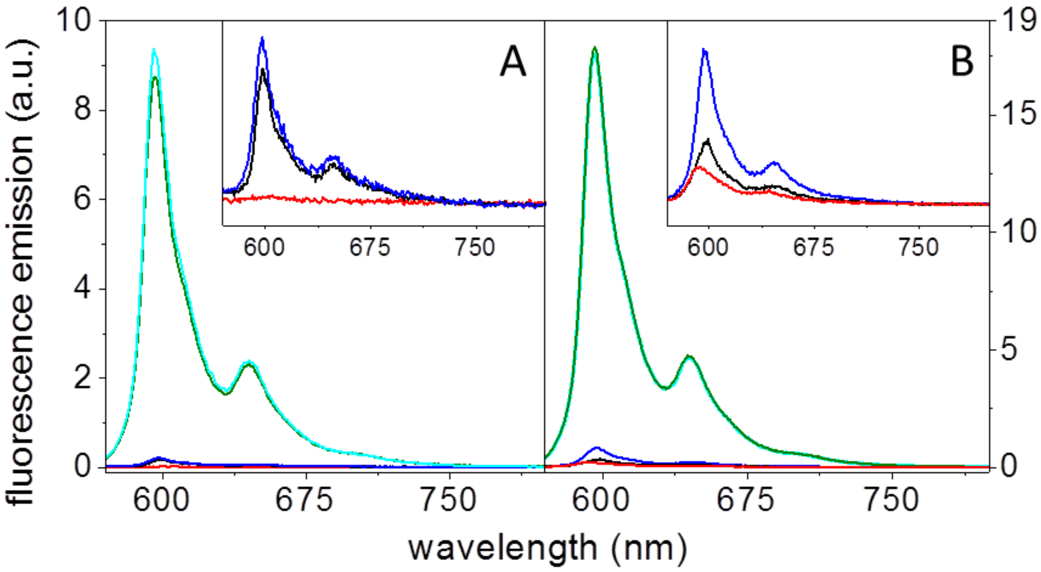

Fig. 4-41 *Fluorescence emission spectra collected in PBS buffer (A) and in the mixture PBS-DMSO 20% (B) for Hyp 4 μM (red), Hyp 4 μM incubated with S. aureus (black), Hyp 4 μM complexed with βLG 200 μM (dark green), Hyp 4 μM complexed with βLG 200 μM incubated with S. aureus (cyan), Hyp 4 μM complexed with βLG 200 μM, incubated with S. aureus and washed with centrifugation (blue). The insets represent a zoom for the less intense signals.* λ_{exc} *= 554 nm, T = 20°C.*

Some indications about the distribution of Hyp in the presence of *S. aureus* cells can be inferred from the comparison of the fluorescence emission spectra reported in Fig. 4-41. Free Hyp, i.e. in absence of the protein-based carrier, is aggregated in PBS buffer and no fluorescence can be detected at the concentration used (Fig. 4-41 A, red). When free Hyp is placed in the PBS-DMSO mixed solvent, the fluorescence emission is still extremely weak, indicating that the molecules is largely aggregated, but detectable (Fig. 4-41 B, red) allowing also the determination of a fluorescence decay lifetime of ~3.5 ns (Tab. 4-7). After the incubation with *S. aureus cells*, the emission spectra of free Hyp undergo minor but important changes: a slight increase of the emission intensity is observed in pure PBS (Fig. 4-41 A, black), while an increase of the emission and a band-shift are detected in the PBS-DMSO mixture (Fig. 4-41 B, black). This indicates a partial re-distribution of Hyp, where a fraction of the molecules are located in a different environment than the solvent, provided by the cells. Fluorescence decays collected from cells suspension are characterized by an intense scattering signal on the shortest time-scale (< 0.5 ns) that may produce a large uncertainty in the determined lifetime values and their relative amplitudes, particularly for unbound Hyp, whose fluorescence emission is extremely weak (Tab. 4-7). The interaction between the PS and the *S. aureus* cells is very likely a crucial event for the achievement of a relevant photosensitization-based inactivation of bacteria.

As previously discussed, the fluorescence emission of 2βLG-Hyp in PBS buffer (Fig. 4-41 A, dark green) is considerably more intense than the one of free Hyp, and it becomes even more intense in the mixed solvent (Fig. 4-41 B, dark green). No significant change is observed in the fluorescence emission spectra of 2βLG-Hyp after incubation with the bacterial cells, both in pure PBS buffer (Fig. 4-41 A, cyan) and in the PBS-DMSO mixture (Fig. 4-41 B, cyan). When the suspensions are washed with centrifugation, the intensity of the fluorescence emission is considerably reduced (Fig. 4-41 A-B, blue) and becomes comparable with the one observed for free Hyp incubated with bacteria. The small residual fluorescence intensity demonstrates a weak interaction of 2βLG-Hyp with the bacteria. Our results suggest that the large majority of Hyp molecules that are delivered with 2βLG, remain bound to the protein carrier also in the presence of the cells. Fluorescence lifetime values for 2βLG-Hyp in both PBS and PBS-DMSO retrieved from the analysis of the fluorescence decays (Tab. 4-7) undergo only minor variations after the incubation with bacteria. In the mixed solvent the fluorescence decay lifetime of 2βLG-Hyp is unaltered after the incubation with *S. aureus* cells (Tab. 4-7). In pure buffer, the bi-exponential character of the 2βLG-Hyp fluorescence decay is preserved, and only a slight increase of the shorter lifetime component, from 3.9 ns to 4.6 ns, can be appreciated upon addiction of bacteria (Tab. 4-7), which is of difficult interpretation because of the low signal-to-noise ratio of the decays. A further indication is given by the analysis of Hyp's triplet state decays: no changes in the triplet lifetime values are observed after the incubation of 2βLG-Hyp with bacteria, both in PBS and PBS-DMSO, where the Hyp retains a $\tau_T \approx 10$ μs, typical of the protein-bound species. No detectable signal for triplet state transient absorption can be appreciated when free Hyp is placed in the bacterial suspension, both in pure buffer and in the mixture, consistently with the above-reported observation that only a tiny fraction of molecules is solubilized by the interaction with the cells. These arguments support the idea that the 2βLG-Hyp construct remains intact in the presence of *S. aureus* cells. The DMSO coating does not appear to significantly affect the distribution of Hyp molecules, which are likely to remain mostly protein-bound in the presence of cells, both in pure buffer and in the mixture. However, in spite of the higher amount of photosensitized $^1O_2$ by 2βLG-Hyp, the DMSO coating appears to decrease the bioavailability of the photo-physically active compound, which results less efficient in the photo-killing of bacteria. This is possibly a consequence of an altered interaction between the cell wall and the 2βLG-Hyp nanostructure, owed to the organic solvent coating.

sample	solvent	τ_1 (ns)	τ_2 (ns)	τ_3 (ns)
Hyp	DMSO	-	-	5.5±0.1 (100%)
Hyp	PBS-DMSO 20%	-	3.5 (100%)	-
Hyp + *S. aureus*	PBS	0.2 (48%)	4.2 (52%)	-
Hyp + *S. aureus*	PBS-DMSO 20%	0.5 (48%)	3.6 (52%)	-
2βLG-Hyp	PBS	-	3.9 (35%)	6.7 (65%)
2βLG-Hyp	PBS-DMSO 20%	0.2 (20%)	-	5.6 (80%)
2βLG-Hyp + *S. aureus*	PBS	-	4.6 (45%)	7.0 (55%)
2βLG-Hyp + *S. aureus*	PBS-DMSO 20%	-	-	5.5 (100%)

Tab. 4-7 *Results of the analysis of fluorescence decays with multi-exponential models. Lifetimes and the relative amplitudes are reported for Hyp and 2βLG-Hyp in solution and after incubation with S. aureus cell suspensions, both pure PBS buffer and the mixture PBS-DMSO are used as solvents. The fastest component (*τ_1*) is due to light scattering.* λ_{exc} *= 450 or 375 nm,* λ_{det} *= 600 nm. βLG is always in excess with respect to Hyp (50:1).*

4.3.5 Chapter bibliography

1. Mercadante, D. *et al.* Bovine β-lactoglobulin is dimeric under imitative physiological conditions: dissociation equilibrium and rate constants over the pH range of 2.5-7.5. *Biophys. J.* **103,** 303–12 (2012).
2. Dufour, E., Genot, C. & Haertlé, T. β-lactoglobulin binding properties during its folding changes studied by fluorescence spectroscopy. *Biochim. Biophys. Acta - Protein Struct. Mol. Enzymol.* **1205,** 105–112 (1994).
3. Rodríguez-Amigo, B. *et al.* The complex of hypericin with β-lactoglobulin has antimicrobial activity with potential applications in dairy industry. *J. Dairy Sci.* **98,** 89–94 (2015).
4. Kontopidis, G., Holt, C. & Sawyer, L. Invited Review: β-Lactoglobulin: Binding Properties, Structure, and Function. *J. Dairy Sci.* **87,** 785–796 (2015).
5. Comas-Barceló, J. *et al.* A self-assembled nanostructured material with photosensitising properties. *RSC Adv.* **3,** 17874 (2013).
6. Jacobson, J. M. *et al.* Pharmacokinetics , Safety , and Antiviral Effects of Hypericin , a Derivative of St . John ' s Wort Plant , in Patients with Chronic Hepatitis C Virus Infection. *Antimicrob. Agents Chemother.* **45,** 517–524 (2001).
7. English, D. S. *et al.* Hypericin, Hypocrellin, and Model Compounds: Primary Photoprocesses of Light-Induced Antiviral Agents. *J. Phys. Chem. A* **101,** 3235–3240 (1997).
8. Delcanale, P. *et al.* Subdiffraction localization of a nanostructured photosensitizer in bacterial cells. *Sci. Rep.* **5,** 15564 (2015).
9. Arakawa, T., Kita, Y. & Timasheff, S. N. Protein precipitation and denaturation by dimethyl sulfoxide. *Biophys. Chem.* **131,** 62–70 (2007).
10. Cowie, J. M. G. & Toporowski, P. M. Association in the bunary liquid system dimethyl sulphoxide - water. *Can. J. Chem.* **39,** 2240–2243 (1961).
11. LeBel, R. G. & Goring, D. A. I. Density, Viscosity, Refractive Index, and Hygroscopicity of Mixtures of Water and Dimethyl Sulfoxide. *J. Chem. Eng. Data* **7,** 100–101 (1962).
12. Vondracek, H., Dielmann-Gessner, J., Lubitz, W., Knipp, M. & Havenith, M. THz absorption spectroscopy of solvated β-lactoglobulin. *J. Chem. Phys.* **141,** 22D534 (2014).
13. Ebbinghaus, S. *et al.* An extended dynamical hydration shell around proteins. *Proc. Natl. Acad. Sci.* **104,** 20749–20752 (2007).
14. Ebbinghaus, S. *et al.* Antifreeze Glycoprotein Activity Correlates with Long-Range Protein−Water Dynamics. *J. Am. Chem. Soc.* **132,** 12210–12211 (2010).
15. Heyden, M. *et al.* Long-Range Influence of Carbohydrates on the Solvation Dynamics of Water—Answers from Terahertz Absorption Measurements and Molecular Modeling Simulations. *J. Am. Chem. Soc.* **130,** 5773–5779 (2008).
16. Aponiene, K., Paskeviciute, E., Reklaitis, I. & Luksiene, Z. Reduction of microbial contamination of fruits and vegetables by hypericin-based photosensitization: Comparison with other emerging antimicrobial treatments. *J. Food Eng.* **144,** 29–35 (2015).
17. Paz-Cristobal, M. P. *et al.* Photodynamic fungicidal efficacy of hypericin and dimethyl methylene blue against azole-resistant Candida albicans strains. *Mycoses* **57,** 35–42 (2014).
18. Negin, S. *et al.* The aqueous medium-dimethylsulfoxide conundrum in biological studies. *RSC Adv.* **5,** 8088–8093 (2015).

4.4 Nanostructures based on albumins: BSA as carrier for triplet emitters molecules

Triplet emitters molecules are gaining growing interest as photo-physically active compounds for applications in bio-imaging. The photo-physics of these compounds is indeed widely tunable and the emission of luminescence occurs from an admixture of excited states, often leading to observed photo-physical parameters which are unusual in comparison to standard fluorescent reporters [1]. One of the most intriguing properties is the long lifetime of luminescence decay that, for the compounds studied in this work, occurs on the μs time-scale, thus about 3 order of magnitude longer than a usual fluorescence, and emission quantum yields that are comparable with those of fluorophores. Additionally, the partial triplet character of the excited state opens the possibility to exploit them as PSs or as sensors for O_2. Unlike the previously described photo-active molecules, triplet emitters are synthetic compounds that may be poorly bio-compatible. Moreover, several of them dramatically change the photo-physical properties upon aggregation. Similarly to previous examples, where a PS molecule was delivered with a protein-based carrier, the aim is to realize a self-assembled nanostructure where the active triplet emitter molecule is combined into the protein-based carrier which confers bio-compatibility and preserves the photo-physical properties that are optimal for applications. We selected BSA as protein-based carrier since it constitutes a wide-spread transport system for many structurally and chemically different molecules in blood flow [2], and thus represents a useful standard. Attempts have been made also with apoMb, but further studied will be needed to evaluate the formation of a stable apoMb-based nanostructure for the transport of the investigated triplet emitters molecules.

4.4.1 AG97 and AG113

The quasi-square planar Pt-complexes named AG97 and AG113 (Fig. 4-42) have been selected as possible candidates for the interaction with protein carriers. They are indeed extremely hydrophobic compounds having a fairly similar size and shape to the previously-described photo-active compounds (Hyp and Zn-PP IX), so that it is plausible to speculate a binding with protein carriers exposing suitable hydrophobic sites. The high extent of the hydrophobic aggregation of these compounds has been soon identified as a major problem, since it leads to an extremely slow equilibration of the system in aqueous solution. As a result, the spectroscopic properties of these molecules placed in aqueous buffer are poorly stable in time (important changes are observed in spectra on the time-scale typical of experiments), and scarcely reproducible, being dependent on small variations of concentration and sample preparation. To partially overcome this problem, we first chose to focus on AG97 as photo-active compound. Because of the more bulky ancillary ligand than AG113, which is completely flat, AG97 is likely to exhibit a less pronounced tendency towards aggregation with respect to AG113 [3]. Indeed, its photo-physical properties appear slightly more stable and reproducible than those of the other compound, e.g. the spectra changed in intensity during time but without undergoing substantial changes in shape, as observed for AG113. The values of photo-physical parameters obtained for AG97 placed in aqueous solutions will be therefore affected by a large uncertainty, but can be considered sufficiently reproducible to allow a (qualitative) comparison with samples obtained for the same compounds under different conditions, e.g. in the presence of the protein carrier.

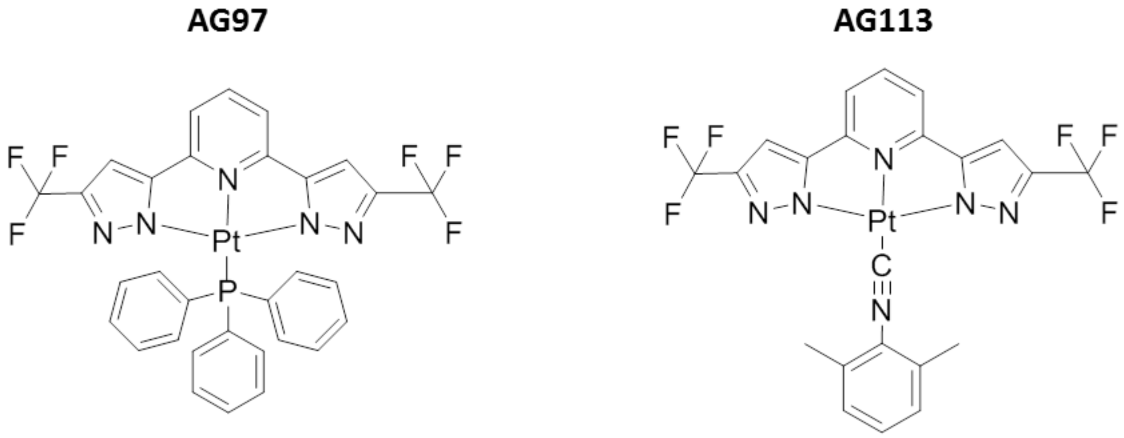

Fig. 4-42 *Chemical structures of AG97 and AG113.*

4.4.2 AG97 spectroscopic properties in solution

AG97 is readily soluble in organic solvents, particularly dichloromethane (DCM), DMSO or EtOH where it shows structured absorption bands around 340 nm and 400 nm (Fig. 4-43). The aggregated complex in PBS buffer displays only one main broadened absorption band centered at 350 nm and an intense background due to light scattering, particularly relevant at the shorter wavelengths (Fig. 4-43, blue). Unlike the previously described photo-active molecules, the emission of AG97 results completely quenched in DMSO (Fig. 4-43, dashed dark green) and extremely weak also in other organic solvents like DCM or EtOH where it is barely detectable. Conversely, the complex exhibits a clear structured emission (quantum yield ~0.05) in PBS buffer, i.e. in its aggregated form, with two band centered at around 470 nm and 497 nm (Fig. 4-43, dashed blue). This is a rather unusual behavior since aggregation is often known to promote non-radiative processes, as happens for Hyp. It is not easy to find a clear explanation even if some reasonable hypothesis can be put forward, e.g. a mechanism of quenching induced by organic solvents; an increased rigidity of the molecule in the aggregate favoring the radiative processes; a weak coupling in the aggregates due to the bulky ancillary ligands or a shielding from solvent due to the tight aggregation.

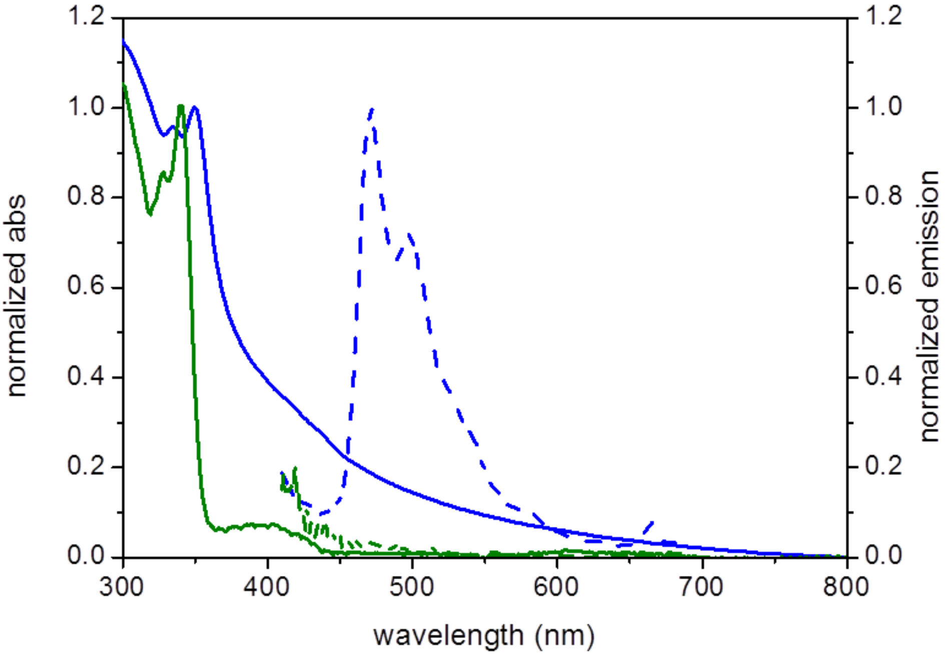

Fig. 4-43 *Normalized absorption (straight) and emission (dashed) spectra for AG97 in PBS buffer (blue) and DMSO (green). Absorption spectra are normalized for the peak value, emission spectra are normalized for peak value of AG97 in DMSO.*

As previously mentioned, a relevant problem concerning the use of pure AG97 in physiological condition is stability, since both emission spectra and luminescence decay in PBS solutions are characterized by a large uncertainty and are scarcely reproducible. Additionally, a change in the emission intensity is observed on a time-scale of hours. The poor stability of the complex in PBS buffer is likely a consequence of multiple equilibria of aggregation rather than a chemical degradation, leading to a slow equilibration of the system and represents a major drawback for potential application of pure AG97 in biosystems.

The values of emission decay lifetimes obtained for AG97 in PBS buffer, despite affected by a large uncertainty owed to the poor stability, are in the order of a μs (Tab. 4-8), as observed for similar triplet emitter species [4] [1]. The lifetime decreases by roughly two order of magnitude in EtOH or DCM, where the emission is barely detectable (Tab. 4-8), consistently with the above-mentioned quenched emission observed in organic solvents. An interesting feature of AG97 is the substantial insensitivity of its photo-physical parameters to variations in the concentration of O_2 in solution (Tab. 4-8). Even an intense bubbling of Argon, used for de-oxygenation, only induced a degradation, likely of mechanical origin, of the complex in PBS without affecting its luminescence lifetime or the shape of the spectra. This insensitivity to O_2 is rather unexpected considering the partial triplet character of the molecule's excited state. In organic solvents it likely arises from the fast non-radiative de-population of the excited state, which dominates over other relaxation mechanisms. In the case of AG97 in the aqueous buffer, this property appears to be a consequence of the hydrophobic aggregation, but a clear explanation is difficult to identify. A possible hypothesis is that AG97 molecules embedded in the aggregates are almost completely shielded from solvent, so that O_2 cannot appreciably quench the excited state and no detectable change is observed upon de-oxygenation. For the purposes of this work, it is important to point out that in physiologically relevant conditions there is no spectroscopic evidence of any interaction a of AG97 with O_2, and the compound retains a long emission lifetime in the µs range, typical of triplet emitters.

	air-equilibrated			**de-oxygenated**	
solvent	**τ_1**	**τ_2**	**Φ_{em}**	**τ_1**	**τ_2**
PBS	(0.83±0.11) µs 39%	(2.95±0.25) µs 61%	0.05	(0.73±0.09) µs 35%	(2.93±0.27) µs 65%
EtOH	1-10 ns	-	~0.00	1-10 ns	-
DCM	~19 ns	-	~0.00	~19 ns	-

Tab. 4-8 *Spectroscopic properties of 3 µM AG97 in several solvents. τ and Φ_{em} are the lifetimes and quantum yield of luminescence emission respectively (λ_{exc} = 350 nm or 340 nm; λ_{det} = 470 nm; T = 20°C); De-oxygenation is obtained with a moderate flow of pre-equilibrated Argon in solution for 20 minutes.*

4.4.3 Interaction of AG97 with BSA: a stable nanostructure

Since proteins can protect hydrophobic compounds against interactions with the solvent, the poor spectroscopic stability of Pt-complex AG97 in physiological conditions may be overcome using this approach. The formation of a stable complex between AG97 and BSA in PBS buffer can be assessed spectroscopically, even if with rather different methods than the ones previously used for the PSs, due to the different photo-physical behavior of the triplet emitter. An experiment is carried out where a simple PBS solution and a 3 µM solution of BSA in PBS were titrated with increasing AG97 concentration from 0 to 20 µM. Experimental conditions and volumes added during the titrations were the same for both solutions, allowing a direct comparison of the results. Absorption spectra are reported in Fig. 4-44, where it is immediately possible to notice that the contribution due to light scattering (a structure-less, Rayleigh-like increase in apparent absorbance at decreasing wavelengths) induced by AG97 aggregates is more intense for a pure buffer (Fig. 4-44 A), than for a buffer in the presence of BSA (Fig. 4-44 B).

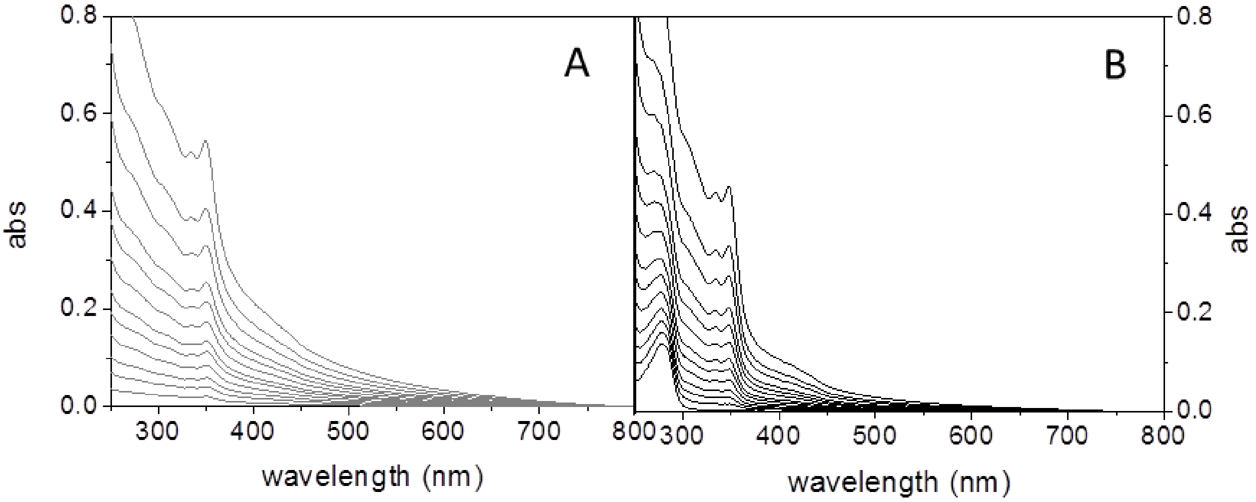

Fig. 4-44 *Absorption spectra for PBS buffer solution titrated with increasing AG97 (grey A) and for 100 μM BSA titrated with increasing AG97 (black B). Titrations are obtained in the same experimental conditions, AG97 concentrations range from 0 to 20 μM.*

Despite based on a qualitative consideration, this result indicates that the hydrophobic aggregation of AG97 is controlled by the presence of BSA. A more consistent proof for the interaction between AG97 and BSA can be obtained by comparing the results obtained from fitting of time-resolved luminescence decays with a bi-exponential model. The histograms of Fig. 4-45 report the values obtained for AG97 emission lifetimes (bars) and their relative amplitude, corresponding to the pre-exponential factor in the model (dots). This representation allows to immediately appreciate how in the presence of BSA the values obtained are more consistent and are reproducible for the different AG97 concentrations (Fig. 4-45 B). Conversely, the results obtained for the titration in simple PBS solution (Fig. 4-45 A) are scattered, characterized by a large uncertainty and exhibit a slight systematic increase of the lifetimes (grey bars) at increasing AG97 concentrations. The instability of these results is likely a consequence of the aggregation of AG97 in the aqueous buffer. However, this comparison demonstrates that the presence of the protein is crucial to obtain a system that is stable and reproducible for different AG97 concentrations (in the range 0-20 μM) and in physiologically relevant conditions. The average values obtained from the analysis of data reported in Fig. 4-45 are: $<\tau_1> = (0.59 \pm 0.13)$ μs (~70%), $<\tau_2> = (2.36 \pm 0.44)$ μs (~30%) for AG97 in pure PBS buffer. The poor correspondence of these average values with the one reported in Tab. 4-8, obtained from a single concentration of AG97, gives an idea of the limited reproducibility of the results. In the presence of BSA, systematically shorter values are obtained for both components of the luminescence decay, with significantly lower uncertainty (one order of magnitude): $<\tau_1>$ = (0.28 ± 0.05) μs (~57%) and $<\tau_2>$ = (0.91 ± 0.06) μs (~43%). The shorter lifetimes are consistent with the reduced Φ_{em} of 0.02 measured in the presence of a large excess of BSA, with respect to the one (Φ_{em} = 0.05) obtained in pure buffer (Fig. 4-46).

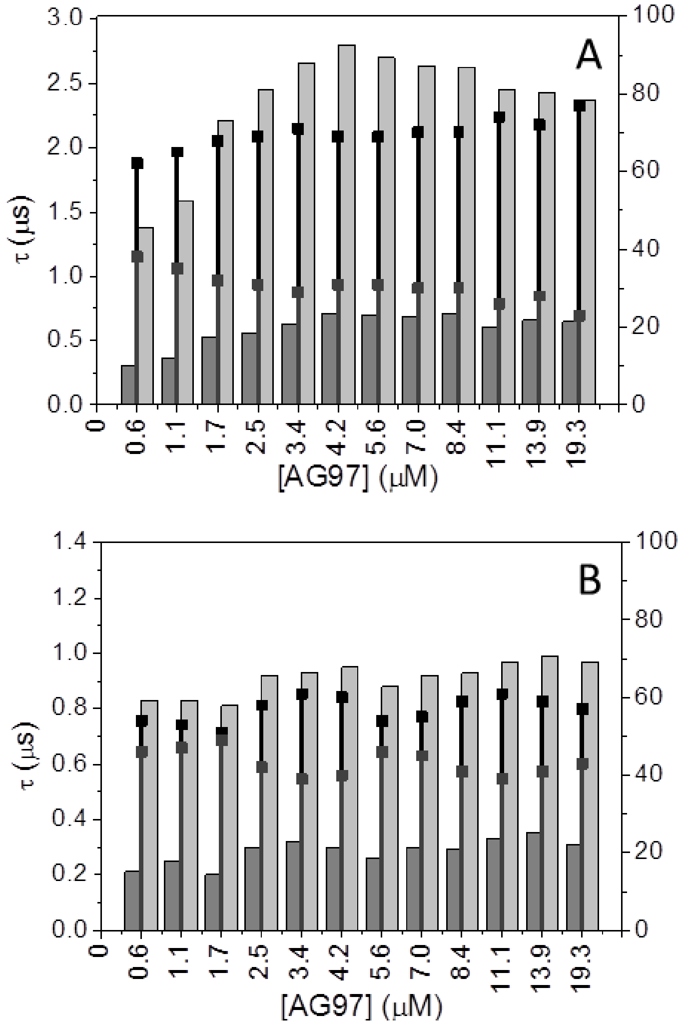

Fig. 4-45 *Lifetime values τ_1 (dark gray bar) and τ_2 (light gray bar) and respective pre-factors A_1 (black dots) and A_2 (grey dots) for different AG97 concentrations in PBS buffer (A) and in 100 μM BSA (B). Values are obtained from a fitting of the emission decays with a bi-exponential model; λ_{exc} = 350 nm, λ_{det} = 465 nm.*

The shortened lifetimes together with the reduction of Φ_{em} demonstrate the existence of an interaction between AG97 and BSA. However, the position of both absorption and emission bands is substantially unaltered in the presence of the protein (Fig. 4-44 and 4-46), suggesting that the AG97 molecules are placed in conditions similar to those experienced in PBS, and thus molecules likely retain a residual aggregation the presence of the albumin. A plausible interpretation is that an homogeneous population of small weakly scattering clusters of AG97 is stabilized by the interaction with BSA, that acts like a template. The presence of an homogeneous population is demonstrated by the consistency of data, while the reduction of lifetimes in the presence of BSA suggests the existence of smaller clusters, that possibly lead to a less extended shielding from the solvent, even thou a direct quenching by the protein cannot be excluded.

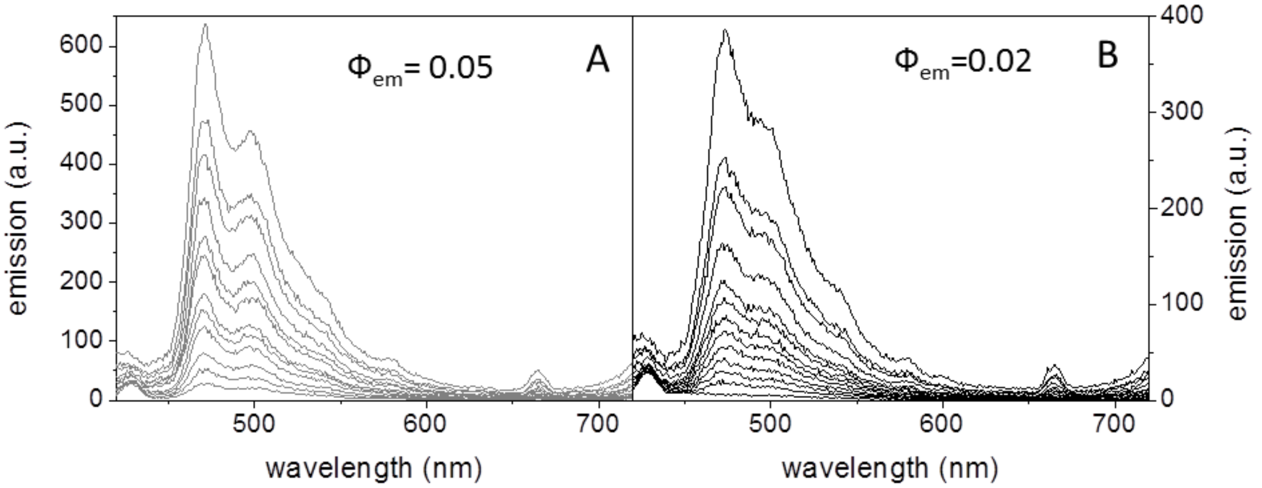

Fig. 4-46 *Emission spectra for PBS buffer solution titrated with increasing AG97 (A) and for 100 µM BSA titrated with increasing AG97 (B). Titrations are obtained in the same experimental conditions, AG97 concentrations range from 0 to 20 µM. Emission quantum yields are shown in the insets and are obtained by a direct measurement comparing the number of absorbed photons with the number of emitted photons, that are collected with an integrating sphere component.*

An important observation is that, as previously observed for AG97 in pure buffer, changes in the concentration of O_2 in solution, do not lead to any appreciable spectroscopic change for AG97 interacting with BSA, particularly in the emission lifetimes. In the experiments carried out to determine the sensitivity to O_2, a large excess of BSA was added to ensure that the large majority of AG97 is actually interacting with the protein. Unfortunately, a precise quantitative determination of the emission lifetimes from the analysis of (partially) de-oxygenated solutions is difficult. Indeed the Argon flow used for de-oxygenation, even if used with attention, unavoidably lead to degradation of a minor fraction of high concentrated BSA (100 µM) producing an intense scattering signal at the lowest times (< 60 ns). However, a simple comparison of the curves showed in Fig. 4-47 allows to conclude that the de-oxygenation does not induce any significant change in the emission decay lifetime with respect to the air-equilibrated sample, particularly considering that lifetimes of molecule's triplet states usually undergo a change of several order of magnitude after these de-oxygenation processes [5].

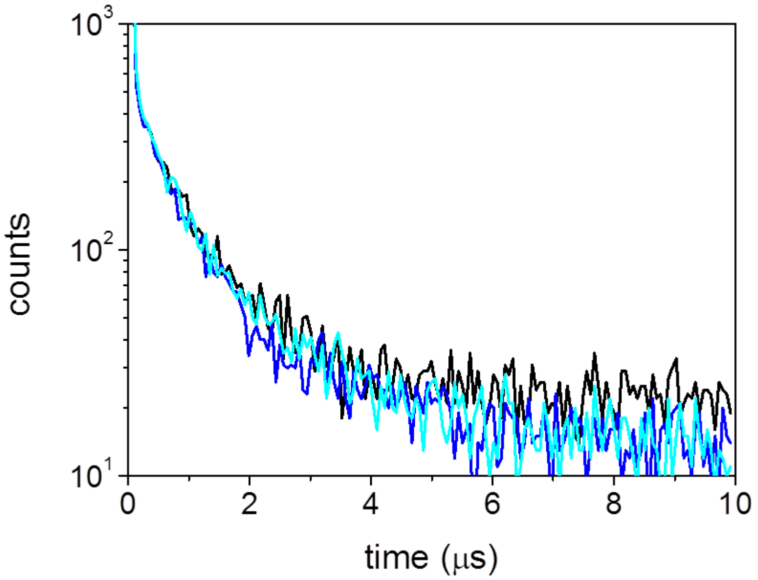

Fig. 4-47 *Time-resolved emission (λ_{exc} = 370 nm, λ_{det} = 470 nm, T = 20°C) for 100 μM BSA with 2.5 μM AG97 in PBS buffer air-equilibrated (black) and after 60 min (blue) and 120 min (cyan) of de-oxygenation with gentle flux of Argon. The shortest times are cut because affected by large scattering.*

4.4.4 Potential of BSA-AG97 as luminescent probe for bio-imaging

The above findings allow us to conclude that the photo-physical properties of AG97 undergo a remarkable improvement with the interaction with BSA, that make this nanostructure a potentially interesting luminescent reporter for bio-imaging. It is indeed: spectroscopically stable and reproducible in the physiological buffer, as a consequence of the increased water-solubility owed to the albumin's structure; it retains a luminescence emission on the μs time-scale with a detectable intensity, which is considerably longer than the fluorescence of usual fluorescent reporters; the excited state of AG97 does not appear to have any sizeable reactivity with O_2 in the nanostructure. This is particularly interesting since photo-excited states of similar molecules, having a triplet character, often behave like PSs and generate reactive oxygen species. These are likely to cause a photo-oxidative damage in the system under investigation, which is an unwanted effect for a molecule that is meant to be used as probe.

4.4.5 Labelling of BSA with FITC: BSAFITC-AG97 nanostructure

A relevant issue when performing experiments based of fluorescence detection on a real biological sample, e.g. an organelle, a cell or a tissue, is to distinguish the emission of the fluorescent probe from background noise and from sample's autofluorescence, that usually occur on the same time-scale [6] [7] [8]. It is thus easy to understand that one of the most promising properties of the nanostructure formed by AG97 conjugated with BSA (BSA-AG97) lies in its long lifetime of luminescence decay, which is 2 to 3 orders of magnitude longer than the lifetime of a typical fluorescent probe. This potentially enables a rather simple experimental discrimination of the emission of the nanostructure from any fluorescence, autofluorescence or scattering, for example by introducing a temporal gating on the time-resolved signal [9] [10].

In order to simulate an intense autofluorescence, the BSA was covalently labelled with a common fluorescent reporter, widely used in biology, the Fluorescein Isothiocyanate (FITC). The purified BSA protein labelled with FITC (BSAFITC) is easily obtained by a standard procedure in PBS buffer [11] [12]. The binding of FITC to the amino acidic chain was confirmed by a 6 nm red-shift in the absorption and emission spectra and by a change in the fluorescence decay of FITC after the conjugation with BSA. A bi-exponential model with τ_1 = 2 ns (15%) and τ_1 = 4 ns (85%) is indeed used to well-describe the decay for free FITC in PBS, while a different model comprising three components, τ_1 = 0.2 ns (41%), τ_2 = 1.3 ns (26%) and τ_3 = 4.0 ns (33%), is necessary for BSAFITC.

The presence of the FITC does not appear to significantly alter the interaction between AG97 and the protein-based structure since the same arguments used for BSA-AG97 holds true for BSAFITC-AG97. A straightforward qualitative indication of the interaction between BSAFITC and AG97 is provided by the reduction of scattering background in absorption spectra due to AG97 aggregation upon addition of BSAFITC, exactly as happens for unlabeled BSA (Fig. 4-49 A and B).

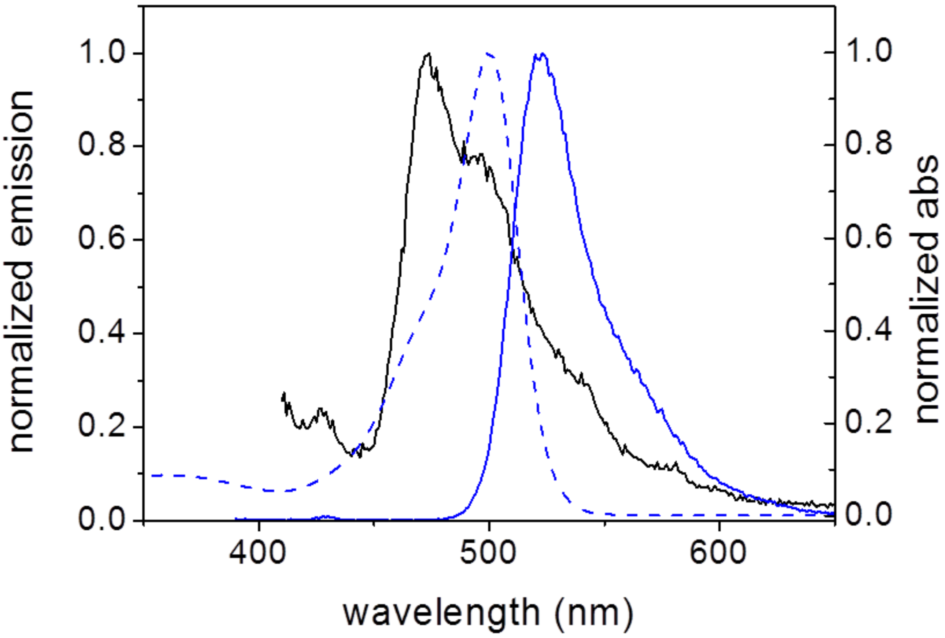

Fig. 4-48 *Emission spectrum of AG97 bound to BSA (black solid, λ_{exc}= 375 nm), absorption (blue dashed) and emission (blue solid) spectra of BSA labelled with FITC . Spectra are normalized for the maximum value.*

A careful inspection of Fig. 4-48, where a comparison of the emission spectra of the species forming the nanostructures is displayed, allows to identify three different spectral regions. Around 470 nm, where BSAFITC does not emit, AG97 exhibits a maximum of emission and therefore only luminescence from Pt-complex is selectively detected at this wavelength. In the spectral region between 490 and 570 nm, both components emit: BSAFITC has its maximum emission at 525 nm occurring with high quantum yield (close to the unity [12]) but on a ns time-scale, while AG97 exhibits a less intense emission, occurring on a µs time-scale. Finally, at ~600 nm the luminescence of AG97 is negligible and only the fluorescence emitted by labelled protein can be appreciably detected. The photo-physical features of the BSAFITC-AG97 nanostructure allows to selectively monitor the decays of the two luminescent components either by setting different detection wavelengths or by introducing a temporal discrimination in the time-resolved luminescence signal. So that a rather accurate analysis of the photo-physics of the nanostructure is possible.

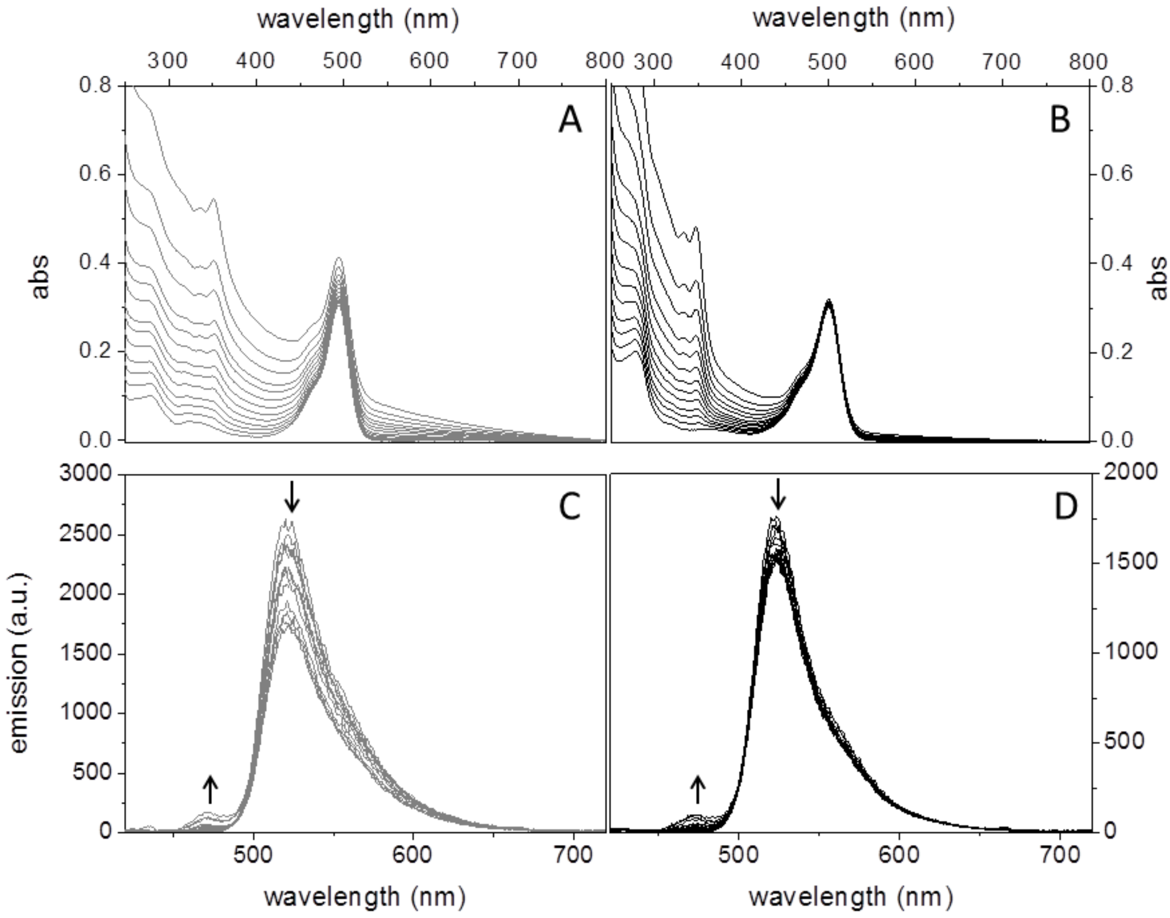

Fig. 4-49 *Absorption (A-B) and emission (C-D) spectra obtained for the titration of FITC in PBS (A and C, grey) and BSAFITC in PBS (B and D, black) with increasing AG97. Experimental conditions are kept constant for both measurements.*

4.4.6 Gated detection as tool for a selective acquisition of the AG97 signal

The properties of the nanostructure have been characterized by means of two parallel titration experiments, where a solution of BSAFITC and a control solution of pure FITC in PBS are titrated with increasing AG97 concentration and the spectroscopic parameters are monitored. The concentrations of FITC and BSAFITC were adjusted in order to have the same peak absorption, corresponding to a comparable amount of FITC fluorophores, either free or bound to the protein structure. The acquisition parameters and the experimental conditions, including the volume of AG97 added, were kept constant for both the experiments, in order to allow a reliable comparison of the results. The obtained absorption spectra at increasing AG97 concentrations are collected in Fig. 4-49 A (free FITC with AG97) and Fig. 4-49 B (BSAFITC with AG97), where it is easy to recognize the absorption band due to FITC, centered around 500 nm. As previously discussed, it can be appreciated how the presence of the BSAFITC limits the aggregation of Pt-complex in PBS, thus reducing the light scattering when compared with the solution with free FITC. The emission spectra are reported in Fig. 4-49 C (free FITC with AG97) and Fig. 4-49 D (BSAFITC with AG97), where the intense emission of FITC can be identified at 525 nm. When the concentration of AG97 is increased, its emission band at 470 nm can be recognized, even if it remains considerably lower than the one of FITC. The lowered intensity of the FITC emission band observed at the higher concentrations of AG97 is owed to the filter effect due to the light scattering induced by aggregates, and it is consequently more relevant for the solution of free FITC (Fig. 4-49 C) than for BSAFITC (Fig. 4-49 D). In the spectral region where emissions overlap, i.e. 490 – 570 nm, the steady-state spectra reported in Fig. 4-49 D do not allow to distinguish the weak luminescence of AG97 hidden in the intense fluorescence of BSAFITC. The easiest way to experimentally isolate AG97 emission would be to set the detection wavelength sharply around 470 nm. However, in a real biological sample, autofluorescence may be really intense in this region, because of the emission of common endogenous fluorophores like NADH or flavins [7] [6]. Moreover, steady-state spectra obtained on simple bio-samples, e.g. cell suspensions, are often largely affected by filter effect due to turbidity, which makes them poorly quantitative.

A reliable experimental method for selective detection of AG97 luminescence in the presence of an intense fluorescence was obtained with a time-gated detection, exploiting the different emission time-scale of the components. Fig. 4-50 reports the gated emission spectra obtained during parallel titrations of four different solutions, namely free FITC, BSAFITC, pure PBS buffer and BSA, at increasing concentration of AG97. The same temporal gating is used at every detection wavelength, so that the signal acquired on the shorter time-scale (< 128 ns) is discarded while the signal occurring on the longer time-scale (128 ns – 8 μs) is integrated to give the spectrum.

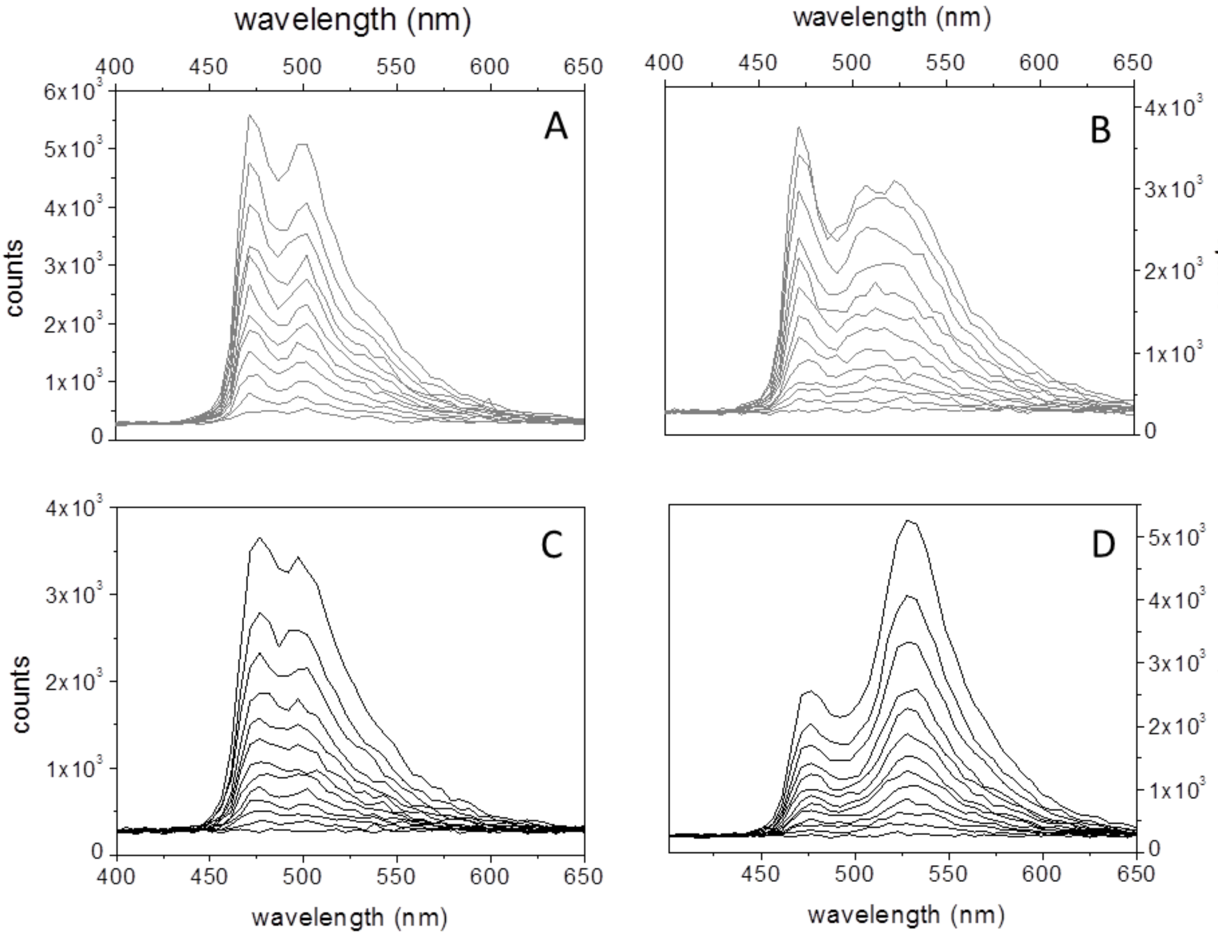

Fig. 4-50 *Gated emission spectra obtained for solutions of PBS buffer (A), free FITC (B), BSA (C) and BSAFITC (D) titrated with increasing AG97. Experimental conditions are kept constant during measurements. Gated spectra are collected after pulsed laser excitation at 375 nm (freq = 100 kHz) with MCS acquisition mode (bandwidth = 32 ns, integration time = 5 s) with a delta of 5 nm, the signal is integrated in the range 128 ns – 8 µs.*

Experimentally, the reported gated spectra are collected using MCS acquisition mode. Analogous spectra have been recorder in TCSPC acquisition mode, even though in this case they could be affected by pile-up error, particularly at the detection wavelengths with the higher count rate. However, an analysis demonstrated that the results obtained in TCSPC mode are consistent with those of MCS, with no significant detectable bias, so that the two methods can be considered consistent for our purposes.

The shape of gated emission spectra obtained for AG97 in pure PBS buffer (Fig. 4-50 A) or with BSA (Fig. 4-50 C), that is in absence of fluorescence, are perfectly consistent to those obtained with usual steady-state emission detection, displayed in Fig. 4-48. The lower resolution of the gated spectra is due to the 5 nm spacing between wavelengths, chosen to avoid too long acquisition times. Gated spectra are also reported for AG97 with free FITC (Fig. 4-50 B) and with BSAFITC (Fig. 4-50 B), namely in the presence of an intense fluorescence. In these cases the emission band of AG97 can be much better appreciated than in the corresponding steady-state spectra of Fig. 4-49 C and D. However, it can be immediately recognized that a residual contribution of FITC emission is still present in gated spectra with an emission band at 525 nm. This is particularly evident in the presence of BSAFITC (Fig. 4-50 D), where the emission band due to the fluorophore is even more intense than the one of AG97 centered at 470 nm. Since the lifetimes of fluorescence decay for both FITC and BSAFITC are in the order of few ns, it is excluded that a residual fluorescence is able to generate such an intense band in the gated spectra, i.e. in a time range of 128 ns – 8 μs. Additionally, the extent of the FITC emission at 525 nm appears to grow during the titration, along with the increase of AG97 concentration. These observations suggest the occurring of an energy transfer between AG97 (donor) and FITC (acceptor), leading to a delayed emission of FITC on the μs time-scale. In Fig. 4-48 it is possible to see that the emission spectrum of AG97 and the absorption spectrum of BSAFITC are significantly overlapped so that the resonant condition for energy transfer is fulfilled.

4.4.7 Energy transfer

	PBS buffer + AG97		**FITC + AG97**		**BSA + AG97**		**BSAFITC + AG97**	
λ_{det}	$<\tau_1>$	$<\tau_2>$	$<\tau_1>$	$<\tau_2>$	$<\tau_1>$	$<\tau_2>$	$<\tau_1>$	$<\tau_2>$
470 nm	0.59±0.13 70%	2.36±0.44 30%	0.39±0.13 64%	1.39±0.42 36%	0.28±0.05 57%	0.91±0.06 43%	0.21±0.03 57%	0.76±0.03 43%
600 nm	-	-	0.24±0.09 64%	1.16±0.25 36%	-	-	0.14±0.02 67%	0.63±0.05 33%

Tab. 4-9 *Lifetimes values from fitting with bi-exponential model (λ_{exc} = 375 nm, T = 20°C, MCS mode with 32 ns resolution). The values for lifetimes are expressed in μs. The average values are obtained from the data of titrations of 4 solutions (free FITC, BSAFITC, PBS buffer and BSA) with increasing concentrations of AG97. The same experimental conditions were used.*

Tab. 4-9 allows a direct comparison of the results obtained from the analysis of emission decays of the four titrations considered, the reported lifetimes result from the average of the values retrieved within a titration. The selected detection wavelengths correspond to the spectral regions where there is appreciable emission only from a single component: only AG97 emission is observed at 470 nm whereas only FITC emission is significantly observed at 600 nm. For solutions of free FITC and BSAFITC it is nice to observe that the lifetimes measured at 470 nm are roughly consistent with those observed at 600 nm, supporting the idea of an energy transfer from AG97 to FITC. Additionally, a shortening of AG97 lifetimes monitored at 470 nm can be appreciated in the presence of FITC or BSAFITC, with respect to the control solutions of pure PBS buffer or BSA, that are obtained under the same conditions but in absence of fluorophore. This result indicates the presence of a quenching of AG97 emission induced by FITC.

A comparison of the relative intensity of 525 nm emission band in Fig. 4-50 B and D, gives a qualitative indication of the extent of the energy transfer from AG97 to FITC. Indeed, the intensity of this band in the gated spectra, reflects the emission of the fluorophore occurring on the long time-scale (between 128 nm and 8 μs). It can be immediately appreciated that when the FITC is attached to the protein, i.e. for BSAFITC, the intensities of its emission band in the gated spectra are considerably higher than in the case of the free FITC diffusing in PBS. This observation is consistent with the idea of a resonance energy transfer favored by the protein structure, which is possibly able to keep donor and acceptor spatially close. However, a clear quantitative discrimination of resonance energy transfer, trivial radiative energy transfer or other non-radiative quenching processes induced to AG97 by the presence of the fluorophore is extremely difficult for this system.

4.4.8 Chapter bibliography

1. Mauro, M., Aliprandi, A., Septiadi, D., Kehr, N. S. & De Cola, L. When self-assembly meets biology: luminescent platinum complexes for imaging applications. *Chem. Soc. Rev.* **43,** 4144–4166 (2014).
2. Jacobson, O., Kiesewetter, D. O. & Chen, X. Albumin-Binding Evans Blue Derivatives for Diagnostic Imaging and Production of Long-Acting Therapeutics. *Bioconjug. Chem.* (2016). doi:10.1021/acs.bioconjchem.6b00487
3. Galstyan, A. *et al.* Correlating the Structural and Photo-physical Features of Pincer Luminophores and Monodentate Ancillary Ligands in PtII Phosphors. *Eur. J. Inorg. Chem.* **2015,** 5822–5831 (2015).
4. Strassert, C. A. *et al.* Switching on luminescence by the self-assembly of a platinum(II) complex into gelating nanofibers and electroluminescent films. *Angew. Chemie - Int. Ed.* **50,** 946–950 (2011).
5. Delcanale, P. *et al.* Zinc-Substituted Myoglobin Is a Naturally Occurring Photo-antimicrobial Agent with Potential Applications in Food Decontamination. *J. Agric. Food Chem.* **64,** 8633–8639 (2016).
6. Schneckenburger, H., Wagner, M., Weber, P., Strauss, W. S. L. & Sailer, R. Autofluorescence Lifetime Imaging of Cultivated Cells Using a UV Picosecond Laser Diode. *J. Fluoresc.* **14,** 649–654 (2004).
7. Aubin, J. E. Autofluorescence of viable cultured mammalian cells. *J. Histochem. Cytochem.* **27,** 36–43 (1979).
8. Waters, J. C. Accuracy and precision in quantitative fluorescence microscopy. *J. Cell Biol.* **185,** 1135 LP-1148 (2009).
9. Bouccara, S. *et al.* Time-gated cell imaging using long lifetime near-infrared-emitting quantum dots for autofluorescence rejection. *J. Biomed. Opt.* **19,** 51208 (2014).
10. Kodama, Y. Time Gating of Chloroplast Autofluorescence Allows Clearer Fluorescence Imaging In Planta. *PLoS One* **11,** e0152484 (2016).
11. Hungerford, G., Benesch, J., Mano, J. F. & Reis, R. L. Effect of the labelling ratio on the photophysics of fluorescein isothiocyanate (FITC) conjugated to bovine serum albumin. *Photochem. Photobiol. Sci.* **6,** 152–158 (2007).
12. Viappiani, C. Use of nonradiative decays of extrinsic fluorophores as structural and dynamical probes in protein environments: Fluorescence quenching. *Biophys. Chem.* **50,** 293–304 (1994).

4.5 Conclusions

4.5.1 Nanostructures based on globins

Two nanostructures based on globins have been investigated, both exploiting apoMb as protein structure for the delivery of two different PSs, Hyp and Zn-PP IX. Despite the structural similarities, the two systems are remarkably different for the type of interaction occurring between the protein portion and the photo-active molecule. While the nanostructure apoMb-Hyp self-assembles in aqueous solutions to form a non-covalent adduct, taking advantage of the hydrophobic effect, the ZnMb reconstituted from apoMb and Zn-PP IX should be considered as a single molecular entity, since the interaction between the protein portion and the PS is stabilized by a coordinative bond. The efficacy of the photosensitization-based inactivation of cells (bacteria or tumor cells) induced by the PSs delivered with the protein-based carrier was evaluated in relation with the photo-physical parameters and correlated to the images collected with fluorescence microscopy techniques.

4.5.1.1 ApoMb-Hyp

While hydrophobic aggregates of Hyp are photo-physically inactive, the PS recovers its photo-activity upon the binding to the hydrophobic cavity of apoMb, that limits the aggregation in aqueous media. It was demonstrated that a stable, water soluble and likely bio-compatible nanostructure forms between apoMb and the monomer of Hyp, with a 1:1 stoichiometry. We determined that the nanostructure is an actual photosensitizing agent, since Hyp retains the ability to generate $^1O_2$ with a quantum yield of 0.14 and it is efficient in the photo-inactivation of tumor cells in vitro and Gram-positive bacteria in suspension. Additionally, the fluorescence emission occurring from the protein-bound Hyp was exploited for the localization of the PS in the presence of cells. By means of femtosecond transient absorption spectroscopy we discovered that protein-bound Hyp has photo-physical properties suitable for being exploited as fluorescent probe for STED nanoscopy, since stimulated emission can be induced without significant excited state absorption. This peculiar photo-physics of Hyp allowed us to image the distribution of the PS on cells with a subdiffraction resolution, that is a particularly important property enabling investigation of the effect of the photosensitization at the subcellular level. Since $^1O_2$ intra-cellular diffusion is limited (~100 nm), a subdiffraction localization of the PS is needed to precisely understand where the photo-damage will be inflicted. Despite STED images revealed a similar distribution of the Hyp delivered with apoMb on bacterial cell wall for both Gram-negative and Gram-positive bacteria, only the latter were effectively inactivated in the photo-treatment. Promising results were obtained for tumor cells of the lines HeLa and PC3 treated with apoMb-Hyp. When delivered with apoMb, Hyp was more efficient in the photo-induced killing of the cells, and resulted photo-toxic at nM concentrations. Images collected with both STED nanoscopy and spinning disk microscopy showed that when Hyp is delivered with apoMb it is more rapidly up-taken by the cells than unbound Hyp, and preferentially accumulates on the plasma membrane of these cells, inducing necrotic death. Conversely, unbound Hyp tends to penetrate the membrane and locates in the cytoplasm where it marks internal components.

4.5.1.2 ZnMb

We assembled ZnMb with the aim of exploiting its remarkable photosensitizing properties (Φ_Δ = 0.9) in biosystems. We demonstrated the possibility of imaging the distribution of ZnMb on cells with confocal fluorescence microscopy, even though the photo-physics of the compound did not allow to reach subdiffraction resolution with STED nanoscopy. The behavior of the photosensitizing agent in the presence of bacterial cells was carefully studied spectroscopically and by means of fluorescence microscopy, which allowed to demonstrate a weak interaction between ZnMb and the cell wall of both Gram-positive *S. aureus* and Gram-negative *E. coli* bacteria. This weak interaction is enough for an efficient photosensitization-based inactivation of the Gram-positive *S. aureus* which are characterized by a more permeable cell wall, whose number of CFUs reduced by ~6 orders of magnitude after the photo-treatment. This is a particularly interesting finding since ZnMb is an endogenous PS, spontaneously forming during maturation of additive free not-cooked cured hams and thus constitutes a potential agent for sanitizer free microbial decontamination of these products.

4.5.2 Nanostructures based on lipocalins

The structure of the lipocalin protein βLG was investigated as carrier for the PS Hyp. βLG constitutes a good model for proteins characterized by a β-barrel structural core, completely different from the folding of globins. The applicative interest of βLG relies on the observation that this protein is the most abundant protein of cow milk whey, and thus can potentially be employed as bio-compatible carrier for PSs in processes related to dairy industry.

4.5.2.1 2βLG-Hyp

With a combination of molecular modeling and spectroscopic techniques we demonstrated that only the dimeric form of βLG, namely 2βLG, can significantly bind the Hyp molecule. The binding is mainly due to hydrophobic effect and occurred at two different binding sites characterized by different affinities for Hyp and located at the interface between the monomers. The small hydrophobic cavity of the protein monomer, wrapped in the β-barrel structure and capable of binding compounds like retinol, is not suitable for accommodating Hyp. The self-aggregation of the nanostructure involved more species than the previously considered nanostructures based on globins. The 2βLG-Hyp is a photo-functional nanostructure since the protein-bound Hyp recovers its ability to photo-generate $^1O_2$ and to emit a detectable fluorescence. The photosensitization-based antimicrobial action of the nanostructure was tested against the Gram-positive *S. aureus* in suspension, whose number of CFUs reduced by 6 logarithmic units in consequence of the photo-treatment. We thus demonstrated the possibility to obtain the self-assembled stable nanostructure 2βLG-Hyp, that is a water soluble and bio-compatible system suitable for photosensitization-based applications, particularly in the context of dairy industry.

A careful inspection of the 2βLG-Hyp nanostructure revealed that one of the protein-bound Hyp molecules, located in a wider binding site, has one face exposed to the solvent. This has a detrimental effect on the photo-physical properties of the PS, due to the partial exposure to an aqueous environment, and possibly to a residual aggregation of the PS on this site. The peculiar solvation properties of βLG allowed to introduce 20% DMSO as co-solvent without affect the integrity of the protein structure. We demonstrated that DMSO coats the protein, providing a better environment for the protein-bound Hyp molecules, which substantially improved their photo-activity, increasing the fluorescence, triplet and $^1O_2$ quantum yields. Unexpectedly, the presence of the DMSO was detrimental to the antibacterial treatment of *S. aureus*, despite the higher amount of $^1O_2$ generated with respect to the pure buffer solution. The surprising behavior most likely arises from the altered interactions of the photosensitizing agent with the DMSO coating, that prevent reaching sensitive regions of the bacterial wall. This result demonstrate that the improved photo-physical properties of the delivery system are not necessarily translated into more effective antimicrobial activity, since this is a result of both photosensitization ability and interaction of the drug with the target cell.

4.5.3 Nanostructures based on albumins

BSA was investigated as delivery system for metal-organic triplet emitter molecules with a tetra-coordinated Pt atom forming a quasi-square planar structure. The peculiar nature of the excited state of this molecules gives rise to luminescence decay with long lifetime, on the time scale of μs, but with quantum yields comparable to those of usual fluorophores. These features make them attractive as luminescent reporters for bio-imaging.

4.5.3.1 BSA-AG97

The major problem concerning the use of the tested triplet emitter compounds is aggregation. Unlike Hyp, the hydrophobic aggregates of these compounds resulted more luminescent than monomers, whose emission is almost completely quenched. However the slow equilibration of the aggregates resulted in unstable and poorly reproducible spectroscopic properties of the compound placed in aqueous buffers, which are inadequate for imaging applications. We demonstrated that the triplet emitted molecule AG97 interacts with BSA in aqueous solution forming a self-assembled nanostructure where the protein appears to stabilize small homogenous clusters of the active molecule, which retains its characteristic luminescence on the µs scale. It was thus possible to obtain a stable, self-assembled and water soluble nanostructure with reproducible properties. Unlike other structures, BSA-AG97 is not sensitive to O_2 and thus is not exploitable as photosensitizing system. But this makes it even more attractive as luminescent reporter since it is not producing reactive oxygen species. The same nanostructure was reproduced using a BSA labelled with the fluorophore FITC (BSAFITC), and we demonstrated that a simple operation of time-gating of the time-resolved emission signal collected from BSAFITC-AG97 allows to separate the emission of the triplet emitter from the intense but fast fluorescence of the BSAFITC. This gated detection method is particularly interesting since it allows to isolate the emission of the triplet emitter reporter delivered with the protein-based carrier from the unwanted scattering, fluorescence and autofluorescence contribution occurring on real bio-samples. Incidentally, we noticed the occurring of an energy transfer process between the AG97 and the FITC, favored by the presence of the protein-based structure. This opens the way to further studies since the overall effect of this process is to obtain a delayed fluorescence emission of the FITC on the µs time scale.

5 Acknowledgements

This work would not have been possible without the close collaboration and friendship between different research groups spread around Europe. I would like to thank all the enthusiastic scientists that I have had the pleasure to meet during my PhD, from group leaders to students.

Special thanks to prof. Santi Nonell and his fantastic group, together with prof. Montserrat Agut, at Institut Químic de Sarrià in Barcelona (Spain). During the long period that I spent in their labs, they always treated me like a member of the team and like a friend. $^1O_2$ measurements, microbiological essays and many other results exposed in this work would not have been possible without their support, help and guide. I want particularly to thank my PhD colleagues in Barcelona: Beatriz, Ester, Joaquim, Oriol, Roger and Rubén.

Special thanks also to Dr. Cristian A. Strassert and his group, together with prof. Andreas Faust, at the University of Münster (Germany). I spent an amazing and fruitful, even though short, period in their lab investigating the challenging triplet emitters molecules. I want particularly to thank Anzhela, who synthesized the molecules and helped me in the lab, Linda, Dario, Jan, Marvin and Sebastian.

The microscopy experiments (STED, confocal and spinning disk) were performed at the Italian Institute of Technology of Genoa (Italy) in close collaboration with the group of prof. Alberto Diaspro, who hosted us several times in his lab. Particular thanks to Dr. Paolo Bianchini, Francesca Pennacchietti and Michele Oneto.

The femtosecond transient absorption spectroscopy measurements were performed at LENS (European Laboratory for Non-linear Spectroscopy) in Florence (Italy) by the group of prof. Paolo Foggi.

The molecular modeling simulations were performed by the group of prof. F. Javier Luque at the University of Barcelona (Spain).

Within the University of Parma, we collaborated with the group of Dr. Massimiliano Tognolini for the experiments involving eukaryotic cells; and with Dr. Stefano Bruno, who always helped me with protein preparations and with bacteria growth.

I want to thank all the people of the bio-physics group at the University of Parma for the support, particularly my lab colleague Chiara Montali who is always willing to help me.

If I have put enthusiasm and passion in this work, it is because I had the privilege to meet good people and good teachers on my way: Dr. Stefania Abbruzzetti, and my tutor prof. Cristiano Viappiani.

Infine, vorrei ringraziare coloro che mi sono sempre stati vicino, in questi tre anni come nel resto della vita, con la loro amicizia, il loro sostegno ed il loro amore. I miei amici, la mia famiglia, Giulia ed i miei genitori.

Pietro
Dicembre 2016